From structural fluctuations to vibrational spectroscopy of adsorbates on surfaces: A theoretical study of H_2O on α-Al_2O_3(0001)

Dissertation zur Erlangung des akademischen Grades
>doctor rerum naturalium< (Dr. rer. nat.)
in der Wissenschaftsdisziplin Theoretische Chemie

vorgelegt von

Giacomo Melani

an der
Mathematisch-Naturwissenschaftlichen Fakultät
der Universität Potsdam

Potsdam, September 2019

Diese Arbeit ist zwischen Oktober 2015 und September 2019 in der Arbeitsgruppe von Prof. Dr. Peter Saalfrank am Institut für Chemie der Universität Potsdam entstanden.

Potsdam, September 2019

Erstgutachter: Prof. Dr. Peter Saalfrank
Zweitgutachterin: Prof. Dr. Beate Paulus
Drittgutachter: Prof. Dr. Marialore Sulpizi

A Nonna Ghighi.

Contents

Preamble

It is surely a pure delight to know, how and by what processes this earth is clothed with verdure and life, how the clouds, mists and rain are formed, what causes all the changes of this terrestrial system of things, and by what divine laws order is preserved amidst apparent confusion.

Humphry Davy

Metal oxides are geologically abundant materials which constitute a large portion of Earth's crust minerals. Conversely, water is the most common solvent on this planet, covering more than 70% of its surface. Therefore, already from the geochemical perspective, it is easily intuitive how important is to understand the chemistry of water on metal oxide surfaces. Among other metal oxide-based geomaterials, *corundum* is an Al-rich mineral, more precisely the crystalline form of α-Al_2O_3, also known as α-alumina, which is the most common and stable polymorph of aluminum oxide.
Two well-known gem varieties are composed mainly of corundum: *ruby* and *sapphire*. The first is a red-coloured gemstone, whose color is due to the presence of chromium impurities. It is curiously from the Sanskrit word for ruby, *kuruvinda*, that comes the term "corundum". The other gem, sapphire, is typically blue but it can be found in other pigmentations from yellow to purple, green to orange, due to trace amounts of other elements within the aluminum oxide structure, such as iron, titanium, copper, and more. From the geochemical point of view, α-alumina particles can act as ice-nucleating agents in the Earth's atmosphere as they can be found in mineral dust aerosols, suspended nanostructures which are emitted from wind-blown soils [3]. In the troposphere, water can adsorb on these aluminum oxide particles to form ice, under certain conditions of temperature and pressure, but can also influence the adsorption of trace gases such as nitric acid, HNO_3 [4–7]. Also the heterogeneous ice nucleation on α-alumina is still under investigation, particularly with respect to the role played by co-adsorbed ions, which seem to suppress this processes due to induced surface charges [8].
On the technological side, aluminum oxide has renowed applications as abrasive, thanks to its hardness and strength, and as pigment. It is also used in ceramics and materials science as well as in more chemically-related contexts where it is one of the most adaptable sorbents for preparative, flash and column chromatography. Aluminum oxide also finds applications in heterogeneous catalysis (more the γ-alumina form), while its hydroxide derivatives can be employed in the manufacture of microporous aluminosilicate materials, namely zeolites.

For the above reasons, water / aluminum oxide interfaces have fundamental importance in surface chemistry and physics. It is therefore crucial to address the adsorption mechanisms, as well as the structural properties of water-covered, or hydrated alumina surfaces. In this work, the α-$Al_2O_3(0001)$ surface termination is taken as representative model system to investigate water interactions towards it. Particular focus in given on the characterization of adsorbed species from their vibrational frequencies. To this respect, inspirational, challenging and eventually fruitful has been the ongoing collaboration of our group with the "Interfacial Molecular Spectroscopy" group lead by Dr. R. Kramer Campen at the Department of Physical Chemistry,

Fritz-Haber Institute of Max Planck Society in Berlin. The expertise of our experimental collaborators in surface-sensitive vibrational spectroscopy has played a key role in providing the cues for this theoretical work and in representing the main source of comparison for the results of our simulations.
Methodologically, the work presented here is firmly based on periodic Density Functional Theory (DFT) and on Ab Initio Molecular Dynamics (AIMD). After almost twenty years from the seminal paper of Hass and coworkers [9, 10], the computational techniques used to describe the H_2O / α-Al_2O_3 interface have evolved, albeit remaining anchored to the same theoretical principles. Interestingly, even in his Nobel Prize for Chemistry lecture of January 1999, Prof. Walter Kohn mentioned the work of Hass *et al.* as instructive example of the potential applications of DFT to describe complex systems as aqueous interfaces.

In this work, the main focus is on the (0001) termination of α-Al_2O_3 surface. This metal oxide crystallizes starting from a hexagonal unit cell defined by primitive lattice vectors $\underline{a}$, $\underline{b}$ and $\underline{c}$, and angles α, β and γ, such as: $|\underline{a}| = |\underline{b}| \neq |\underline{c}|$, $\alpha = \beta = 90°$ and $\gamma = 60°$. Although this metal oxide has been the subject of various studies, both theoretical and experimental, here we refer to the systematic characterization operated by Kurita *et al.* [11], who recently established the respective energetics of the three thermodynamically most stable α-alumina surface terminations: (0001), $(1\bar{1}02)$ and $(11\bar{2}0)$. According to Kurita's analysis as well as other works, the (0001) is globally the most stable termination for α-alumina surface in oxygen-free, or Ultra High Vacuum (UHV) conditions. Following the (0001) basal plane, we find that oxygen ions form a hexagonal closely packed structure, while Al^{3+} ions are located at two thirds of octahedral sites of the oxygen sublattice. Consequently, the coordination number of oxygen is 4, whereas it is 6 for aluminum. As also described in Ref. [11], further stability is associated with (0001) termination at single Al layer (Al-I surface model). The latter, which will be simply referred to as "Al-terminated surface" in what follows, is employed here to describe α-Al_2O_3 interacting with few water molecules.

The research work presented in this thesis is divided into three main parts: the first concerning the description of the water (D_2O) dissociative adsorption on the Al-terminated (0001) surface. Here the aforementioned computational techniques are used to characterize the vibrational frequencies of the adsorbed OD species, up to the direct calculation of vibrational spectra from molecular dynamics simulations at finite temperature. More specifically, the main focus of this part of the work has been directed towards extending previously reported analysis [12] of adsorbed OD species on the Al-terminated α-Al_2O_3. Indeed, Kirsch and coauthors [12] reported a combined theoretical and experimental study, where D_2O dosing was realized with a Molecular Beam Source (MBS), while spectroscopic characterization was done by means of Vibrational Sum Frequency (VSF) generation. Theory was based on DFT calculations at the Generalized Gradiend Approximation (GGA) level of theory, yielding vibrational frequencies corresponding to singly dissociated water molecules on three different adsorption sites: 1-2, 1-4 and 1-4′ (the corresponding nomenclature will be properly explained later). Calculated OD stretching frequencies from Normal Mode Analysis were in relatively good agreement with experimental VSF resonances, although absolute frequencies had an almost constant 100 cm^{-1} redshift compared to experiment. In order to go beyond this static description, the main purpose of this part of the work has been to employ AIMD simulations at 300 K to include characteristic finite-temperature effects which are known to affect vibrational spectra. Moreover, the employment of time-correlation functions methods allows us to calculate vibrational responses, from the Vibrational Densities of States (VDOS), to InfraRed (IR) and VSF spectra, which will be

described and reported below.

In the second part of this work, unlike the previous case, which refers to a low coverage situation congruent to UHV conditions, the focus is shifted towards the study of the water / aluminum oxide interface in environmental, moist conditions. Indeed, several experimental and computational studies highlighted how the α-Al_2O_3(0001) surface may get restructured under greater water contents or relative high humidity to form an OH-terminated, or hydroxylated surface (HS) where the topmost single Al layer is removed and the oxygen layer beneath forms O-H bonds resulting from water dissociation. In such process, each terminating Al atom is thought to be replaced by three H atoms. Again, the interplay between theory and VSF experiments play a major role to properly address the surface structure by its adsorbates vibrations. As for the Al-terminated surface, the combination of periodic DFT with AIMD trajectories at 300 K yields vibrational spectra (VDOS, IR and VSF) in very good agreement with experimental ones, underlying high-frequency OH stretching vibrations associated with terminating Al-OH bonds, called "aluminols" in what follows. Besides, in order to provide potential insights towards higher coverage situations, a further water-covered hydroxylated surface model (HS+2ML) is considered, where an additional water layer is adsorbed on the HS surface. Here, the role of interfacial hydrogen bonding determines the different vibrational response of this system. For both HS and HS+2ML, vibrational spectra obtained from velocity-velocity autocorrelation functions (as for the Al-terminated surface models) are fully described below.

Eventually, a third part of the thesis collects the work done to address the behaviour of interfacial OH species upon IR excitation. Also for this case, the motivation arises from collaboration with experimental partners, who performed time-resolved pump-probe VSF spectroscopy at the air / solid and liquid / solid interfaces of α-alumina. In these experiments, where infrared light is shined onto a water-covered α-Al_2O_3(0001) surface, surface-bound OH (*i.e.* aluminols) are presumably excited, leading to vibrational lifetimes for OH stretch transitions in the order of few picoseconds. These lifetimes are either quite short when compared to other adsorbates on insulating surfaces (for instance CO on NaCl), or quite long if related to typical OH vibrational decays in bulk water or aqueous environments. It is therefore through *ab initio* molecular dynamics that we decide to tackle this problem, particularly using a recently-developed non-equilibrium MD scheme, which has been properly adapted for the purposes of this work. In non-equilibrium AIMD trajectories, the IR excitation is "mimed" by adding kinetic energy into selected modes of interfacial aluminols of the HS+2ML model, whose behaviour is tracked in time. The analysis of both time-dependend OH kinetic energy and of time-resolved spectral responses indicates a timescale for vibrational energy relaxation within 2-4 ps. While non-hydrogen-bonded aluminols are selectively excited, the main acceptor modes for the excessive kinetic energy can be retrieved within OH bonds from two structural domains, the hydrogen-bonded aluminols and the additional water layer. This observation can provide insights into the mechanism of energy dissipation at the water / α-alumina interface.

1 Electronic Structure Theory and Molecular Simulations

We are perhaps not far removed from the time when we shall be able to submit the bulk of chemical phenomena to calculation.

Joseph Louie Gay-Lussac

1.1 Fundamentals of molecular quantum mechanics: The Born-Oppenheimer approximation

The quantum-mechanical description of any chemical system is dictated by the solution of the time-dependent Schrödinger equation (TDSE) [13]:

$$i\hbar\frac{\partial\Psi(\underline{\eta},t)}{\partial t} = \hat{H}(\underline{\eta};t)\Psi(\underline{\eta};t) = \left[-\frac{\hbar^2}{2m}\nabla^2 + V(\underline{\eta};t)\right]\Psi(\underline{\eta};t) \quad . \tag{1.1}$$

Here, $\hat{H}(\underline{\eta};t)$ represents the Hamiltonian operator with its kinetic energy and potential energy terms. The solution of TDSE is a wavefunction $\Psi(\underline{\eta};t)$, which depends on both system's spatial coordinates, $\underline{\eta}$, and, parametrically, on time. By knowing Ψ, all physical properties and behaviour of the system can be extracted. If the latter is not explicitly dependent on time, for instance if the system doesn't interact with electromagnetic fields, the TDSE can be simplified and the corresponding time-independent Schrödinger equation (TISE) arises: $\hat{H}(\underline{\eta})\Psi_k(\underline{R}) = E_k(\underline{\eta})\Psi_k(\underline{\eta})$. The TISE is an eigenvalue problem, whose eigenvalues E_k are energy levels for the considered system and whose eigenstates Ψ_k are called "stationary states" (because their eigenvalues are constant in time).

Unfortunately, no analytical solution of the Schrödinger equation exists for many-particles systems of interest in chemistry, and physics, especially in the condensed phase. Over the years methods to obtain approximate solutions have been provided, among which the most successful in quantum chemistry is the so-called "Born-Oppenheimer Approximation" (BOA) [13]. Proposed by Max Born and J. Robert Oppenheimer in 1927, the BOA invokes a fundamental assumption: due to the great difference in masses between electrons and nuclei, their motion may be separated and the total wavefunction may be written as a product of the two independent parts. Here, we shall focus on the BOA formalism starting from the time-independent Schrödinger equation, although the theory is general.

For a system with N_e electrons and N_α atomic nuclei, the total wavefunction $\Psi(\underline{r},\underline{R})$ can be factorized in an electronic and a nuclear part, as: $\Psi(\underline{r},\underline{R}) = \psi_e(\underline{r};\underline{R})\chi_n(\underline{R})$. Here $\underline{r} = \{\underline{r}_i\}$ and $\underline{R} = \{\underline{R}_\alpha\}$ correspond to the collective coordinate vectors in Cartesian space of electrons and nuclei, respectively (neglecting the spin).

The electronic wavefunction ψ_e, which shall depend explicitly on electronic positions and only parametrically on the nuclear coordinates, it is then the eigenstate of an electronic Hamiltonian, $\hat{H}_e(\underline{r})\psi_{e,k}(\underline{r};\underline{R}) = U_k(\underline{R})\psi_{e,k}(\underline{r};\underline{R})$, where $\hat{H}_e$ is (in atomic units, $\hbar = 1$, $e = 1$, $m_e = 1$):

$$\hat{H}_e = -\frac{1}{2}\sum_i^{N_e}\nabla_i^2 - \sum_i^{N_e}\sum_\alpha^{N_\alpha}\frac{Z_\alpha}{|\underline{r}_i - \underline{R}_\alpha|} + \frac{1}{2}\sum_i^{N_e}\sum_{j\neq i}^{N_e}\frac{1}{|\underline{r}_i - \underline{r}_j|} + \frac{1}{2}\sum_\alpha^{N_\alpha}\sum_{\beta\neq\alpha}^{N_\alpha}\frac{Z_\alpha Z_\beta}{|\underline{R}_\alpha - \underline{R}_\beta|} \tag{1.2}$$

where Z_α is the charge of a given nucleus. $U_k(\underline{R})$ corresponds to the "potential energy surface" (PES), a multidimensional function associated with the electrostatic field felt by the nuclei and originated by the electrons at a given atomic configuration.

Parallely, the nuclear wavefunction χ solves the corresponding nuclear TISE: $\hat{H}_{n,k}(\underline{R})\chi_{n,kv}(\underline{R}) = E_{kv}(\underline{R})\chi_{n,kv}(\underline{R})$, where:

$$\hat{H}_{n,k}(\underline{R}) = -\frac{1}{2}\sum_\alpha^{N_\alpha}\frac{1}{M_\alpha}\nabla_\alpha^2 + U_k(\underline{R}) \quad . \tag{1.3}$$

The indices k and v mean that while the resolution of the electronic TISE provide a kth-electronic eigenstate, the nuclear one gives rize to a so-called "vibronic" wavefunction, where a given χ shall be pigeonhold to a certan electronic state but also to a manifold of inner translational and rovibrational sub-levels, here indicated by the single index v.

The resulting picture from the BOA assumes therefore an electronic wavefunction that depends on electron positions but for a fixed set of nuclear coordinates $\underline{R}$. At the same time, nuclei can move on a potential energy surface generated by specific electronic densities. However, it should be noted that the total wavefunction as a product of $\psi_{e,k}$ and $\chi_{n,kv}$ only fulfills the total Schrödinger equation if additional terms involving derivatives of the electronic wavefunction with respect to nuclear coordinates are considered. These terms are known as "non-adiabatic couplings" (NAC) and "diagonal Born-Oppenheimer corrections" (DBOC). They are usually thought to be very small (because they inversely depend on nuclear masses), so that they are neglected in the BOA picture. Nonetheless, when light-induced processes like in photochemistry are considered or when strong interactions between nuclear motion and electronic states are involved, for instance in the scattering of a molecule on a metal surface, the BOA breaks down.
In what follows, we will always refer to processes associated with the fundamental or "ground" electronic state, $\psi_{e,0}$ and the Born-Oppenheimer scheme will be fully adopted.

1.2 From electronic states to band structure of solids

1.2.1 Wavefunction representation based on Slater determinants

Let us now focus on the solution of the electronic Schrödinger equation. Since electrons are fermionic particles, the corresponding total wavefunction must be antisymmetrical under the interchange of two identical particles: $\psi(1,2) = -\psi(2,1)$, for a two- electron system (to simplify the notation, from now on, the index "e" will be left away). Conversely, electrons must also obey Pauli's "exclusion principle", according to which two electrons cannot occupy the same "spinorbital". A spinorbital, φ, is the product of an electronic spatial orbital ϕ and electronic

spin function γ , the latter related to the spin quantum number, $m_s = +/-1/2$. Mathematically, an electronic wavefunction which satisfies both fermionic antisymmetry and Pauli's principle can be expressed by a Slater determinant:

$$\psi(1,2,...,N_e) = \left(\frac{1}{N_e!}\right)^{1/2} \begin{vmatrix} \varphi_1(1) & ... & \varphi_{N_e}(1) \\ \vdots & & \vdots \\ \varphi_1(N_e) & ... & \varphi_{N_e}(N_e) \end{vmatrix} \quad . \tag{1.4}$$

Here $\varphi_i(p) = \varphi_i(\underline{p})$ indicates the ith-spinorbital for each pth-electron: $\varphi_i(\underline{p}) = \phi_i(\underline{r}_p)\gamma(\omega_p)$, where $\underline{p}$ is a collective eletronic coordinate and $\underline{r}_p$ is its spatial component. The spin variable $w_p = m_s$ determines the value of the spin function $\gamma(\omega_p) = \alpha(\omega_p)$ or $\beta(\omega_p)$, where $\alpha(+1/2) = \beta(-1/2) = 1$ and $\alpha(-1/2) = \beta(+1/2) = 0$.

Most quantum-chemical approaches to solve the electronic TISE by expressing the wavefunction with a Slater determinant, which have been proposed over the years, start from the "Hartree-Fock" (HF) method, or "Self-Consistent Field" (SCF). In this approach, a single Slater determinant is adopted to best describe the electronic wavefunction by employing a minimization procedure. The solution of this SCF-iteration is then associated with the electronic ground state ψ_0. Before going into details of other strategies to solve the TISE for electrons, we should remark that spatial orbital wavefunctions are often represented by means of a basis: $\phi_i = \sum_s c_{si}\xi_s$. The choice of the basis functions ξ_s can be quite various and many basis sets have been developed. Among these, quantum-chemical methods often rely on linear combination of atomic orbitals (LCAOs), where the latter are constructed by using Slater-type orbitals (STOs) or by Gaussian-type orbitals (GTOs) [13, 14]. Such methods have shown to be very useful to describe both molecular and extended systems.
However, in the context of condensed-phase simulations, other expansions can be employed, for instance when we are dealing with a solid or a surface. Since the aim of this work has been to study the spectroscopic and dynamical properties of a metal-oxide surface, the computational methods adopted here rely on a "plane-wave" (ξ^{PW}) basis. Let us therefore start with the quantum-mechanical treatment of a periodic system.

1.2.2 Quantum theory of solids and surfaces

In a solid or a surface, each atom can be associated with a point in the crystal lattice [15]. The arrangement of atoms in a regular lattice must follow translational symmetry conditions, namely that from an elementary structure, known as "unit cell", its repetitions along the x, or y, or z (or all) axes generate the periodic crystal. A category of lattice units well-known in crystallography and solid state physics comprises the 14 "Bravais Lattices", each of them representing a fundamental arrangement of points in space with corresponding symmetry, including unit-cell structures such as the "cubic" or the "hexagonal" ones, the latter being employed in this work.

The periodicity of a lattice in three dimensional space is mathematically associated to a lattice vector $\underline{B}$, given by: $\underline{B} = n_1\underline{a}_1 + n_2\underline{a}_2 + n_3\underline{a}_3$, where n_1, n_2 and n_3 are integers and $\underline{a}_1$, $\underline{a}_2$ and $\underline{a}_3$ are three linearly independent vectors, also called "primitive vectors". The lattice vector $\underline{B}$ is usually referred to as the "direct vector" or "vector in the direct space".
Without loss of generality, another vector representation can be defined, where each point associated with a vector $\underline{G}$ shall obey the condition: $\underline{G} \cdot \underline{B} = 2\pi m$, with m being an integer, or

$e^{i\underline{G}\cdot\underline{B}} = 1$, analogously. The new lattice vector defines the so-called "reciprocal space", hence is called "reciprocal vector" $\underline{G}$: $\underline{G} = h\underline{b}_1 + k\underline{b}_2 + l\underline{b}_3$. Here, h, k and l are also integers, while $\underline{b}_1$, $\underline{b}_2$ and $\underline{b}_3$ are the primitive vectors (in reciprocal space). Between primitive vectors in direct space and in reciprocal space, fixed relations are present. Indeed, the vectors $\underline{b}_j$ can be derived from $\underline{a}_i$ vectors as follows:

$$\underline{b}_1 = 2\pi \frac{\underline{a}_2 \times \underline{a}_3}{\underline{a}_1 \cdot (\underline{a}_2 \times \underline{a}_3)} \tag{1.5}$$

$$\underline{b}_2 = 2\pi \frac{\underline{a}_3 \times \underline{a}_1}{\underline{a}_2 \cdot (\underline{a}_3 \times \underline{a}_1)} \tag{1.6}$$

$$\underline{b}_3 = 2\pi \frac{\underline{a}_1 \times \underline{a}_2}{\underline{a}_3 \cdot (\underline{a}_1 \times \underline{a}_2)} \tag{1.7}$$

The $\underline{a}_i$ and $\underline{b}_j$ obey: $\underline{a}_i \cdot \underline{b}_j = 2\pi\delta_{ij}$.
Integers h, k and l are also named "Miller indices" and they can be used to characterize a particular crystallographic plane, indicated by $[hkl]$. For hexagonal (and rhombohedral) lattices, a slightly different notation known as "Miller-Bravais" indices $(hkil)$ may also be employed (as in this work). Index i can be further defined by h and k with the relation $i = -(h + k)$, hence its redundancy. For instance, the hexagonal surface plane (0001) would then correspond to the original notation [001].

In direct, or real space the primitive vectors describe a "primitive cell", namely the minimum-volume unit cell corresponding to a single lattice point of a structure with discrete translational symmetry. When such a primitive cell is centered around a lattice point (mathematically defined by the Voronoy decomposition), it is called a "Wigner-Seitz cell". This region of space in a periodic lattice is analogously defined by reciprocal vectors and is named "First Brillouin Zone" (FBZ). The centre of the FBZ is called Γ-point.

Electrons in a periodic crystal as in a solid or a surface are subject of an effective potential $U(\underline{r})$, which has the same translational symmetry of the lattice itself, as mentioned above, so that: $U(\underline{r}) = U(\underline{r} + \underline{B})$. It is therefore crucial that the electronic wavefunction obeys this condition. Bloch's theorem [15] states that the eigenfunctions of a potential with such translational symmetry must be of the form: $\phi_{n\underline{k}}(\underline{r}) = e^{i\underline{k}\underline{r}} u_{n\underline{k}}(\underline{r})$, where both the wave vector $\underline{k} = m_1\underline{b}_1 + m_2\underline{b}_2 + m_3\underline{b}_3$ (m_1, m_2 and m_3 are fractional numbers, so that $\underline{k} \in$ FBZ) and n are quantum numbers, the latter being the "band" . The basis wave-like functions $u_{n\underline{k}}(\underline{r})$ must also obey translational symmetry: $u_{n\underline{k}}(\underline{r}) = u_{n\underline{k}}(\underline{r} + \underline{B})$. A corollary of Bloch's theorem for eigenfunctions $\phi_{n\underline{k}}(\underline{r})$ is: $\phi_{n\underline{k}}(\underline{r})e^{i\underline{k}\underline{B}} = \phi_{n\underline{k}}(\underline{r} + \underline{B})$. Bloch's functions, $u_{n\underline{k}}(\underline{r})$, can be further expanded as a set of plane waves (χ^{PW}), which satisfy all prementioned symmetry relations.
The solution of the Schrödinger equation employing Bloch's wavefunctions are band energies, $\epsilon_{n\underline{k}}$ (or $\epsilon_n(\underline{k})$), which determine the "band structure" of a given crystalline material.

An important remark shall be spent regarding periodic boundary conditions (PBC). In fact, the macroscopic periodicity of the crystal not only restricts the allowed values of quantum number $\underline{k}$, but it becomes central in computational practice when simulating a periodic system. Unless the Bravais lattice is cubic, the most general way to apply PBCs is through the so-called "Born-von Karman" boundary condition, where we consider a translation vector $\underline{B}$ proportional to the primitive vectors $\underline{a}_i$. In this way the relationship derived from Bloch's theorem becomes: $\phi_{n\underline{k}}(\underline{r} + N_i\underline{a}_i) = e^{iN_i\underline{k}\cdot\underline{a}_i}\phi_{n\underline{k}}(\underline{r})$, for $i = 1, 2, 3$. Here, N_i are all integers determining the total

number of primitive cells in the crystal, $N = N_1 N_2 N_3$. From this new condition we can express the allowed Bloch wave-vectors as: $\underline{k} = \sum_i^3 \frac{m_i}{N_i} \underline{b}_i$, where m_i are integers and $\underline{b}_i$ are the primitive vectors in reciprocal space.

1.3 Density Functional Theory

1.3.1 Basics

Among the many quantum chemistry approaches to solve the TISE, several methods starting from Hartree-Fock (HF) theory have been developed, generally referred to as "wave-function theory" (WFT) methods, such as Configuration Interaction (CI), Coupled Cluster (CC) or Multi-Configurational Self-Consistent Field (MCSCF) to name a few. These methods offer great computational accuracy and they are systematically improvable. However, they can be feasibly applied only to systems with few tens of atoms since their computational cost increases rapidly with N, a number related to the system's size [14]. For instance, HF scales with N^4, while CCSD(T), the so-called "gold standard of quantum chemistry", scales with N^7, but even steeper scaling can be reached like in the full CI method (FCI), which depends exponentially on N.
Another computational strategy which has become particularly successful in the quantum chemistry community is Density Functional Theory (DFT) [13, 16]. This approach is radically different from WFT methods since it doesn't actually solve the TISE. Instead of the electronic eigenfunctions, all information about the system is obtained *via* the corresponding electronic density, $\rho(\underline{r})$:

$$\rho(\underline{r}) = N_e \int d\underline{r}_2 ... \int d\underline{r}_{N_e} \psi(\underline{r}, \underline{r}_2, ..., \underline{r}_{N_e}) \psi^*(\underline{r}, \underline{r}_2, ..., \underline{r}_{N_e}) \tag{1.8}$$

where N_e is the normalization constant and $\psi(\underline{r})$ is the electronic wavefunction. Relying on ρ instead of ψ is computationally more efficient, since the latter depends on $3N_e$ coordinates, while the density only on the three Cartesian ones (neglecting the electronic spin).

The modern development of DFT began with the formulation of two theorems by P. Hohenberg and W. Kohn [13]. The first one, known also as "existence theorem", states that the ground-state electronic energy (for which: $\hat{H}_e \psi_0 = E_0 \psi_0$) and all other ground-state electronic properties can be uniquely determined by knowing the corresponding electronic density. In DFT, the total energy is considered as a "functional" of the electronic density. Direct consequence of this theorem is that many quantum-mechanical observables can be directly obtained from the ground-state energy without the necessity to calculate wavefunctions.
The second Hohenberg-Kohn theorem, also named "variational theorem of DFT", introduces an analog for the variational principle of wavefunctions, namely: for a trial density $\rho'(\underline{r})$, the corresponding energy functional $E_0[\rho']$ cannot be less than the exact ground-state energy. We have therefore: $E_0[\rho'] \geqslant E_0^{exact}$. This second theorem allows to employ a minimization procedure as in the SCF-method where an initial guess for the density is then improved to achieve the ground-state energy.

In the framework of DFT, the total electronic energy functional can be expressed as:

$$E[\rho] = T[\rho] + V_{ee}[\rho] + \int d\underline{r} \rho(\underline{r}) v_{ext}(\underline{r}) \tag{1.9}$$

here, $T[\rho]$ is the kinetic-energy functional, $V_{ee}[\rho]$ represents the intelectronic repulsive energy functional, while $v_{ext}(\underline{r})$ is an external potential which includes the electron-nuclear interaction:

$$v_{ext}(\underline{r}) = -\sum_{\alpha}^{N_\alpha} \frac{Z_\alpha}{|\underline{r} - \underline{R_\alpha}|} \quad . \tag{1.10}$$

Historically, one of the main difficulties of DFT, even before the two Hohenberg-Kohn (HK) theorems, has been to find an expression for the kinetic energy term, $T[\rho]$. In fact, one of the early attempts to describe it was the Thomas-Fermi (TF) model, in which the kinetic energy is expressed directly from the electronic density, the latter based on the homogeneous electron gas:

$$T^{TF}[\rho] = C_F \int \rho(\underline{r})^{\frac{5}{3}} d\underline{r} \tag{1.11}$$

where $C_F = \frac{3}{10}(3\pi^2)^{\frac{2}{3}}$. As we will see also for the exchange term from the "Local Density Approximation" below, the assumption of homogeneous electron gas as representative model is valid only for certain (metallic) systems, but completely fails for molecules. However, the TF model still represents a fundamental standpoint in context of density functional theories closer to the original HK theorems.

A major improvement in the formulation of DFT was brought by the "orbital description" introduced by W. Kohn and L. J. Sham [17], who hypothesized a reference system consisting of N_e non-interacting electrons in an external reference potential $v_{ref}(\underline{r})$. The electronic density of the reference system, ρ_{ref}, shall be identical to the real density $\rho(\underline{r})$. The Hamiltonian for such reference system can be then written as a sum of one-electron components:

$$\hat{h}_{ref} = \sum_{i}^{N_e} \hat{h}_i^{KS} = \sum_{i}^{N_e} \left[-\frac{1}{2}\nabla_i^2 + v_{ref}(\underline{r}_i) \right] \quad . \tag{1.12}$$

The solutions of the corresponding eigenvalue equation are called "Kohn-Sham spatial orbitals": $h_i^{KS}\phi_i^{KS} = \epsilon_i^{KS}\phi_i^{KS}$. The reference density can be then obtained as: $\rho_{ref} = \sum_i^{N_e} |\phi_i^{KS}|^2$. Correspondingly, a Slater determinant representing the ground-state wavefunction for the reference system can be written:

$$\psi_{ref}(1, 2, ..., N_e) = \left(\frac{1}{N_e!}\right)^{1/2} \begin{vmatrix} \varphi_a^{KS}(1) & ... & \varphi_z^{KS}(1) \\ \vdots & & \vdots \\ \varphi_a^{KS}(N_e) & ... & \varphi_z^{KS}(N_e) \end{vmatrix} \tag{1.13}$$

where φ^{KS} are the Kohn-Sham spinorbitals. The KS-formulation resembles quite deeply the single-determinant picture of the HF-method, although the physical meaning of KS-orbitals is disputable.

The "new" total energy functional can be written in terms of the reference density:

$$E[\rho] = T_{ref}[\rho_{ref}] + J_{ref}[\rho_{ref}] + \int d\underline{r}\rho(\underline{r})v_{ext}(\underline{r}) + \{T[\rho] + V_{ee}[\rho] - (T_{ref}[\rho_{ref}] + J_{ref}[\rho_{ref}])\} \tag{1.14}$$

here $J[\rho]$ indicates the classical Coulomb term expressed as: $J[\rho] = \frac{1}{2} j_0 \int \frac{\rho(\underline{r}_1)\rho(\underline{r}_2)}{|\underline{r}_1 - \underline{r}_2|} d\underline{r}_1 d\underline{r}_2$.

Since ρ_{ref} and ρ are supposed to be equal, $E[\rho]$ can be further rewritten in simpler terms:

$$E[\rho] = T_{ref}[\rho] + J[\rho] + \int d\underline{r} \rho(\underline{r}) v_{ext}(\underline{r}) + E_{XC}[\rho] \tag{1.15}$$

where $E_{XC}[\rho] = T[\rho] + V_{ee}[\rho] - (T_{ref}[\rho] + J[\rho])$ is known as "exchange-correlation" functional. The reference potential v_{ref} is then written as:

$$v_{ref}(\underline{r}) = v_{ext}(\underline{r}) + \frac{\delta J}{\delta \rho} + \frac{\delta E_{XC}}{\delta \rho} \quad . \tag{1.16}$$

Up to this point, all DFT equations are formally exact. However, the main drawback of the KS-DFT method lies within the knowledge of the $E_{XC}[\rho]$, for which only approximate expressions are known. The first approach, called "Local Density Approximation" (LDA) [18, 19], is derived from the homogeneous electron gas model. Here the exchange-correlation energy is commonly decomposed in two terms for correlation and exchange respectively. The original formulation of the exchange term is due to P. Dirac in 1930. Later in 1951 J. C. Slater proposed a modified expression for E_X^{LDA}, namely:

$$E_X^{LDA}[\rho] = -C_X \int \rho(\underline{r})^{\frac{4}{3}} d\underline{r} \tag{1.17}$$

where $C_X = \frac{3}{4}\alpha \left(\frac{3}{\pi}\right)^{\frac{1}{3}}$ and α is an adjustable parameter. In analogy to Dirac's theory α should be set to 1, while in the first derivation of Slater $\alpha = \frac{2}{3}$. According to Slater's X_α-method, α can be different.
The correlation functional E_C^{LDA} is usually defined either on analytical expressions for limiting densities or on the fitting of accurate Quantum Monte Carlo simulations [18].

Further implementations have been proposed besides the LDA, whose natural extension can be found in the so-called "Generalized- Gradient Approximation" (GGA), for which the E_{XC} is supposed to depend not only on the electronic density at a given point but also on its gradient:

$$E_{XC}^{GGA}[\rho] = \int f_{XC}\left(\rho(\underline{r}), \underline{\nabla}\rho(\underline{r})\right) d\underline{r} \tag{1.18}$$

where f_{XC} is a suitably chosen function.
In this work the GGA-DFT is in fact the level of theory employed for electronic structure calculations. Among the several expressions developed for the gradient-corrected functional, the most notable ones are the PW91 functional (J. P. Perdew *et al.* [20]), the PBE functional (J. P. Perdew *et al.* [21,22]) and the BLYP functional, which employs two formulations, one for the exchange term (A. D. Becke [23]) and one for the correlation term (C. Lee *et al.* [24]). The Perdew-Burke-Ernzerhof (PBE) exchange-correlation functional is expressed as:

$$E_{XC}^{PBE}[\rho] = \int \rho(\underline{r})(\varepsilon_X^{PBE}[\rho] + \varepsilon_C^{PBE}[\rho]) d\underline{r} \tag{1.19}$$

where ε_C^{PBE} and ε_X^{PBE} are the correlation and exchange energy densities, the latter obtained as corrections to the LDA energies in the form:

$$\varepsilon_X^{PBE} = \varepsilon_X^{LDA} \cdot F(x) \tag{1.20}$$

$$F(x) = 1 + a - \frac{a}{1 + bx^2} \tag{1.21}$$

and

$$\varepsilon_C^{PBE} = \varepsilon_C^{LDA} + H(t) \tag{1.22}$$

$$H(t) = cf_3^3 \ln\left[1 + dt^2\left(\frac{1 + At^2}{1 + At^2 + A^2t^4}\right)\right] \tag{1.23}$$

$$A = d\left[e^{-\frac{\varepsilon_C^{LDA}}{cf_3^3}} - 1\right]^{-1} \tag{1.24}$$

$$f_3(\zeta) = \frac{1}{2}\left[(1+\zeta)^{\frac{2}{3}} + (1-\zeta)^{\frac{2}{3}}\right] \tag{1.25}$$

$$t = \left[2(3\pi^3)^{\frac{1}{3}} f_3\right]^{-1} x \quad . \tag{1.26}$$

Here, x is a dimensionless density gradient while t is a variable related to it *via* the function f_3, which depends on a relative spin polarization, called ζ. It should be noted that all a, b, c and d parameters in the PBE functional are non-empirical, *i. e.* they are not obtained by fitting to experimental data. In this work, all calculations are indeed based on PBE.

It should be mentioned that further developments of DFT have been dedicated to find new and improved descriptions of the exchange- correlation functional, even beyond the GGA approach. For instance, a straightforward implementation of gradient-corrected functionals involves the inclusion of second-derivatives of the electronic density, as it is realized in "meta-GGA" functionals. Most of modern meta-GGA functionals now employ second-derivatives of the electronic kinetic energy, thus introducing a certain orbital dependence typical of more recent developments in DFT. Furthermore, other approaches have worked out expressions of the E_{XC} term by employing linear combinations of different forms, including variable portions of the pure Hartree-Fock exchange. These latter approaches all constitute the vast realm of so-called "hybrid functionals". Among these, the three-components Becke-Lee-Yang-Parr (B3LYP) [25, 26], the adjusted Perdew–Burke-Ernzerhof by Adamo and Barone (PBE0) [27] and the Heyd-Scuseria-Ernzerhof (HSE) [28] exchange-correlations functionals are some of the most employed and popular ones in the context of molecular and condensed-phase simulations.

1.3.2 DFT for periodic systems

As described above, the quantum-mechanical treatment of periodic systems often employs a plane-wave (PW) basis instead of atomic orbitals because of their inherent translational symmetry. For the KS-DFT method applied to solids, the Kohn-Sham orbitals are written in terms of the wavevector $\underline{k}$ and as a sum of basis functions, which depend on the reciprocal lattice vector $\underline{G}$:

$$\psi_{n\underline{k}}(\underline{r}) = e^{i\underline{k}\cdot\underline{r}} \sum_{\underline{G}} c_{n\underline{k}}(\underline{G}) e^{i\underline{G}\cdot\underline{r}} \tag{1.27}$$

For highly ordered systems and to perform full band structure calculations, it is necessary to evaluate many $\underline{k}$-values, but for AIMD simulations or to calculate vibrational frequencies (not phonon curves), it is sufficient to expand the KS-orbitals only at the Γ-point, $\underline{k} = 0$ as:

$$\psi_n(\underline{r}) = \sum_{\underline{G}} c_n(\underline{G}) e^{i\underline{G}\cdot\underline{r}} \tag{1.28}$$

In practical calculations it is necessary to choose a cutoff energy, E_{cut}, such that: $E_{cut} \geqslant \frac{1}{2}|\underline{G}_{max}|^2$. If band-structure calculations are performed not only at the Γ-point, the cutoff energy is expressed as: $E_{cut} \geqslant \frac{1}{2}|\underline{G}_{max} + \underline{k}_{max}|^2$. The cutoff energy sets the maximum for plane-waves kinetic energy and with that the precision of the DFT calculation, as the extent of atom-centered basis sets determines the accuracy of a "molecular" quantum chemistry calculation. An advantage of the PW basis is the expression of the kinetic-energy functional, $T[\rho]$, which can be simply formulated as:

$$T[\rho] = \frac{1}{2} \sum_{l}^{N_e} \sum_{\underline{G}} f_l(\underline{G}) |\underline{G}|^2 c_l(\underline{G}) c_l^*(\underline{G}) \tag{1.29}$$

here f_l indicates the occupancy number of each l th- KS-orbital.

It is worth to comment on the relative convergence and computational applicability of PW bases compared to atom-centered ones. In terms of how rapidly a calculation converges, since plane waves depend solely on the unit-cell parameters and not on the atoms included in it, this approach usually has a slower convergence than atom-centered basis sets. On the other hand, the already mentioned intrinsic periodicity of plane waves makes a PW basis more advantageous for periodic systems, despite the necessity to employ relatively large E_{cut} values to reach a proper convergence. Eventually, another advantage of PW bases is that they do not suffer from the "basis set superposition error" (BSSE), which usually affects calculations employing localized atom-centered basis functions.

With the exception of few examples performing all-electrons calculations, in many electronic structure codes the treatment of electrons is splitted between core and valence. Indeed, core electrons are strongly bound to a particular nucleus, while valence electrons are polarizable and take part in intermolecular interactions and in the formation of chemical bonds. The latter are treated explicitly, but core electrons may be combined with the nuclear charge by means of an effective potential, known as "pseudopotential" (PP), $v_{pp}(\underline{r})$. This terminology is commonly used in the solid-state physics community, while among quantum chemists the functional modelling of core electrons is usually called an "effective core potential" (ECP). Pseudopotentials enter the $v_{ext}(\underline{r})$ used in the equations above and are divided into two main categories: "norm-conserving" and ultrasoft PPs. The first are constructed based on two main conditions. The first states that inside a region close to the nucleus, defined by a tunable "core radius" r_c, the electron-nuclear potential is described by a suitable analytical function and the all-electron wavefunction shall be replaced by a corresponding pseudo-wavefunction. For $r < r_c$ the norm of all-electron wavefunction and pseudo-wavefunction should match. The second condition requires that in the region outside the core radius, both wavefunctions should be

identical. Ultrasoft pseudopotentials were introduced by relaxing the norm-conserving requirement and to allow calculations using the lowest possible cutoff energy for plane-wave bases [16]. An innovative strategy strictly related to plane-wave basis calculations is represented by the "projector-augmented wave" (PAW) method [29], which is usually considered a pseudopotential method, although it formally retains the treatment of all core electrons, hence providing a higher accuracy with compatible computational efficiency. In the PAW method, the main idea is to project out the rapidly oscillating components of the all-electron wavefunction inside the core radius region by using a proper projection technique. In this method, part of the all-electron wavefunction is expressed by a *smooth* term, represented using a plane-wave basis, and another part employing localized functions which act like atomic pseudo-orbitals.

1.3.3 Treatment of intermolecular van der Waals-interactions with DFT

Despite the computational efficiency and the direct applicability of Density Functional Theory for solid state and condensed phase simulations, it is known that DFT struggles to describe intermolecular forces, in particular van der Waals (vdW) interactions. In the context of physical chemistry, the term "vdW interactions" includes forces between atoms and molecules of three different kinds: permanent dipoles (also known as Keesom force), a permanent dipole and a corresponding induced one (*i.e.* Debye force) and instantaneously induced dipoles (generally known as London dispersion force). The latter has a typically non-classical origin and it is formally included in the exchange-correlation term of the energy, $E_{XC}[\rho]$. However, approximate DFT approaches, especially LDA and GGA, neglect the long-range, nonlocal correlations that give rise to the dispersive vdW-forces, because of their inherent derivation. Various innovative approaches have been developed to account for such interactions, either by empirical *a posteriori* corrections, or by formulation of novel *ad hoc* density functionals [30, 31].

In this work, where intermolecular dispersion forces play a non-negligible role to describe hydrogen bonding and adsorbate (H_2O)-surface interactions, we adopted the so-called D2-correction scheme developed by S. Grimme [32]. In this method, a dispersive energy term, E_{disp}^{D2}, describing the pair interactions between α, β-atoms is added on top of the ground state electronic energy, which is obtained by a DFT calculation. E_{disp}^{D2} has the form:

$$E_{disp}^{D2} = -\sum_{\alpha}^{N_\alpha}\sum_{\beta>\alpha}^{N_\alpha} s_6 \frac{C_{6,\alpha\beta}}{R_{\alpha\beta}^6} f(R_{\alpha\beta}) \tag{1.30}$$

where s_6 is a global scaling parameter, which has been optimized for several DFT functionals (*e.g.* for PBE, $s_6 = 0.75$), $C_{6,\alpha\beta} = \sqrt{C_{6,\alpha\alpha} C_{6,\beta\beta}}$ is the dispersion coefficient for the given atom pair (for the atom types considered in this work, Al, O and H, $C_6 = 10.79$, 0.7 and 0.14, respectively), $R_{\alpha\beta}$ is the interatomic distance, and $f(R_{\alpha\beta})$ is a Fermi-type damping function:

$$f(R_{\alpha\beta}) = \left[1 + e^{-d\left(\frac{R_{\alpha\beta}}{R_{0\alpha\beta}} - 1\right)}\right]^{-1} \tag{1.31}$$

with $R_{0\alpha\beta} = R_{0\alpha} + R_{0\beta}$ being the sum of atomic vdW-radii and d an adjustable parameter. Improvements of this method have been further developed by Grimme and coworkers, which have resulted in new correction factors and schemes: D3 [33] and, the newest, D4 [34]. In this work, the PBE DFT functional with D2 dispersion correction has been always employed.

1.4 Ab Initio Molecular Dynamics

So far the theoretical treatment of a periodic system has been described focusing on the electronic part of the Born-Oppenheimer approximation. The methodology presented is fundamental to describe the electronic structure of a given periodic system, but it doesn't provide any dynamical information, especially if one considers finite temperature behaviour.

Even within the BOA a full quantum-mechanical treatment for both electrons and nuclei is not feasible for systems with more than a few atoms. This is why approximate techniques have been developed which are focused on a mixed description: quantum mechanics for electrons and classical mechanics for nuclei. Such techniques are usually referred to as "*Ab Initio* Molecular Dynamics" (AIMD) and they may be divided into three approaches: Ehrenfest, Born-Oppenheimer and Car-Parrinello dynamics [16]. The first approach involves classical propagation of nuclear trajectories where the forces on each nucleus are calculated by the electronic Schrödinger equation. No constraints are imposed on the nature of the electronic wavefunction, hence it can correspond to different energy levels; this makes the Ehrenfest approach a "mean-field" method.
In the second approach, known as "Born-Oppenheimer" dynamics (BO-AIMD), the electronic wavefunction is minimized and nuclear forces are evaluated at each timestep, which restricts the calculated electronic eigenvalue to the ground state ψ_0 [35]. Nuclei are then propagated according to classical Newton's equations of motion:

$$M_\alpha \underline{\ddot{R}}_\alpha(t) = -\underline{\nabla}_\alpha \{\langle \psi_0 | \hat{H}_e | \psi_0 \rangle\} \quad . \tag{1.32}$$

Here the diagonalization of the electronic Hamiltonian at each t makes this approach computationally heavier than Ehrenfest dynamics but it ensures that the nuclei move classically on the ground-state state potential energy surface. In this work, the BO-AIMD method has been the favourite choice.

For the sake of completeness it is worth to mention the third approach, developed by Roberto Car and Michele Parrinello in 1985, hence the abbreviation "CPMD". It deals with a different formulation of the ground state energy, which is obtained as functional of fictitious orbitals that form the basis of the electronic wavefunction.
For both BO and CP dynamics nuclear forces can be evaluated "on the fly" using the Hellmann-Feynman theorem, for which: $-\underline{\nabla}_\alpha \langle \psi_0 | \hat{H}_e | \psi_0 \rangle \approx -\langle \psi_0 | \underline{\nabla}_\alpha \hat{H}_e | \psi_0 \rangle$. Formally, the Hellmann-Feynman theorem holds for time-independent, variational wavefunctions and for a complete orthonormal basis. Under such conditions, the relationship above is exact.

The main advantage of AIMD techniques compared to "standard" classical molecular dynamics lies within the possibility to simulate any chemical system without knowing in advance a potential function, or a force field, describing its interatomic forces. In AIMD all interactions come out directly from the quantum treatment of electrons, therefore allowing for simulations of reactive processes or phenomena where strong but fluctuating intermolecular interactions play a role, like hydrogen bonding.

Commonly to any other classical MD technique, nuclear equations of motion are solved at each timestep according to different possible schemes. The most popular algorithm to solve Newton's differential equations is the "Verlet algorithm" (here in the Störmer formalism) [16], which has been also employed for the simulations presented in this work. In this algorithm the

time-dependent position vector for each atom α may be calculated backward $(t-\Delta t)$ or forward $(t+\Delta t)$ using a Taylor expansion with timestep Δt:

$$\underline{r}_\alpha(t-\Delta t) = \underline{r}_\alpha(t) - \underline{v}_\alpha(t)\Delta t + \frac{1}{2}\underline{a}_\alpha(t)\Delta t^2 - O(\Delta t^3) \tag{1.33}$$

$$\underline{r}_\alpha(t+\Delta t) = \underline{r}_\alpha(t) + \underline{v}_\alpha(t)\Delta t + \frac{1}{2}\underline{a}_\alpha(t)\Delta t^2 + O(\Delta t^3) \tag{1.34}$$

the sum of Eqs.1.33-1.34 gives: $\underline{r}_\alpha(t+\Delta t) = 2\underline{r}_\alpha(t) - \underline{r}_\alpha(t-\Delta t) + \Delta t^2 \underline{a}_\alpha(t)$.

Therefore, the position of an atom can be propagated by simply knowing the current position, the previous one and the acceleration (which is derivable from *ab initio* forces through $\underline{F}_\alpha(t) = M_\alpha \underline{a}_\alpha(t)$). Atomic velocities may also be calculated "on the fly" for a given time t using Eq.1.35:

$$\underline{v}_\alpha(t) = \frac{1}{2\Delta t}\left[\underline{r}_\alpha(t+\Delta t) - \underline{r}_\alpha(t-\Delta t)\right] \quad . \tag{1.35}$$

The timestep entering Verlet's algorithm Δt is not only important to accurately solve nuclear equations of motion and to ensure stability of the propagated trajectories, it should also be chosen suitably in order to describe the physico-chemical process of interest. In particular, it should be small enough to catch the fastest dynamics but it should also allow to perform reasonably long trajectories. For instance, if we want to capture a molecular vibration as the O-H stretching around 3800 cm^{-1} ($\sim 10^{14}$ s^{-1}), a timestep in the order of 1 fs or less should be used. On the other hand, some phenomena may require longer propagation time to be observed, for instance conformational changes or surface diffusion reactions, which can take up to hundreds of ps or even ns. However, it should be noted that the conventional timescale which can be addressed by *ab initio* MD methods spans from fs to tens of ps. For slower processes, methods with lower computational cost such as classical force fields are advisable.

Another widely used formulation of Verlet algorithm is the so-called "velocity Verlet", which immediately requires the knowledge of both velocity and acceleration for each particle in order to propagate the trajectories:

$$\underline{r}_\alpha(t+\Delta t) = \underline{r}_\alpha(t) + \underline{v}_\alpha(t)\Delta t + \frac{1}{2}\underline{a}_\alpha(t)\Delta t^2 \tag{1.36}$$

$$\underline{v}_\alpha(t+\Delta t) = \underline{v}_\alpha(t) + \frac{1}{2}\left[\underline{a}_\alpha(t) + \underline{a}_\alpha(t+\Delta t)\right]\Delta t \quad . \tag{1.37}$$

A fundamental property of the velocity Verlet algorithm is its "symplectic" form, namely it is an integration method designed for the numerical solution of Hamilton's equations of motion for each atom α:

$$\frac{dp_{\alpha,i}}{dt} = \dot{p}_{\alpha,i} = -\frac{\partial H}{\partial q_{\alpha,i}} \tag{1.38}$$

$$\frac{dq_{\alpha,i}}{dt} = \dot{q}_{\alpha,i} = \frac{\partial H}{\partial p_{\alpha,i}} \tag{1.39}$$

where $q_{\alpha,i}$ and $p_{\alpha,i}$ are the ith-Cartesian components (x, y or z) of position and momentum coordinates respectively. The velocity Verlet algorithm is actually the one employed in this work.

The algorithm ensures total energy ($H = T + V$) conservation during the course of propagation. In the context of statistical mechanics this type of dynamics is known as "microcanonical", or NVE, where N stands for the total number of particles (atoms), V for the volume of the system (or simulation box) and E for the total energy. In the microcanonical ensemble, which represents an isolated non-interacting system, those thermodynamic quantities are constant. NVE-molecular dynamics involves full conservation of total energy, hence the dynamics is deterministic.

In order to simulate processes at finite temperature, other MD techniques are available. Such techniques are generally referred to as "canonical" dynamics, since they are related to the canonical (NVT) statistical ensemble. Here, the temperature T is often mantained constant by letting the system interact with a thermal bath, or "thermostat". Practically, this is achieved by including one or more degrees of freedom which act on the thermal reservoir, so that the trajectories are carried out for this "extended" system. In this kind of simulations the total energy is not conserved, and it is allowed to flow continously from the reservoir to the system and back. The thermal bath has a certain "thermal inertia" Q which is proper of any thermostat and most of NVT-MD techniques depend on the control of such parameter (the dimensions of Q are J s^2 so it's an energy $\times$ time^2).
Among these thermostatting techniques, the Nosé-Hoover method [36–38] successfully allows to propagate canonical trajectories and it has also been employed in this work. The Nosé-Hoover scheme involves the solution of modified Hamilton's equations of motion, where an additional fictitious coordinate is introduced to mimic the effect of the thermostat:

$$\dot{\underline{q}}_\alpha = \frac{\underline{p}_\alpha}{m_\alpha} \tag{1.40}$$

$$\dot{\underline{p}}_\alpha = \underline{F}_\alpha - \frac{p_\eta}{Q}\underline{p}_\alpha \tag{1.41}$$

$$\dot{\eta} = \frac{p_\eta}{Q} \tag{1.42}$$

$$\dot{p}_\eta = \frac{\underline{p}_\alpha \cdot \underline{p}_\alpha}{m_\alpha} - g k_B T \tag{1.43}$$

and the resulting modified single-particle Hamiltonian is formulated as:

$$H^{NH} = \frac{\underline{p}_\alpha^2}{2m_\alpha} + V(\underline{q}_\alpha) + \frac{p_\eta^2}{2Q} + g k_B T \eta \quad . \tag{1.44}$$

Here, T is the prescribed temperature and g stands for the number of degrees of freedom, typically $g = 3N - 3$ [16]. η is a dimensionless parameter and the relation $\dot{\eta} = p_\eta / Q$ may be recognized as a dynamical friction coefficient, which represents the coupling with the reservoir. It is important to underline that because of this modified energy formulation, Nosé-Hoover equations of motion don't follow Hamiltonian dynamics. However, it is possible to retrieve from H^{NH} a distribution function with the same characteristics are the canonical partition function, hence to mantain the same thermodynamic properties of the NVT-ensemble.

The initial atomic velocities of an NVT-MD trajectory are typically generated randomly according to the Boltzmann distribution at a given temperature, it is therefore necessary to propagate long enough simulations so that the system properly reaches the desired thermal equilibrium. Moreover, because of the non-Hamiltonian behaviour of Nosé-Hoover trajectories,

multiple sets of MD runs have to be launched together in order to achieve reliable statistical information.

2 Theory and Computation of Vibrational Frequencies and Spectroscopy

All integral laws of spectral lines and of atomic theory spring originally from the quantum theory. It is the mysterious organon on which Nature plays her music of the spectra, and according to the rhythm of which she regulates the structure of the atoms and nuclei.

Arnold Sommerfeld

2.1 Static quantum-chemical approach for vibrational analysis

In the Born-Oppenheimer picture, the solution of the electronic TISE generates potential energy surfaces which parametrically depend on nuclear coordinates. Moreover, such potential energy U can be expanded as a Taylor series of $3N$ atomic displacements, $x_i = R_i - R_{i,0}$, where N ($= N_\alpha$ as indicated above) is the number of atoms and R_i is one of the ith-atomic (Cartesian) coordinates [13]:

$$U = U_0 + \sum_i^{3N} \left(\frac{\partial U}{\partial x_i}\right)_0 x_i + \frac{1}{2}\sum_{i,j}^{3N} \left(\frac{\partial^2 U}{\partial x_i \partial x_j}\right)_0 x_i x_j + O(x_i^3) \tag{2.1}$$

where U_0 indicates the minimum (or equilibrium geometry) of the potential energy for zero displacements, $x_i = 0$.

In the harmonic approximation, namely for small displacements around the minimum, the potential becomes: $U = \frac{1}{2}\sum_{i,j}^{3N} \left(\frac{\partial^2 U}{\partial x_i \partial x_j}\right)_0 x_i x_j$, where the second derivatives assume the meaning of a generalized force constant. One can also introduce mass-weighted coordinates, $Q_i = \sqrt{M_i} x_i$, so that the potential energy assumes the equivalent form: $U = \frac{1}{2}\sum_{i,j}^{3N} \left(\frac{\partial^2 U}{\partial Q_i \partial Q_j}\right)_0 Q_i Q_j$. Conversely, one can express the kinetic energy operator $\hat{T}$ in this new set of coordinates, leading to the simplified form: $\hat{T} = \frac{1}{2}\sum_i^{3N} \dot{Q}_i^2$.

All second derivatives of the potential form the elements of the so-called Hessian matrix, $H_{ij} = \left(\frac{\partial^2 U}{\partial Q_i \partial Q_j}\right)$. By solving the eingenvalue problem $\underline{\underline{H}}\underline{A}_k = \lambda_k \underline{A}_k$ we can obtain "Normal Modes" [13] in terms of their eigenvalues, harmonic frequencies $\omega_k = \lambda_k^2$, and eigenvectors $\underline{A}_k$. At the same time, harmonic energies of quantized vibrational levels are obtainable, following the well-known expression: $E_k^v = (v + \frac{1}{2})\hbar\omega_k$, where v is the vibrational quantum number.
Hessian eigenvalues can be particularly useful also to characterize a given molecular geometry associated with the calculated potential: if all eigenvalues are positive ($\lambda_k \geq 0$, $\forall k$) then the considered structure corresponds to a minimum in the potential energy surface; if one and only one eigenvalue is negative, hence there is an imaginary frequency, the structure corresponds to a first-order saddle point in the multidimentional PES, which chemically is associated to a

"transition state".
Harmonic frequencies, vectors and energies obtained from diagonalization of the Hessian matrix are the constituents of Normal Mode Analysis (NMA) and they represent the first tool of quantum chemical methods to describe molecular vibrations, from gas-phase to solid-state systems. For periodic systems, as performed in this work, NMA can be done by numerical calculations of the Hessian matrix and subsequent diagonalization using finite atomic differences. Normal mode frequencies and eigenvectors are obtained only at the Γ-point, so that only vibrations localized in each unit cell can be determined. In fact, to obtain phonon dispersion curves a wider $\underline{k}$-points sampling would be necessary.
The NMA procedure suffers from several methodological drawbacks [13], which we shall mention in what follows.

First of all, relying on the harmonic approximation for the nuclear potential usually holds for vibrations which don't involve a major displacement from the (real) equilibrium structure. Moreover, if a vibrational transition between the ground and an excited state is very energetic, then the deviation from harmonic vibrational levels will be important. This inconvenience of NMA is known as "anharmonicity" and it may be solved by assuming a different shape of the potential energy function, for instance a Morse potential. Another source of anharmonicity can be included by taking couplings among different Normal Modes.
Another disadvantage of NMA consists in the total lack of spectroscopic intensities and linewidths. In fact, a vibrational transition is typically probed by the interaction with infrared (IR) light which brings the system from the ground state to a vibrational excited state. The linewidth of the involved vibrational resonance is inversely proportional to phase and energy relaxation times, the latter related to the finite lifetime of the excited state. The dephasing time is usually much faster than vibrational relaxation and dominates the width of the vibrational peak [13,39]. The strength and probability of such IR transition can be estimated from the derivative of the electrical dipole moment $\underline{\mu}$ with respect to the involved atomic displacements, also known as "dynamical dipole moment". As for the potential U, $\underline{\mu}$ can also be expanded as a series of mass-scaled coordinates:

$$\underline{\mu} = \underline{\mu}_0 + \sum_{i}^{3N} \left(\frac{\partial \underline{\mu}}{\partial Q_i} \right)_0 Q_i + \frac{1}{2} \sum_{i,j}^{3N} \left(\frac{\partial^2 \underline{\mu}}{\partial Q_i \partial Q_j} \right)_0 Q_i Q_j + O(Q_i^3) \tag{2.2}$$

In order to calculate the probability of a vibrational transition acting on a given coordinate (or mode) Q_i, the following expectation value can be calculated using the double-harmonic approximation (*i.e.* neglecting both the anharmonicity of the potential energy surface and the nonlinear relationship of the dipole moment to the normal mode coordinate), as:

$$\langle k|\underline{\mu}|l\rangle \approx \left(\frac{\partial \underline{\mu}}{\partial Q_i} \right)_0 \langle k|Q_i|l\rangle \tag{2.3}$$

where $|k\rangle$ and $|l\rangle$ are the respective vibrational eigenstates involved in the transition of ith-oscillator. If the displacement along coordinate Q_i is accompanied by a change in the electrical dipole moment, hence $\partial\underline{\mu}/\partial Q_i \neq \underline{0}$, the system will interact with infrared radiation, allowing the vibrational kl-transition to occurr. Otherwise, if changes within a Normal Mode coordinate leave the dipole vector the same ($\partial\underline{\mu}/\partial Q_i = \underline{0}$), no vibrational excitation will happen and the given mode Q_i will be called "IR inactive". Group theory and molecular symmetry considerations

can further help to determine *a priori* if a vibrational mode will be IR active or not; however, from the energetic point of view, selection rules for IR absorption or emission require that the spacing between initial and final vibrational levels should match: $v_l - v_k = \Delta v_{kl} = \pm 1$ [39].

A different kind of vibrational transitions may be measured by Raman spectroscopy and there another property of the system is involved: the polarizability, $\underline{\underline{\alpha}}$. As for the dipole vector, also the polarizability tensor can be expanded as a Taylor series of atomic displacements:

$$\underline{\underline{\alpha}} = \underline{\underline{\alpha}}_0 + \sum_i^{3N} \left(\frac{\partial \underline{\underline{\alpha}}}{\partial Q_i} \right)_0 Q_i + \frac{1}{2} \sum_{i,j}^{3N} \left(\frac{\partial^2 \underline{\underline{\alpha}}}{\partial Q_i \partial Q_j} \right)_0 Q_i Q_j + O(Q_i^3) \tag{2.4}$$

By employing a similar argument as done for the electrical dipole moment, it can be shown that a Raman transition requires a change of the polarizability along a Normal Mode coordinate Q_i: $\partial \underline{\underline{\alpha}} / \partial Q_i \neq \underline{\underline{0}}$. In this case the Q_i-coordinate will be Raman active [39].

Other sorts of vibrational excitations may happen, but are quite rare, for instance "overtones" and "combination bands". The first happens when anharmonicity of a given vibrational coordinate is involved and it allows for double vibrational transitions, *i.e.* for transitions characterized by $\Delta v_{kl} = 2$. This is often observed with H_2O, where the overtone of its bending vibration can be found. A combination band, on the other hand, is a vibrational transition where two coupled coordinates Q_i and Q_j are simultaneously excited.

Another critical issue concerning vibrational frequencies obtained from Normal Mode Analysis consists in the static approach which is intrinsic of this method. As we have described so far, the diagonalization of the Hessian matrix allows to calculate harmonic frequencies and eigenvectors for a given point in the potential energy surface. This calculation is usually performed for a geometry corresponding to a minimum of the PES. However, in reality and in experiment any vibrational spectrum may be related to a variety of structures, a manifold of phase space points whose populations are governed by the Boltzmann distribution at a given temperature. It is therefore imperative to go beyond the static ($T = 0$ K) picture of Normal Mode Analysis and to include the structural dynamics which often determines spectral features. There are several effects which are missing in NMA, to a name a few: line broadening (homogeneous or inhomogeneous), thermal fluctuations and (inter)mode couplings. Within the framework of *ab initio* molecular dynamics most of these effects are retrievable [35]. But how to simulate a vibrational spectrum from classical trajectories? We need first to introduce the concept of correlation functions.

2.2 Time-correlation functions approach for vibrational analysis

In statistical mechanics, time-correlation functions are tools to convey dynamical information about a system [40, 41]. The main assumption is that such a system shall be in a stationary state, or in thermodynamic equilibrium. Let us consider a dynamical variable $A(t)$ connected to a time-dependent observable, for instance the molecular dipole moment $\underline{\mu}(t)$ associated with the absorption lineshape. In the Heisenberg picture of quantum mechanics (assuming a thermal ensemble distribution), the time-average of classical $A(t)$ shall correspond to the time-dependent expectation value of operator $\hat{A}(t) = e^{i\hat{H}t/\hbar} \hat{A} e^{-i\hat{H}t/\hbar}$:

$$\langle \hat{A} \rangle(t) = \mathrm{Tr}\{\hat{\rho}\hat{A}(t)\} \tag{2.5}$$

where $\hat{\rho}$ represents here the time-independent density operator, which in thermal equilibrium can be written in terms of the Boltzmann-weighted eigenstates of our system: $\hat{\rho} = e^{-\hat{H}/k_BT}/\mathrm{Tr}\{e^{-\hat{H}/k_BT}\} = Q^{-1}\sum_j e^{-\varepsilon_j/k_BT}|\psi_j\rangle\langle\psi_j|$, with $Q = \mathrm{Tr}\{e^{-\hat{H}/k_BT}\}$ being the canonical partition function.
In classical statistical mechanics, the fundamental hypothesis about $A(t)$ is that its time average $\langle A \rangle_t$ and its ensemble average $\langle A \rangle_e$ should be identical, where:

$$\langle A \rangle_t = \lim_{t\to\infty} \frac{1}{2t} \int_{-t}^{t} A(t')dt' \tag{2.6}$$

$$\langle A \rangle_e = \lim_{n\to\infty} \frac{1}{n} \sum_{i=1}^{n} A_i \tag{2.7}$$

considering an ensemble of n macroscopically identical systems. Such hypothesis is also called "ergodic theorem" and it holds for conservative systems.
Being a function of time as well as of positions and momenta, $\underline{q}$ and $\underline{p}$, the average at time t of observable A is given by the phase-space integral:

$$\langle A \rangle(t) = \int d\underline{q} \int d\underline{p} f(\underline{q}, \underline{p}, t) A(\underline{q}, \underline{p}) \tag{2.8}$$

where $f(\underline{q}, \underline{p}, t)$ is a phase-space distribution function.

For a system evolving according to Hamilton's equations, A depends on variable positions and momenta at each time, $A(\underline{q}(t), \underline{p}(t))$, although its average is uniquely determined by the initial conditions $[\underline{q}(0), \underline{p}(0)]$:

$$\langle A \rangle(t) = \int d\underline{q} \int d\underline{p} f(\underline{q}, \underline{p}, 0) A(\underline{q}(t), \underline{p}(t)) \quad . \tag{2.9}$$

This also involves that f does not change with time. In fact, under the assumption of thermal equilibrium, the distribution function can be written as: $f(\underline{q}, \underline{p}) = Q^{-1} e^{-H(\underline{q},\underline{p})/k_BT}$ (in analogy with the density operator).

Let us consider now a second dynamical variable $B(t) = B(\underline{q}(t), \underline{p}(t))$. For both $A(t)$ and $B(t)$ we can define a "correlation function" C_{AB}:

$$C_{AB}(t_1, t_2) = \int d\underline{q} \int d\underline{p} f(\underline{q}, \underline{p}) A(\underline{q}(t_1), \underline{p}(t_1)) \cdot B(\underline{q}(t_2), \underline{p}(t_2)) = \langle A(t_1) \cdot B(t_2) \rangle \quad . \tag{2.10}$$

If we define $t = t_2 - t_1$, we find:

$$C_{AB}(t_1, t_2) = \langle A(t_1) \cdot B(t_1 + t) \rangle = C_{AB}(t_1, t_1 + t) \tag{2.11}$$

but since for a stationary state the origin of time is not crucial, that is we can assume $t_1 = 0$ without loss of generality, we have:

$$C_{AB}(t) = \langle A(0) \cdot B(t) \rangle \quad . \tag{2.12}$$

Hence, a correlation function always depends on the time difference between the two "measurements".

Correspondingly, we can also define an "autocorrelation function" of $A(t)$ as:

$$C_{AA}(t) = \langle A(0) \cdot A(t) \rangle = \tag{2.13}$$
$$= \langle A(t') \cdot A(t'+t) \rangle = \tag{2.14}$$
$$= \lim_{t\to\infty} \frac{1}{2t} \int_{-t}^{t} A(t')A(t'+t)dt' \tag{2.15}$$

where the brackets "$\langle ... \rangle$" introduced above mean an equilibrium ensemble average.

The autocorrelation function $C_{AA}(t)$ has three important properties which can be derived from the above assumptions, including ergodicity [40, 41]:

1. From stationarity condition: $C_{AA}(t) = C_{AA}(-t)$, *i.e.* classical autocorrelation functions are symmetrical with respect to time. This is only valid for a classical system, while in quantum mechanics such condition is not necessarily true.

2. From Schwarz's inequality: the magnitude of an autocorrelation function is never larger than its initial value: $|C_{AA}(t)| \leq |C_{AA}(0)|$.

3. The Fourier transform of $C_{AA}(t)$, $\tilde{C}_{AA}(\omega)$, is called "power spectrum" or "spectral function" of variable $A(t)$:
$$\tilde{C}_{AA}(\omega) \propto \int_{-\infty}^{+\infty} C_{AA}(t)e^{-i\omega t}dt \tag{2.16}$$
and, from the Wiener-Khintchine theorem, we have: $\tilde{C}_{AA}(\omega) \geq 0$.

A typical correlation function of interest for vibrational spectroscopy and which is directly computable from classical MD trajectories is the "velocity-velocity autocorrelation function" (VVAF), $C_{vv}(t)$ [16, 35, 40, 42, 43]:

$$C_{vv}(t) = \frac{1}{N} \sum_{i}^{N} \langle \underline{v}_i(0) \cdot \underline{v}_i(t) \rangle \tag{2.17}$$

where $\underline{v}_i$ indicates the velocity vector of the ith-atom in the dynamics. The power spectrum of VVAF is called "Vibrational Density of States" (VDOS):

$$\mathrm{VDOS}(\omega) \propto \int_{0}^{+\infty} C_{vv}(t)\cos(\omega t)dt \quad . \tag{2.18}$$

In Eq.2.18 the integral is performed only with respect to positive time thanks to the aforementioned symmetrical properties of classical correlation functions such as the VVAF. In fact, it can be easily shown that since $C_{vv}(t) = C_{vv}(-t)$ for a system in thermal equilibrium, the full Fourier transform (from $-\infty$ to $+\infty$) can be simplified to the solely cosine transform. This is also related to a further property of correlation functions which are even functions of time like the VVAF: only the real part, $Re\{\tilde{C}_{vv}(\omega)\}$ is meaningful and corresponds to the Vibrational Density of States.

2.3 Basics of vibrational IR and SFG spectroscopy

At this point we shall derive a theoretical treatment of vibrational spectra and their relation to classical AIMD trajectories. To do so, we first need to introduce the fundamental relations that allow to describe the absorption of infrared radiation. In general, when a material is subject to an electric field, an induced polarization density $\underline{P}(t)$ is generated, which is proportional to the applied field' strength $\underline{E}(t)$ [13,44]. In fact, the macroscopic polarization (here expressed along a certain Cartesian axis a) can be written as a sum of linear and non-linear terms:

$$P_a(t) = \epsilon_0 \left[\sum_b \chi^{(1)}_{ab} E_b(t) + \sum_{bc} \chi^{(2)}_{abc} E_b(t) E_c(t) + ... \right] = \tag{2.19}$$

$$= P^{(1)}_a(t) + P^{(2)}_a(t) + ... \tag{2.20}$$

where ϵ_0 is the permittivity of vacuum, while $\chi^{(1)}_{ab}$ and $\chi^{(2)}_{abc}$ are the ab- and abc-elements of the so-called "first-order" and "second-order" optical susceptibilities, where abc indicate a general set of Cartesian components. Such abc indices may be related to the direction of the applied electric fields as well as to the intrinsic coordinates of the material. Both optical susceptibilities $\underline{\underline{\chi}}^{(1)}$ and $\underline{\underline{\underline{\chi}}}^{(2)}$ are tensors (of second- and third-rank, respectively) describing the interaction between a material and the applied fields, which results in the induced first-order and second-order polarizations.
The first-order, or linear approximation is valid to describe one-photon absorption processes as after excitation with infrared light in conventional vibrational IR spectroscopy. On the other hand, the second-order polarization is needed to describe non-linear spectroscopic techniques, like in the case of the Sum Frequency Generation (SFG) spectroscopy, which consists of a two-photon process (in absorption) and is considered as the reference experimental methodology in this work. Experimentally, this second-order technique occurs when two incoming laser pulses (with fixed frequencies, ω_1 and ω_2) are interacting with a material *via* its susceptibility $\underline{\underline{\underline{\chi}}}^{(2)}$. The material reacts upon illumination by emitting a third pulse with frequency $\omega_3 = \omega_1 + \omega_2$, hence the name "Sum Frequency Generation" [44–49].

We should now consider the properties of the second-order susceptibility tensor, in particular its symmetry, which are closely related to the "surface specificity" of the SFG technique [46]. The third-rank tensor $\chi^{(2)}_{abc}$ has a maximum of 27 components, although the number of which are effectively determining the induced polarization in an SFG experiment may be less. In fact, the symmetry of the propagating medium (material) strongly affects the properties of $\chi^{(2)}_{abc}$. For instance, in a centrosymmetric (or isotropic) material, all directions are equivalent, and this implies: $\chi^{(2)}_{abc} = \chi^{(2)}_{-(abc)}$, where $-(abc)$ indicate opposite directions. At the same time, being a third-rank tensor, $\chi^{(2)}_{abc}$ must change sign when reversing axis system, so that: $\chi^{(2)}_{abc} = -\chi^{(2)}_{-(abc)}$. To satisfy this condition, the second-order susceptibility must be 0 for a centrosymmetric environment, as a bulk material, hence the SFG signal will also be zero.
Although the majority of bulk phases are centrosymmetric, the boundary between two materials is inherently anisotropic and, therefore, may be SFG active. For instance, a isotropic planar surface (about the xy-plane) can be considered symmetric around the surface normal (z-axis) and thus contains a C_∞ rotation axis: in these conditions we have $z \neq -z$ but $x = -x$ and $y = -y$ [46]. Under such symmetry conditions, the $\chi^{(2)}_{abc}$ tensor has only four independent

non-zero components: $\chi^{(2)}_{zxx}(=\chi^{(2)}_{zyy})$, $\chi^{(2)}_{xzx}(=\chi^{(2)}_{yzy})$, $\chi^{(2)}_{xxz}(=\chi^{(2)}_{yyz})$ and $\chi^{(2)}_{zzx}(=\chi^{(2)}_{zzy})$. It should be noted that for different symmetry characters than C_∞ given by different unit-cell structures, the non-zero elements of $\chi^{(2)}_{abc}$ may be different.

Experimentally, several combinations of incoming pulses can be achieved, leading to different spacial polarizations of the illuminated material and also related to different contributions of the $\chi^{(2)}_{abc}$ tensor elements. These distinct elements can in fact be probed by using two different polarizers for the applied electric fields, one for the field vector perpendicular to the plane of incidence, labeled *s* (from the German "Senkrecht"), and one for the field vector parallel to the plane of incidence, labeled *p*. Four combinations are sufficient: *ppp*, *ssp*, *sps*, *pss*, with the letters listed in decreasing frequency, where the first is for the emitted Sum Frequency pulse. Among these, the spectral response associated with *ssp* polarization is the most straightforward to relate to the second-order susceptibility. Indeed, the SFG intensity within such scheme is directly proportional to the $\chi^{(2)}_{xxz}$ element.

The derivations presented so far are specifically appropriate for a system containing adsorbed molecules on a surface which is SFG inactive. However, if the underlying substrate is also SFG active, an additional susceptibility to describe its nonlinear optical response is required. The substrate susceptibility is termed as $\chi^{(2),NR}_{abc}$, where the NR subscript refers to its non-resonant nature. Because the susceptibility used so far ($\chi^{(2)}_{abc}$) is related solely to the resonant behaviour of the interfacial adsorbed molecules, it is renamed $\chi^{(2),R}_{abc}$. A generic description of the response of the interface to applied $\underline{E}$-field vectors is, therefore, given by: $\chi^{(2)}_{abc} = \chi^{(2),R}_{abc} + \chi^{(2),NR}_{abc}$ [44,46].

In the context of this work, the resonant contribution to the second-order susceptibility is associated with vibrational excitations within the fundamental electronic states of molecular chromophores present at the interface, hence the general nomenclature SFG is now changed to Vibrational Sum Frequency (VSF) generation, to emphasize the ability to probe vibrational transitions associated with this surface-sensitive spectroscopic technique. From a technical point of view, the VSF experiment is achievable by chosing the frequency of the incoming pulses within the IR (wavelength between 700 nm and 1 mm) and the Visible (wavelength between 400 nm and 700 nm) spectral ranges. The IR pulse of frequency ω_{IR} shall be resonant with vibrational transitions (most importantly between ground and first excited states $v(0 \rightarrow 1)$) while the second pulse of frequency ω_{VIS} shall simply bring the excited chromophores to a higher virtual vibrational state. As expected, the emitted pulse will have a frequency $\omega_{VSF} = \omega_{IR} + \omega_{VIS}$.

In Fig.2.1, a schematic representation of a VSF experiment is shown for a typical *adsorbate + surface* system. In particular, it is highlighted that only the interfacial region is characterized by a non-zero value of $\chi^{(2)}$, hence adsorbates vibrations are detectable and not bulk vibrations. A corresponding energy representation for VSF spectroscopy is also reported.

Very often, the experimental treatment of the VSF lineshape considers a Lorentzian form where each chromophore contributes to the resonant part of the optical response. Each *abc*-element of the second-order susceptibility can be therefore phenomenologically represented as:

$$\chi^{(2)}_{abc} = \chi^{(2),NR}_{abc} + \sum_q \frac{A_{abc,q}}{(\omega_{IR} - \omega_q - i\Gamma_q)} \quad . \tag{2.21}$$

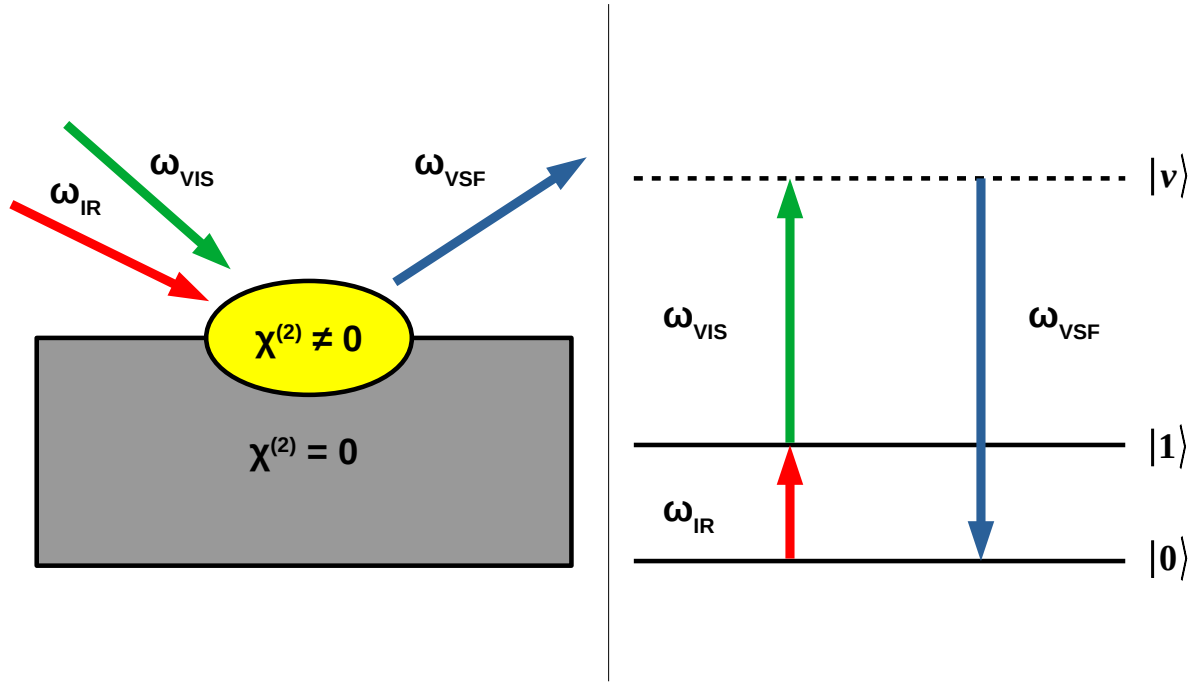

Figure 2.1: Left panel: Representative scheme of Vibrational Sum Frequency generation spectroscopy for adsorbates on a surface, where two incoming laser pulses are shined on the solid, one in the IR region (resonant with vibrational transitions) and one in the VIS region. A third outcoming laser pulse is emitted with corresponding frequency $\omega_{VSF} = \omega_{IR} + \omega_{VIS}$. Right panel: Energy representation of the VSF experiment. The IR pulse here is taken to be resonant with the $v = 0 \rightarrow v = 1$ vibrational transition. The VIS pulse provides a further excitation to a virtual vibrational state v, so that the emitted VSF pulse corresponds to the downward transition to the initial vibrational state.

Here, index q correspond to each resonant vibrational mode probed by SFG, $A_{abc,q}$ is a parameter related to the strength of the vibrational transition and to the nature of the vibrational mode involved for a certain polarization, while Γ_q is a damping constant specific of each mode.
As it can be easily noticed from Eq.2.21, the second-order susceptibility is an intrinsic complex quantity, which possesses a real and an imaginary part:

$$Re\{\chi^{(2)}_{abc}\} = \chi^{(2),NR}_{abc} + \sum_q \frac{A_{abc,q}\,(\omega_{IR} - \omega_q)}{(\omega^2_{IR} - \omega_q)^2 + \Gamma^2_q} \tag{2.22}$$

$$Im\{\chi^{(2)}_{abc}\} = \sum_q \frac{iA_{abc,q}\Gamma_q}{(\omega^2_{IR} - \omega_q)^2 + \Gamma^2_q} \quad . \tag{2.23}$$

In experiment, the total VSF lineshape, consisting of both resonant and non-resonant contributions can be measured by means of so-called "homodyne detection". However, recent developments allow to determine also the imaginary part of $\chi^{(2)}$, using the "heterodyne" technique.

At this point is necessary to explain how different elements $\chi^{(2)}_{abc}$ of the second-order susceptibility can be related to the measured intensity of a VSF experiment, I^{VSF}, within the main

polarization combinations (*ppp*, *ssp*, *sps* and *pss*). In general, the VSF intensity can be related to [12, 44]:

$$I^{VSF}(\omega_{IR}) = \frac{8\pi^3\omega_{VSF}}{c^3\cos^2\theta_{VSF}}|\chi^{(2)}_{eff}|^2 I^{VIS} I^{IR}(\omega_{IR}) \tag{2.24}$$

where the intensity of the emitted VSF field is a function of the frequency of the incident infrared, ω_i is the frequency of the ith-field, c is the speed of light in vacuum, θ_{VSF} is the angle of the wave vector of the reflected VSF field with respect to the surface normal, I^{VIS} is the intensity of the visible field and $I^{IR}(\omega_{IR})$ is the intensity of the incident infrared, which is frequency dependent. With the exception of $\chi^{(2)}_{eff}$, which consists of a properly scaled susceptibility for a given polarization and contains all sample specific information, all these parameters are either under the control of the experimentalist or are physical constants. Here, we report the expression for $\chi^{(2)}_{eff}$ for two main polarization schemes, *ppp* and *ssp*, for an azimuthally isotropic surface, where only four $\underset{\equiv}{\chi}^{(2)}$-tensor elements are contributing to the VSF signal:

$$\chi^{(2)}_{eff,ssp} = L_{yy}(\omega_{VSF})L_{yy}(\omega_{VIS})L_{zz}(\omega_{IR})\sin\theta_{IR}\chi^{(2)}_{yyz} \tag{2.25}$$

$$\chi^{(2)}_{eff,ppp} = -L_{xx}(\omega_{VSF})L_{xx}(\omega_{VIS})L_{zz}(\omega_{IR})\cos\theta_{VSF}\cos\theta_{VIS}\sin\theta_{IR}\chi^{(2)}_{xxz} \tag{2.26}$$

$$- L_{xx}(\omega_{VSF})L_{zz}(\omega_{VIS})L_{xx}(\omega_{IR})\cos\theta_{VSF}\sin\theta_{VIS}\cos\theta_{IR}\chi^{(2)}_{xzx} \tag{2.27}$$

$$+ L_{zz}(\omega_{VSF})L_{xx}(\omega_{VIS})L_{xx}(\omega_{IR})\sin\theta_{VSF}\cos\theta_{VIS}\cos\theta_{IR}\chi^{(2)}_{zxx} \tag{2.28}$$

$$+ L_{zz}(\omega_{VSF})L_{zz}(\omega_{VIS})L_{zz}(\omega_{IR})\sin\theta_{VSF}\sin\theta_{VIS}\sin\theta_{IR}\chi^{(2)}_{zzz} \quad . \tag{2.29}$$

Due to the surface symmetry, $\chi^{(2)}_{yyz} = \chi^{(2)}_{xxz}$, so the latter will be employed from now on. It clearly emerges that the *ssp*-polarized VSF signal is the easiest one to be computed, since it requires only one component of the susceptibility tensor. All $L_{ab}(\omega_i)$ elements are known as "Fresnel coefficients" [44] and they are dependent on the geometry of the laser settings and on the refractive index of the material within the considered frequency ranges.

2.3.1 Microscopic theory of IR and VSF spectroscopy

We shall now move towards a microscopic description of both IR and Vibrational Sum Frequency generation optical responses and, in particular, how the quantum-mechanical theory of first-order $\chi^{(1)}_{ab}$ and second-order $\chi^{(2)}_{abc}$ can be related to classical correlation functions.
As expressed for the *static* vibrational response, the microscopic electrical dipole $\underline{\mu}$ allows for the interaction of a molecule, or a material, with light to occurr.
However, as we wrote previously for the macroscopic polarization vector, which is indeed a polarization density (dipoles per unit of volume), we can expand the electrical dipole moment as a Taylor series in terms of applied field strength along a general Cartesian axis a (where $a = x, y$ or z) [13]:

$$\mu_a = \mu^{(0)}_a + \sum_b \alpha_{ab}E_b + \frac{1}{2}\sum_{bc}\beta_{abc}E_bE_c + ... \quad . \tag{2.30}$$

Here α_{ab} is the ab-element of the second-rank polarizability tensor, while β_{abc} is the corresponding abc-element of another optical property, known as "first hyperpolarizability". The first term of the sum, $\mu^{(0)}_a$ is the permanent dipole moment of the system.

We can immediately recognize a certain similarity between the macroscopic case described above for the induced polarization $\underline{P}$ and the microscopic one, where we have introduced the dipole vector, the polarizability and the first hyperpolarizability tensors as mediating entities in the interaction between a quantum mechanical system and an electric field. These microscopic properties are responsible for individual transitions within vibrational spectroscopy, in particular the microscopic hyperpolarizability β_{abc} can be related to the corresponding macroscopic susceptibility, hence to the VSF signal intensity.

In the context of small external perturbations, *i.e.* first-order perturbation theory, and in the limit of vibrational resonance, we can derive quantum-mechanical expressions for both IR and VSF optical responses by means of the first- and second-order susceptibilities [50]:

$$\chi^{(1)}_{ab}(\omega) = \sum_{v,v'} \left[\frac{\langle v|\mu_a|v'\rangle\langle v'|\mu_b|v\rangle}{\omega_{vv'} - \omega - i\Gamma_{vv'}} \right] \rho_{vv} \tag{2.31}$$

where ω is the characteristic frequency of the IR field (we have omitted the index for symplicity), considered to be resonant with vibrational transitions, while v, v' are labels of the vibrational states involved in the IR excitation and $\Gamma_{vv'}$ is a damping factor related to the finite lifetime of the given vibrational excited state. Eventually, ρ_{vv} is the vth-diagonal element of the density matrix in thermal equilibrium, where $\rho_{vv} = e^{-\frac{\hbar\omega_v}{k_BT}}/\sum_u e^{-\frac{\hbar\omega_u}{k_BT}}$.
Conversely, for the second-order response we have:

$$\chi^{(2)}_{abc}(\omega) = \sum_{v,v'} \left[\frac{\langle v|\alpha_{ab}|v'\rangle\langle v'|\mu_c|v\rangle}{\omega_{vv'} - \omega - i\Gamma_{vv'}} \right] \rho_{vv} \quad . \tag{2.32}$$

Here, α_{ab} is the ab-element of the Raman polarizability tensor, which has been incorporated in the $\underline{\underline{\chi}}^{(2)}$ expression.
The frequency-dependent expression in Eqs.2.31,2.32 can be rewritten in a quantum time-correlation function formalism by virtue of the relationship: $\int_0^\infty dt e^{i(\omega_{vv'} - \omega - i\Gamma_{vv'})} = i(\omega_{vv'} - \omega - i\Gamma_{vv'})^{-1}$, so that:

$$\chi^{(1)}_{ab}(\omega) = i\int_0^\infty dt \sum_{v,v'} e^{i(\omega_{vv'} - \omega - i\Gamma_{vv'})t} \langle v|\mu_a|v'\rangle\langle v'|\mu_b|v\rangle\rho_{vv} \tag{2.33}$$

$$= i\int_0^\infty e^{-i\omega t} dt \sum_{v,v'} \langle v|e^{i\hat{H}t}\mu_a e^{-i\hat{H}t}|v'\rangle\langle v'|\mu_b|v\rangle\rho_{vv} \tag{2.34}$$

$$= i\int_0^\infty e^{-i\omega t} dt \sum_{v,v'} \langle v|\mu_a(t)|v'\rangle\langle v'|\mu_b|v\rangle\rho_{vv} \quad . \tag{2.35}$$

Same treatment reported in Eq.2.33 shall be applied to the Raman polarizability element α_{ab} to write an analogous of $\chi^{(2)}_{abc}$ [50].

Under the assumption of describing vibrational transitions for a system in thermal equilibrium, as represented by ρ_{vv}, the quantum-mechanical treatment of IR and VSF responses can be translated in a classical way by means of the statistical mechanics analogue of "linear response theory" [40]. By employing Kubo's "fluctuation-dissipation theorem" [40,51] we can relate each of the vibrational transitions mentioned so far to a classical time-correlation function. More specifically, the lineshape associated with an IR spectrum, $I^{IR}(\omega)$, will be determined by the

first-order optical susceptibility, the latter related to the Fourier transform of the (microscopic) "dipole-dipole" autocorrelation function [42, 43, 52]:

$$\chi_{ab}^{(1)}(\omega) \propto i \sum_{q}^{M} \int_{0}^{\infty} \langle \mu_{q,b}(0) \cdot \mu_{q,a}(t) \rangle e^{-i\omega t} dt \tag{2.36}$$

where indices a and b correspond to the Cartesian components of dipole vector, while index q spans over all vibrational chromophores of the system. Here, the $\langle \mu_a(0) \cdot \mu_b(t) \rangle$ is a classical autocorrelation function analogue of Eq.2.33, which is an even function of time, so that only the real part of its Fourier transform has a physical meaning as we noticed previously for the power spectrum of atomic velocities, VDOS.

Following the theoretical developments made by Akihiro Morita and James T. Hynes [50, 53–56], a similar classical treatment for the VSF spectral lineshape can also be done, relating $I^{VSF}(\omega)$ to the second-order optical susceptibility and this to the FT-correlation function of dipole and polarizability:

$$\chi_{abc}^{(2)}(\omega) \propto i \sum_{q}^{M} \int_{0}^{\infty} \langle \mu_{q,c}(0) \cdot \alpha_{q,ab}(t) \rangle e^{-i\omega t} dt \tag{2.37}$$

where M indicates the total number of vibrational chromophores (*i.e.* vibrational modes contributing to the VSF absorption spectrum) in the system.

It should be noted that while in Eqs.2.31-2.32 we were employing the dipole operator along certain Cartesian coordinates and the Raman transition expectation value for α_{ab}, in the Eqs.2.36-2.37 the first- and second-order susceptibilities are calculated by means of classical quantities, namely the electrical dipole vector and the polarizability tensor within the respective Cartesian components. Differently than the IR response, being related to $Re\{\chi_{ab}^{(1)}(\omega)\}$, the VSF response originates from the dipole-polarizability correlation function, which is not symmetrical with respect to time.

2.4 Computing vibrational spectra: From VDOS to VSF

2.4.1 General formalism

From the technical point of view, an object as the velocity-velocity autocorrelation function, $C_{vv}(t)$, is computed by taking the scalar product of the velocity vector of each moving atom in the simulation box within a given time shift, t [57]. Therefore, the $C_{vv}(t)$ tells us how the motion of a given atom is correlated with itself during the course of propagation. In practice, the VVAF at time t is calculated as average over number of atoms and as time-average over initial conditions t_j:

$$C_{vv}(t) = \frac{1}{N} \frac{1}{N_t} \sum_{i=1}^{N} \sum_{j=1}^{N_t} \langle \underline{v}_i(t_j) \cdot \underline{v}_i(t_j + t) \rangle \quad . \tag{2.38}$$

Here, $N_t = 1 + t_{\text{samp}}/\Delta t$ is the number of intervals within which the sampling time (t_{samp}) used for the calculation of the correlation functions is divided, and $t_j = (j-1)\Delta t$, with $j = 1, \ldots, N_t$.

Again, N is the total number of atoms in the system.
The correlation functions were evaluated within the same time frames Δt as those used for the propagation of AIMD runs. It should be noted that the brackets notation $\langle ... \rangle$ defines in Eq.2.38 an ensemble average over all AIMD trajectories.
Recalling the general properties of classical correlation functions described above, in particular that $|C_{vv}(0)| > |C_{vv}(t)|$, $\forall t > 0$, it is usually convenient to normalize the $C_{vv}(t)$ by taking $\langle \underline{v}(0) \cdot \underline{v}(t) \rangle / \langle \underline{v}(0) \cdot \underline{v}(0) \rangle$, so that the autocorrelation function starts from 1. However, this normalization procedure is not strictly required.

Any spectral response function in the frequency domain, starting from the Vibrational Density of States, is obtained by means of Fourier-transformed correlation functions. In practice, this is achieved by applying a discrete, Fast Fourier Transform (FFT) procedure to the calculated correlation function, which is defined by a finite amount of data points, equally spaced by Δt.

When applying FT-correlation functions to do spectral simulations from AIMD trajectories, one main disadvantage consists in the so-called "finite time propagation" [16]. Indeed, any correlation function although sampled for a sufficiently large time will eventually correspond to a limited amount of points. Besides, despite the initial decaying behaviour of the correlation function, the long-time limit, according to which the correlation among sampled points should go to zero, is hardly satisfied. Such non-ideal effects are common in practical calculations may introduce spurious peaks within the power spectrum obtained *via* FT. In particular, the truncation of a calculated correlation function at $t = t_{samp}$ will cause its Fourier-transformed signal to contain similar features as the one of a step function, such as a sinc function.
In order to account for this limited sampling time, a correlation function can be multiplied by a window function, before applying the FFT-method. The window function helps to minimize the aforementioned effects by introducing a strongly decaying term to zero. In this work, the Hann's window [58], $w(t)$, has been adopted to multiply and fix all correlation functions obtained from AIMD trajectories. It is defined as:

$$w(t) = cos^2 \left(\frac{\pi t}{2 t_{samp}} \right) \quad . \tag{2.39}$$

At this point, an *intermezzo* should be dedicated to the mathematical and physical features determining the lineshape of a vibrational spectrum as the ones presented in this work [16,41,57]. Let us first start with the fundamental parameters entering the Fourier transform and affecting the lineshape, namely the sampling time, within t_{samp}, which defines a calculated correlation function and the spacing between the correlation-function data points, *i.e.* the timestep Δt. Due to the intrinsic "*time vs frequency*" uncertainty of Fourier transformation (here generally represented by σ_t for time in fs and σ_ω for frequency in wavenumbers), $\sigma_t \cdot \sigma_\omega \geq \frac{1}{4\pi c}$, the sampling time determines the resolution of the vibrational peaks, $\Delta\omega$, so that the longer is t_{samp} the smaller is the frequency spacing. For instance, sampling for 1 or 2 ps we can resolve each peak within 15 - 30 cm^{-1}. On the other hand, the timestep controls the maximum frequency of the spectrum, ω_{max}.

A more physically motivated characteristic entering the spectral properties is *broadening*, which can be of two kinds: "homogeneous" or "inhomogeneous", and both are determing peak

lineshapes. *Homogeneous broadening* can be understood in terms of quantum mechanics by considering the finite lifetime of a certain (vibrational) excited state, whose decay will eventually cause a broadening around the natural peak frequency. In such circumstances, another closely related factor is the so-called "dephasing time", which likewise determines a line widening, and is due to dynamic perturbations of the excited state.
An analogous picture is explainable with classical mechanics if we think of the natural damping, Γ, of an oscillator: the dissipation caused by friction or other non-conservation of energy will introduce a time-dependent decrease of the oscillation amplitudes (in such case the oscillator's VVAF is proportional to $e^{-\Gamma t}$). The more effective is damping the broader will be the peak centered at the oscillatory frequency.
Since all oscillators are naturally affected by this first kind of effects, the resulting peaks widening is called *homogeneous broadening* and it always determines a *Lorentzian* lineshape [44] (as expressed in Eq.2.21).
The second kind of broadening is caused by locally different physical environments or fluctuations felt by each oscillator, hence the name *inhomogeneous*. For instance, in the swarm of trajectories launched to describe the phase space of our system at a given temperature, each individual oscillator (even if formally identical to all the others), like a vibrating O-H bond, is subject to variable interactions due to its chemical surroundings. By averaging over all trajectories, the spectral response of this ensemble of oscillators will be affected by such temporary fluctuations. In the case of an inhomogeneous broadening, the characteristic lineshape is a *Gaussian*.

When comparing spectroscopic observables obtained from classical correlation functions with their quantum analogues it is crucial to recall their symmetry properties [40, 41, 52]. In the frequency domain, a quantum correlation function for a system in thermal equilibrium must obey the so-called "detailed balance" condition: $\tilde{C}_{qm}(\omega) = e^{\frac{\hbar\omega}{k_B T}} \tilde{C}_{qm}(-\omega)$. The same condition shall be applied to formally quantum spectral responses, as $\chi^{(1)}_{ab}(\omega)$ and $\chi^{(2)}_{abc}(\omega)$. Quantum correction factors $Q(\omega)$ exist to account for this property and to properly modify spectral responses calculated from classical correlation functions, so that: $\tilde{C}_{qm}(\omega) = Q(\omega)\tilde{C}_{cl}(\omega)$. In this work we have adopted $Q(\omega) = \frac{\hbar\omega}{k_B T}/(1 - e^{-\frac{\hbar\omega}{k_B T}})$, known as "harmonic correction" [59].

2.4.2 IR and VSF from velocity-velocity correlation functions

The calculation of vibrational IR and SFG spectra is achievable by knowing the dipole moment vector and the polarizability tensor of each vibrational chromophore present in the system. However, when using molecular dynamics simulations based on periodic density functional theory, obtaining the values of $\underline{\mu}$ and $\underline{\underline{\alpha}}$ is not a simple task. Various strategies exist for calculating such electronic properties, for example through the so-called "Maximally Localized Wannier Functions" (MLWFs) [60]. Such functions localized in real space can be obtained from Bloch orbitals and they have the advantage of providing a physically meaningful description of the electronic structure. In fact, the new orbitals constructed from MLWFs can be used to calculate electrical dipole moments and polarizabilities of each atom.
Unfortunately, when applying such strategy in the context of already expensive time-dependent calculations, the required computational cost increases dramatically. Moreover, in order to obtain converged signals of correlation functions such as $\langle \underline{\mu}(0) \cdot \underline{\mu}(t) \rangle$ or $\langle \underline{\mu}(0) \cdot \underline{\underline{\alpha}}(t) \rangle$, the necessary propagation time of AIMD trajectories increases.

Nevertheless, other approaches have proved to be extremely useful for the purposes of this work, being focused on the simulation of the spectra of water / metal oxide interfacial systems. Indeed, in characterizing the IR or VSF spectrum of such systems it clearly emerges that the O-H stretching mode dominates in the high frequency region of the vibrational spectrum. In such conditions, Tatsuhiko Ohto and coworkers provided a particularly interesting alternative strategy [61] to simulate IR and VSF optical responses without the need to use orbital projection schemes as the MLWFs or else. In their work [61] the initial step is to calculate correlation functions as their time-derivatives, *i.e.* $\langle \dot{\underline{\mu}}(0) \cdot \dot{\underline{\mu}}(t) \rangle$ and $\langle \dot{\underline{\mu}}(0) \cdot \dot{\underline{\underline{\alpha}}}(t) \rangle$. Secondly, the vibrational response is fully projected on the O-H stretching coordinate, namely the dipole moment vector and the polarizability tensor are thought to depend solely on it [62]. Assuming a linear dependence on the stretching displacement vector, both $\underline{\mu}$ and $\underline{\underline{\alpha}}$ for the ith-OH oscillator can be approximately written as:

$$\underline{\mu}_i(t) \approx \underline{\mu}_i^0 + \left[\frac{\partial \underline{\mu}_i}{\partial r^{OH}} \right]_0 \underline{r}_i^{OH}(t) \tag{2.40}$$

$$\approx \underline{\mu}_i^0 + \mu_i' \underline{r}_i^{OH}(t) \tag{2.41}$$

$$\underline{\underline{\alpha}}_i(t) \approx \begin{pmatrix} \alpha_{xx}^0 + \left[\frac{\partial \alpha_{xx}}{\partial r^{OH}} \right]_0 |\underline{r}_i^{OH}(t)| & 0 & 0 \\ 0 & \alpha_{yy}^0 + \left[\frac{\partial \alpha_{yy}}{\partial r^{OH}} \right]_0 |\underline{r}_i^{OH}(t)| & 0 \\ 0 & 0 & \alpha_{zz}^0 + \left[\frac{\partial \alpha_{zz}}{\partial r^{OH}} \right]_0 |\underline{r}_i^{OH}(t)| \end{pmatrix} \tag{2.42}$$

Here, the term $\underline{\mu}^0$ and $\underline{\underline{\alpha}}^0$ indicates the permanent dipole and polarizability. In both Eqs.2.40-2.42 the O-H stretching mode is considered to be dominated by the variation of the intramolecular O-H bond distance, as justified by quantum-chemical calculations done for the H_2O molecule [50, 53, 61]. Therefore, both $\underline{\mu}$ and $\underline{\underline{\alpha}}$ are linearly projected along the distance vector, $\underline{r}^{OH}$. For the polarizability, its tensorial (or matrix) character is formally reproduced by the outer product of two $\underline{r}^{OH}$ vectors, yielding the dependence from the modulus $|\underline{r}^{OH}(t)|$ in the matrix elements of Eq.2.42. Moreover, off-diagonal elements of the bond polarizability have been found to be negligibly smaller than diagonal ones [50]. As firmly reported by the authors in Ref. [61], this formulation of $\underline{\underline{\alpha}}$ is crucial for the "surface sensitivity" of the following $\chi_{abc}^{(2)}$ expression.
One further approximation is to take the transition polarizability components $\frac{\partial \underline{\underline{\alpha}}}{\partial r^{OH}}$ as isotropic: $\alpha'_{\mathrm{OH}} = \frac{\partial \alpha_{xx}}{\partial r^{OH}} = \frac{\partial \alpha_{yy}}{\partial r^{OH}} = \frac{\partial \alpha_{zz}}{\partial r^{OH}}$. The same argument is used to calculate the O-H transition dipole moment, where the derivatives of each Cartesian component of the dipole vector are assumed to be the equal: $\mu'_{\mathrm{OH}} = \frac{\partial \mu_x}{\partial r^{OH}} = \frac{\partial \mu_y}{\partial r^{OH}} = \frac{\partial \mu_z}{\partial r^{OH}}$.

As reported in Ref. [61], under such approximations, the first- and second-order susceptibilities from Eqs.2.36-2.37 may be reformulated for an esemble of M O-H oscillators as:

$$\chi_{ab}^{(1)}(\omega) = \frac{Q(\omega)\ {\mu'_{\mathrm{OH}}}^2}{i\omega^2} \int_0^\infty \sum_{i,j}^{M} \langle v_{b,j}^{\mathrm{OH}}(0)\ v_{a,i}^{\mathrm{OH}}(t) \rangle\ e^{-i\omega t}\ dt \tag{2.43}$$

$$\chi_{abc}^{(2)}(\omega) = \frac{Q(\omega)\ \mu'_{\mathrm{OH}} \alpha'_{\mathrm{OH}}}{i\omega^2} \int_0^\infty \sum_{i,j}^{M} \left\langle v_{c,i}^{\mathrm{OH}}(0)\ \frac{\underline{v}_j^{\mathrm{OH}}(t)\ \underline{r}_j^{\mathrm{OH}}(t)}{|\underline{r}_j^{\mathrm{OH}}(t)|} \right\rangle\ e^{-i\omega t}\ dt \tag{2.44}$$

for $a = b$, $\chi^{(2)}_{ab} = 0$ otherwise. Here, bond-projected velocities enter the formulation of both $\underline{\underline{\chi}}^{(1)}$ and $\underline{\underline{\underline{\chi}}}^{(2)}$. The harmonic quantum correction factor $Q(\omega)$ is already included in the formulation.

The new expressions in Eqs.2.43-2.44 provide a direct methodology to calculate IR and VSF optical responses of OH bonds within the typical stretching region, namely between 3000 and 4000 cm^{-1}, without the necessity to perform expensive "on the fly" orbital projection schemes. Moreover, for the $\underline{\underline{\underline{\chi}}}^{(2)}$ response, another fundamental property typical of VSF spectroscopy is satisfied: the surface specificity, thanks to the *ad hoc* expression of the polarizability tensor in Eq.2.44. Eventually, this new approach is essentially based on properly formulated velocity-velocity autocorrelation functions, even "surface specific", and it allows to evaluate directly the IR and VSF responses at the computational cost of standard AIMD trajectories, since only the OH-bond distances and velocities are required.

In the derivation above, the transition dipole moment and polarizability have been taken as frequency-independent, in line with the "Condon approximation". An important clarification is here necessary: the standard definition of Condon approximation usually arises from the context of molecular vibronic spectroscopy, where the electronic transition dipole moment is supposed to be independent from nuclear coordinates. In this work we are referring to vibrational transitions, where the involved dipole moment and polarizability are supposed to be uninfluenced from the local solvation environment. However, several studies have shown that the O-H stretching frequency in an aqueous medium can largely change due to orientational dynamics and to fluctuations in their electrostatic surroundings [50,63]. These effects have a consequence also on the strength of the vibrational transition probed spectroscopically, influencing the amplitude of the transition dipole or polarizability. In order to describe a more general spectroscopic response, the aforementioned methodology adopts a frequency-dependent parametrization of both μ' and α' done by James Skinner and coworkers [64, 65], which is based on quantum chemistry and classical molecular dynamics simulations and is specific for O-H(D) bonds:

$$\mu'_{\text{OH}}(\omega) = \left[A_\mu + \frac{B_\mu(C-\omega)}{D} \right] \mu'_{\text{OH},g} \tag{2.45}$$

$$\alpha'_{\text{OH}}(\omega) = \left[A_\alpha + \frac{B_\alpha(C-\omega)}{D} \right] \alpha'_{\text{OH},g} \quad . \tag{2.46}$$

Here, $A_\mu = 1.377$, $A_\alpha = 1.271$, $B_\mu = 53.03$ and $B_\alpha = 6.287$ are numerical parameters identical for OH or OD species. The hydrogen specific constants are $C = 3737$ cm^{-1} and $D = 6932.2$ cm^{-1} (for the deuterated bond, $C = 2745.8$ and $D = 4870.3$, also in cm^{-1}). $\mu'_{\text{OH},g}$ and $\alpha'_{\text{OH},g}$ are gas phase values (no environment), and ω is in wavenumbers. The frequency-dependent parametrizations are sketched in Fig.2.2.

Eventually, the vibrational IR and Sum Frequency Generation responses can be calculated for an ensemble of O-H oscillators as:

$$\chi^{(1)}_{ab}(\omega) = \frac{Q(\omega)\ {\mu'_{\text{OH}}}^2(\omega)}{i\omega^2} \int_0^\infty \sum_{i,j}^{M} \langle v^{\text{OH}}_{b,j}(0)\ v^{\text{OH}}_{a,i}(t) \rangle\ e^{-i\omega t}\ dt \tag{2.47}$$

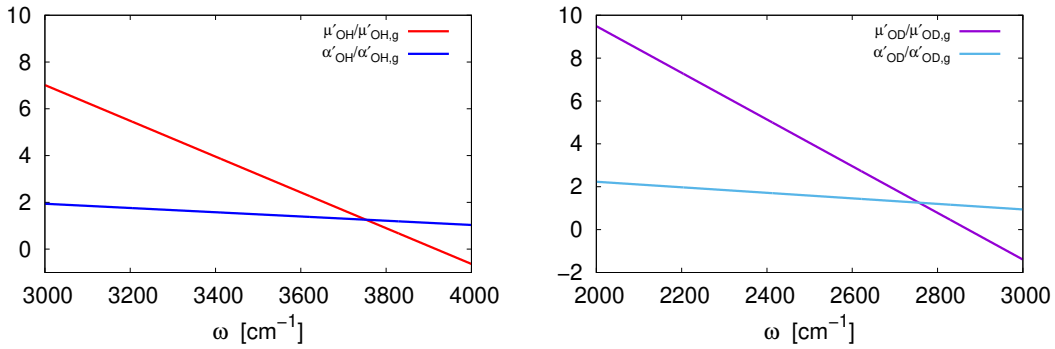

Figure 2.2: Plots of Skinner's parametrizations [64, 65] of transition dipole and transition polarizability for O-H(D) bonds within the typical frequency ranges of O-H and O-D stretching modes, respectively. Please note that on the y-axis the dimensionless ratio between μ (or α) and its gas-phase reference value is reported.

$$\chi^{(2)}_{abc}(\omega) = \frac{Q(\omega)\ \mu'_{\mathrm{OH}}(\omega)\alpha'_{\mathrm{OH}}(\omega)}{i\omega^2} \int_0^\infty \sum_{i,j}^{M} \left\langle v^{\mathrm{OH}}_{c,i}(0)\ \frac{\underline{v}^{\mathrm{OH}}_j(t)\ \underline{r}^{\mathrm{OH}}_j(t)}{|\underline{r}^{\mathrm{OH}}_j(t)|} \right\rangle\ e^{-i\omega t}\ dt \quad , \tag{2.48}$$

where the calculated susceptibilities are relatable to the respective IR and VSF spectroscopic intensities. For instance, considering a p-polarized infrared spectrum, this can be approximated to the z-oriented vibrational response, so that we have: $I^{IR}_{zz} \propto Re\{\chi^{(1)}_{zz}(\omega)\}$. In the case of a ssp-polarized VSF experiment, the response can be related to the sole xxz-susceptibility element *via*: $I^{VSF}_{xxz} \propto |\chi^{(2)}_{xxz}(\omega)|^2$. The method presented here from Ohto *et al* is in principle transferable to other aqueous systems, including water / metal oxides interfaces [66].

3 Computational details: the VASP program

In so far as quantum mechanics is correct, chemical questions are problems in applied mathematics.

Henry Eyring

As introduced above, the main *corpus* of this work in terms of electronic structure theory has been done at the periodic Density Functional Theory (DFT) level. Among the several computer packages available for simulating solids and surfaces, the "Vienna Ab initio Simulation Package" (VASP) [67–72] has been the favourite one to adopt. VASP's capabilities cover vast features of DFT calculations, ranging from LDA to hybrid functionals. It has become recently possible to extend the limits of DFT by the introduction of wave-function based techniques, like the "Random Phase Approximation" (RPA) and "2^{nd}-order Møller-Plesset perturbation theory" (MP2) which allow for more accurate, although more expensive, calculations. Other, more sophisticated approaches for static electronic structure calculations are also available, such as Green's function-based (GW) methods for many-body perturbation theory or even Coupled-Cluster (CC) [73]. At the heart of a static VASP calculation employed in this work there is the projector-augmented wave (PAW) method [74], originally introduced by P. E. Blöchl [29], for the treatment of electron-ion interactions. Since VASP employs three-dimentional periodic boundary conditions, all calculations are based on unit-cell or supercell settings consistent with the crystal structure of the considered material.

For the calculation of the band structure of a given material with DFT it is necessary to consider an expansion of the wavefunction in terms of $\underline{k}$-values, where for $\underline{k} = 0$ we are at the Γ-point. Moreover, the number of $\underline{k}$-points necessary for a calculation depends critically on the necessary precision and on the fact whether the system is metallic. Metallic systems require an order of magnitude more $\underline{k}$-points than semiconductors and insulators. It should also be noted that the crystal symmetry properties of the considered unit cells affect the calculation. In fact, while to sample the full Brillouin zone (BZ) a large amount of $\underline{k}$-points is needed, symmetry reduces this number thanks to the so-called "irreducible parts" of the Brillouin zone, where fewer $\underline{k}$-points can be considered. In the VASP program, a particular method for sampling of the Brillouin zone is implemented, known as "Monkhorst-Pack" $\underline{k}$-points mesh, which has also been constantly employed for the calculations in this work.

In the work presented here the VASP program has been employed not only to obtain the ground-state properties of considered materials, but also to evaluate the respective minima in the potential energy surfaces using Geometry Optimization (GO), to calculate "static" vibrational frequencies *via* Normal Mode Analysis (NMA), and to propagate classical nuclear trajectories with *Ab Initio* Molecular Dynamics (AIMD). For GO calculations, VASP allows to employ two main algorithms: a quasi Newton-Raphson method called "RMM-DIIS" and developed by Péter Pulay [75] and a conjugate-gradient procedure. In the first case a quasi-Newton (variable metric) algorithm is used to relax the ions into their instantaneous ground state. The

forces and the stress tensor are used to determine the search directions to find the equilibrium positions (the total energy is not taken into account). This algorithm is very fast and efficient if the structure we are calculating is close to local minima, but fails badly if the initial positions are a bad guess, while the conjugate-gradient method is more suitable for structural search in zone of the phase space at higher energy.
For NMA, which is usually performed at an already minimized geometry and only at the Γ-point, the numerical evaluation of second-derivatives of total energy is performed and the following diagonalization of the Hessian matrix is done to produce vibrational eigenvectors with corresponding frequencies. To calculate the Hessian matrix, finite differences are used, *i.e.* each atom is displaced in the direction of each Cartesian coordinate, and from the forces the Hessian matrix is determined. In the NMA calculations performed for this work, the atoms are displaced in all three Cartesian directions, resulting in a significant computational effort even for moderately sized high-symmetry systems, but allowing for selective displacement of certain atoms while keeping fixed the others.
For AIMD trajectories, it is possible to perform simulations within the microcanonical (NVE), canonical (NVT) and even isothermal–isobaric (NPT) ensembles. For the purposes of this work, only microcanonical and canonical trajectories have been calculated, the latter using the Nosé-Hoover thermostat to mantain constant temperature. For all GO, NMA and AIMD, forces are calculated for each α-atom based on the Hellmann-Feynman theorem: $-\underline{\nabla}_\alpha \langle\psi_0|\hat{H}_e|\psi_0\rangle \approx -\langle\psi_0|\underline{\nabla}_\alpha \hat{H}_e|\psi_0\rangle$.

All electronic structure calculations in this work, from geometry optimization to AIMD trajectories, have been performed using the Kohn-Sham [17] DFT (KS-DFT), at the GGA level of theory, employing the Perdew-Burke-Ernzerhof (PBE) [21, 22] exchange-correlation functional and a projector-augmented plane-wave basis (PAW) [29] as implemented in the Vienna Ab initio Simulation Package (VASP) [67, 68, 74]. Van der Waals interactions were included by Grimme's empirical D2 method [32]. For all calculations, we based our structural modelling on a α-$Al_2O_3(0001)$ surface slab model using on a hexagonal 2×2 unit-cell. A $3 \times 3 \times 1$ Monkhorst-Pack $\underline{k}$-mesh [76], corresponding to five $\underline{k}$-points in the irreducible BZ, and a kinetic energy cutoff of 400 eV were used.
When calculating vibrational frequencies and normal modes at the DFT / PBE+D2 level, we always employed a finite difference step of $1.5 \cdot 10^{-2}$ Å and an SCF-convergence threshold of 10^{-5} eV. We performed AIMD simulations within the canonical ensemble (NVT) at 300 K using the Nosé-Hoover thermostat [36–38]. Classical nuclear trajectories were propagated starting from optimized PBE+D2 structures, while initial velocities were generated randomly according to a Boltzmann distribution at $T = 300$ K. The equations of motion for nuclear degrees of freedom were propagated according to the Velocity-Verlet algorithm with timestep of $\Delta t = 0.2$ fs.

In some examples, reaction path profiles between two structures have also been studied in order to search for transition states (TS), namely saddle points in the potential energy surfaces. To investigate such reaction paths, the so-called "Nudged Elastic Band" method has been employed, specifically in its "Climbing Image" (CI-NEB) version. The NEB is a method for finding saddle points and minimum energy paths between known reactants and products. The method works by optimizing a number of intermediate structures (known as "images") along the reaction path, or "band". Each image should have the lowest energy possible while maintaining equal spacing to neighboring images. This is achieved by a constrained optimization, where additional spring forces are introduced along the band between images and also by projecting

out the component of the force due to the potential perpendicular to the band. In the CI-NEB version, the image with highest energy is driven up to the saddle point. This image does not feel the spring forces along the band. Instead, the true force at this image along the tangent is inverted. In this way, the image tries to maximize its energy along the band, and minimize it in all other directions. When this image converges, it will be at the exact saddle point.
The VASP program allows for this kind of analysis thanks to the VTST package, implemented by H. Jónsson and G. Henkelman [77, 78].

4 Vibrational Spectra of Adsorbed Water on the Al-terminated α-Al_2O_3(0001) Surface [1]

When theory and experiment agree, that is the time to be especially suspicious.

Niels Bohr

4.1 Water reactivity towards α-alumina: State of the art

Water adsorption onto metal oxides such as α-Al_2O_3 has been object of various studies, from both theory and experiment. In particular, single-crystal oxides have been shown to be reactive for H_2O dissociation also when considering non-defective, perfect surfaces, as pointed out in seminal reviews [79–82]. It was previously thought that water may be reactive only towards surface defect sites, as reported in Ref. [83]. In fact, a representative example of water dissociation and adsorption onto a clean oxide is given by the α-Al_2O_3(0001) surface.

Largely investigated [84–90], this surface is only one of the possible crystal cuts of corundum [11, 91–93], yet it is the most stable and common one. The clean α-alumina (0001) surface is composed by alternating (single and double) layers of O- and Al-atoms, but the absolute surface morphology has been under debate. In particular, is has been argued that an unequivocal determination of the exact surface structure is strongly affected by the method employed to prepare a single-crystal sample and also by the experimental techniques used for structural characterization. More specifically, low-energy electron diffraction (LEED) patterns [94–96] and X-ray diffraction measurements [97] are consistent with a "half-metal terminated surface", as reported by Woodruff [93], with uppermost Al^{3+} ions that act like Coordinatively Unsaturated Sites (CUS). These observations are also sustained by many theoretical and computational works [11, 91, 98–100], which also point in the same direction. Among them, a systematic study of α-Al_2O_3 electronic structure and energetics, considering various surface terminations, was done by Kurita *et al.* [11]. As we reported previously in the Preamble, in this work we relied on the theoretical DFT characterization done by Kurita and coworkers to build up our structural models. In particular, we considered their so-called "Al-I" stoichiometric model, being the most stable structure for the (0001) surface in a water and oxygen free environment (UHV conditions), to construct slab models for the Al-terminated (0001) surface, and as starting point for later water-covered structures.

Concerning now the adsorption of water on α-alumina, several studies have been focused to describe phase diagrams and relative stability of structures representing the H_2O / α-Al_2O_3 interface. From the experimental point of view, first high-resolution electron-energy-loss spectroscopy (HREELS) studies [101–103] showed vibrational resonances compatible with the presence of dissociated water on the (0001) surface. Then, early LEED and temperature-programmed desorption (TPD) studies [94, 95] reported that the UHV-stable Al-terminated

surface would get reconstructed upon increasing water pressure. Parallely, X-ray photoemission (XPS) experiments [104,105] as well as X-ray reflectivity (XR) by J. Catalano [106], indicated a surface reconstruction once the Al-terminated (0001) surface is exposed to water. These studies suggest the emergence of an O-terminated surface in moist conditions, with at least one layer of undissociated water on top of it. Such description of alumina in aqueous environments is also supported by Atomic Force Microscopy (AFM) measurements [107,108]. However, the prementioned techniques have clear limitations, either because of low resolution or because of difficulty in resolving the interfacial hydrogen-bonding structure which would arise from the high water loading.
Among the various experimental methods of surface science, vibrational spectroscopy is capable of capturing local structural features and to distinguish between physisorbed, chemisorbed and dissociated water on the oxide surface. In fact, since the developments of surface-sensitive techniques as Vibrational Sum Frequency (VSF) generation, an increasing number of spectroscopic investigations have been provided on this system. The VSF experiments [8, 109–113] reported in literature are also indicating that the Al-terminated surface gives way to an O-terminated, or hydroxylated surface with interfacial OH bonds resulting from water adsorption. It should be mentioned that recent study by Petrik *et al.* [114] employed vibrational analysis techniques (infrared reflection absorption spectroscopy, IRAS, and diffuse reflectance infrared Fourier transform spectroscopy, DRIFTS) together with TPD to investigate the adsorption of water on α-Al_2O_3(0001) and α-alumina particles. Their conclusion confirms the formation of topmost hydroxyl groups, although the full surface hydroxylation could not be observed.

Before going into the details of local adsorption structures at various water coverages, let us briefly review the literature associated with theoretical works dedicated to study the H_2O / α-Al_2O_3(0001) interface. In these works [9,10,98–100,108,112,113,115–125], *ab initio* calculations have been performed using various approaches, from molecular cluster models to embedded periodic ones and to periodic slab calculations, and with different levels of electronic structure, from DFT to Hartree Fock (HF) or wave-function-based methods. Overall, the resulting picture that can be learnt from these computational works is that water can favourably adsorb onto the (0001) surface either molecularly or dissociatively. Both reactions are thermodynamically favoured, although no absolute agreement on the energetics and kinetics of adsorption have been reached. Upon further water coverage, the occurrence of a hydroxylated surface is mostly sustained, where the terminating OH groups become then the interacting units for further water adsorption *via* formation of an interfacial hydrogen bonding network.

Despite the vast scientific production just cited, many unsolved questions remain about the atomistic description of H_2O adsorption reactions on α-alumina, whose mechanism is at the very basis of this oxide' surface physical chemistry. When crossing to the realm of solid / liquid interfaces the agreement on such well-studied system is not at all improved, for instance when considering the characteristics of water layer(s) in contact with the surface. Understanding the properties of interfacial OH groups in environmental conditions is indeed crucial to determine the "acid - base" chemistry of aluminum oxide, with important electrochemical implications.
It is therefore in this not fully clarified context that our research group has undertaken the study of H_2O on α-Al_2O_3 from a theoretical perspective, in a joint effort with experts in surface vibrational spectroscopy (R. Kramer Campen group, FHI, Berlin). The research group where this work was conducted has considered also less studied surface terminations like the O-terminated $(1\bar{1}02)$ [126] and the $(11\bar{2}0)$ [127], while the (0001) surface has been looked from different point of views [2, 12, 128–130], starting from the unimolecular water adsorption reaction, up to more

complex structures resembling environmental conditions, as we shall see in details in what follows.

4.2 Dissociative water adsorption on the α-Al_2O_3(0001) surface: A DFT and AIMD investigation

Let us now focus on the first representative example of this doctoral project. In this section water unimolecular adsorption onto the Al-terminated (0001) surface will be described, starting with the fundamental aspects of this process and then focusing on the dynamical properties of (dissociatively) adsorbed H_2O and on the calculation of vibrational frequencies and spectra in comparison with experiments. In fact, already twenty years ago, in the seminal work of Hass *et al.* [9,10], computer simulations employing Car-Parrinello molecular dynamics (CPMD) had extended other studies to include finite temperature effects and to provide a first, direct insight in the reaction dynamics. In these works, H_2O could interact with α-alumina either *via* molecular or dissociative adsorption, the latter involving the molecule to split into two fragments and forming two surface hydroxyl groups. For the dissociative path, two possible products had been observed with CPMD, named "1-2" and "1-4" states. Later on, Ranea and coworkers provided further investigations [119,120], where they highlighted the possibility of one more dissociated state, analogous to the "1-4" structure but where the two formed OH bonds were more distant.

Looking at the research conducted in our group, Wirth *et al.* [128] focused on detailed energetics and kinetics of water (molecular and dissociative) adsorption products using periodic DFT calculations and also at the occurrence of nuclear quantum effects which could be present due to the intrinsic quantum-mechanical nature of hydrogen. In Ref. [128] the authors first considered submonolayer coverages (one water per 2×2 unit cell, *i.e.*, coverage 1/4). Here a water molecule was found to coordinate with O-down to an unstaurated CUS Al atom, while in dissociative cases a water molecule splits into OH (or OH^-) sitting on a Al CUS site, and H (or H^+) attaching either to the nearest ("1-2 dissociation") or a next-nearest neighbour surface O atom ("1-4 dissociation"), or to an O atom even further away ("1-4' dissociation"). In Refs. [12,128,129] it was argued that a molecular adsorbate is metastable with respect to dissociation into 1-2 (the most stable) and 1-4 species (of about the same stability as the molecular species). By hydrogen diffusion, out of 1-4 also the form 1-4' (slightly less stable than 1-4) could be formed. In those references [12,128,129], the 1-2 and 1-4 species, which had been only postulated in Refs. [9,10], were investigated and finally observed experimentally, together with 1-4' species. In the experiment [12], deuterated water (D_2O) had been dosed on the α-alumina (0001) surface with a molecular beam source (MBS), leading to a low-coverage situtation, and the reaction products were spectroscopically identified by VSF. VSF signals corresponded to six distinct OD stretch vibrations: three for the "surface OD" bonds of 1-2, 1-4, and 1-4', and three for the "adsorbate OD" bonds of them. Here, "surface OD" refers to the vibration of the D(+)-surface O vibration, while "adsorbate OD" to the vibration of the dissociated OD(-) fragment of water, on the Al CUS site. The modes, which will be reiterated below, were assigned based on vibrational frequencies obtained by Normal Mode Analysis (NMA) using DFT, *i.e.*, on the harmonic approximation.
While NMA yielded relative frequencies in reasonable agreement with experiment, in this work we go beyond the previous, static, theoretical treatment both to assess the importance of these additional effects and to calculate intensities and linewidths. In particular, using Born-

Oppenheimer Ab Initio Molecular Dynamics (AIMD) we shall account for molecular motion, anharmonicity and mode couplings at finite temperature, and we will determine VSF intensities using a correlation function approach. This serves to get insight into the mentioned, so far neglected effects and to critically assess the mode assignment done in Ref. [12].

The energetics and thermodynamic details of water dissociative adsorption on Al-terminated (0001) surface has been deeply investigated in our group by Dr. Jonas Wirth and Dr. Sophia Heiden, the latter focusing on a comparative analysis of adsorption energies, reaction barriers and static vibrational frequencies by means of various DFT methods. Specifically, in Ref. [130], the authors reviewed the stability of different adsorption states (molecular *vs.* 1-2 *vs.* 1-4 *vs.* 1-4') using plane-wave basis methods and Generalized-Gradient Approximation (GGA) functionals, together with atom-centered basis approaches which allowed for DFT calculations using hybrid functionals (B3LYP) at a reasonable computational cost. Moreover, the use of localized atomic bases enabled Heiden and coworkers to employ wave-function based methods like Hartree Fock (HF) and localized- 2^{nd}-order Møller-Plesset perturbation theory (LMP2). Heiden *et al.* [130] found that DFT using hybrid functionals and LMP2 yield better (*i.e.* higher) reaction barriers for hydrogen diffusion between 1-4 and 1-2 dissociated states, while GGA functionals lead to grossly underestimated activation energies. However, the greatest advantage of wave-function methods lies in its intrinsic hierarchy of approximations, which can be developed to provide more accurate theoretical results.

Since in this project the main focus has been on the dynamical aspects of adsorbed water on α-Al_2O_3, only one electronic structure approach has been employed, namely Kohn-Sham [17] DFT (KS-DFT), at the GGA level of theory, employing the PBE functional [21,22] and a PAW basis [29] as implemented in the VASP code [67, 68, 74]. Further technical information have been reported above in Chapter 3.
In this part of the work, DFT-based calculations and AIMD simulations are employed to describe the finite-temperature behaviour of adsorbed water on the Al-terminated α-alumina (0001) surface. In particular, the main focus is on the simulation of vibrational spectra beyond static NMA and the harmonic approximation employing the time-correlation functions methods described in previous sections, beginning with Vibrational Densities of States (VDOS). Specifically, the method developed by Ohto and coworkers [61] allows for direct assessment of anharmonic vibrational (IR and VSF) spectra for deuterated water OD fragments.

4.3 Computational models: Their realization and relative stability

In order to describe low-coverage water adsorption on the Al-terminated (0001) surface, the Al-I surface model [11], same as in Refs. [12, 128–130], comprising a 9-atomic layer (2×2) supercell (layer sequence Al_4-O_{12}-Al_4-Al_4-O_{12}-Al_4-Al_4-O_{12}-Al_4) with dimensions 9.66 Å ×9.66 Å × 31.41 Å (20 Å of vacuum in the z-direction), and employing 3D periodic boundary conditions has been used. For geometry optimizations, NMA and AIMD the lowest four layers (Al_4-O_{12}-Al_4-Al_4) are kept fixed at bulk values optimized in Ref. [12], while the upper five layers (O_{12}-Al_4-Al_4-O_{12}-Al_4) are allowed to be relaxed, or to move. On top of this relaxed surface, which exhibits four Al CUS sites and it is shown in Fig.4.1, water molecules are adsorbed and corresponding structures have been optimized.

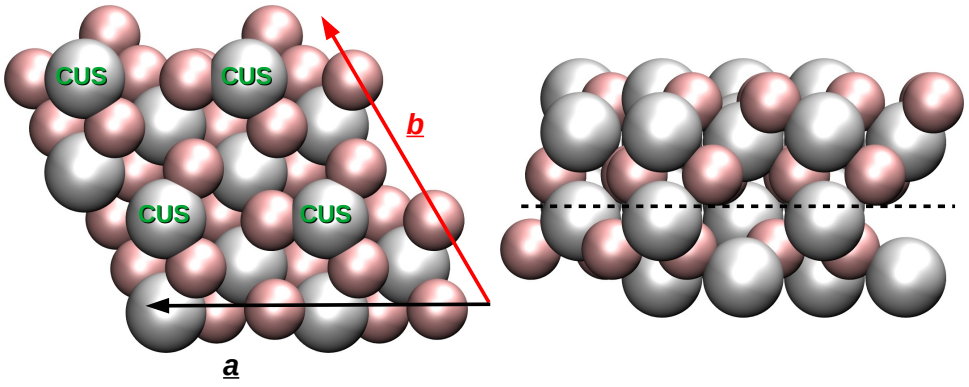

Figure 4.1: Top (a) and side (b) views of Al-terminated α-$Al_2O_3(0001)$ (2×2) surface coincident with model Al-I from Kurita *et al.* [11]. The surface slab is composed by alternating (single and double) layers of O- and Al-atoms, as also used in Refs. [12, 128–130]. Surface atoms are shown as "van-der-Waals spheres" in pale colors (Al in grey and O in red). Atoms below the dashed lines in (b) belong to the lowest four layers which are kept fixed at bulk values.

Two coverages were considered. In a first model, we have one water molecule per (2×2) cell, *i.e.*, coverage 1/4. This coverage is "low" but presumably still higher than in experiment. For the 1/4 coverage case, the corresponding, most stable dissociated species are those of Refs. [12, 129, 130], *i.e.*, the 1-2, 1-4, and 1-4' configurations. Fig.4.2 provides an overview of molecularly and dissociatively adsorbed structures at 1/4 coverage, including the intact water. All products are accompanied by adsorption energies for dissociated and the molecular species obtained with PBE+D2, which have been calculated as:

$$E_{\text{ads}} = E(\text{adsorbate} + \text{surface}) - [E(\text{adsorbate}) + E(\text{surface})] \tag{4.1}$$

where E stands for the DFT total energy resulting from geometry optimizations.

For the same structures, Gibbs free energies of adsorption could also be calculated, where the individual Gibbs free energies at temperature T for each species were computed using the following relationship: $G(T) = H(T) - TS(T) \approx E + G_{vib}(T)$. We considered the vibrational contribution being the only relevant one besides the total DFT energy, since translation and rotation do not occur in the applied slab model and electronic contributions can be negleted even at high temperature thanks to the wide band gap of aluminum oxide (~ 4 eV). Of course, in the case of molecularly adsorbed D_2O, neglecting rotational and translational contributions may have an impact on the adsorption enthalpy and entropy. Nevertheless, here we have adopted the same approach for all adsorption geometries. The vibrational contribution to Gibbs free energy is obtained according to the equation [40, 128]:

$$G_{\text{vib}}(T) = \sum_i \left[\hbar\omega_i \left(\frac{1}{2} + \frac{1}{e^{\frac{\hbar\omega_i}{k_B T}} - 1} \right) - \frac{\hbar\omega_i}{e^{\frac{\hbar\omega_i}{k_B T}} - 1} + k_B T \cdot ln\left(1 - e^{-\frac{\hbar\omega_i}{k_B T}}\right) \right], \tag{4.2}$$

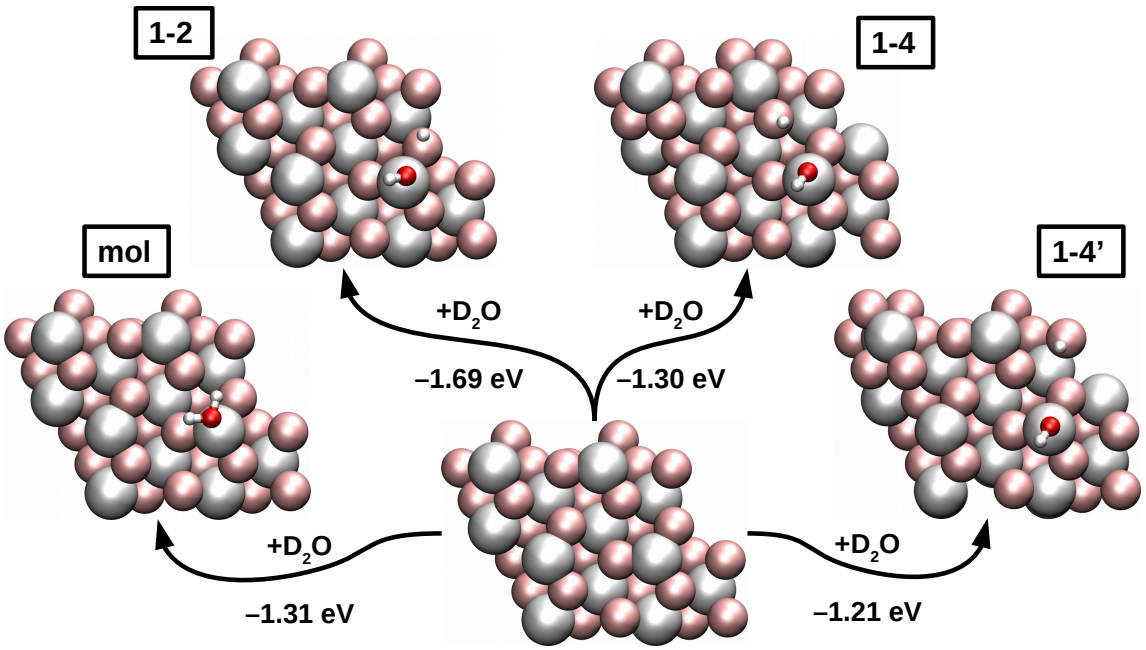

Figure 4.2: Top views of the molecularly and dissociatively adsorbed D_2O on Al-terminated α-$Al_2O_3(0001)$ (2×2) surface. Adsorption energies, E_{ads}, relative to the clean Al-terminated surface, calculated at the PBE+D2 level of theory, are also reported.

where k_B is Boltzmann constant and ω_i is the ith-vibrational mode obtained by NMA.
Using Gibbs free energies of adsorption, we could also calculate relative adsorption probabilities, $P_{ads}^{(j)}$, for each jth-dissociated structure under study. Such probability is obtained from the corresponding Boltzmann distribution function at 300 K:

$$P_{\text{ads}}^{(j)} = \frac{e^{-G_{\text{ads}}^{(j)}/k_B T}}{\sum_i e^{-G_{\text{ads}}^{(i)}/k_B T}} \quad . \tag{4.3}$$

Here, $G_{\text{ads}}^{(j)}$ is the relative Gibbs free energy of adsorption for species j. The calculated probabilities can provide additional information regarding the likelihood to find a given adsorbate at T = 300 K. Their application in our spectral simulation is commented below.

In Tab.4.1 we list adsorption energies and adsorption free energies $G_{\text{ads}} = H_{\text{ads}} - TS_{\text{ads}}$ at $T = 300$ K for all dissociated structures at coverage 1/4 and more. From the table, we can see that 1-2 is the most stable adsorption product, 1-4 and the molecular species less but about equally stable on this level of theory, and 1-4' is slightly less stable than all the previous ones, in agreement with previous observations [12, 128]. Also the comparison with other theoretical and experimental results [94, 95, 99] is quite satisfactory, especially given the wide energy range provided by thermal desorption experiments between 1.0 and 1.8 eV.

In fact, in order to study the effects of coverage, also the case with two molecules per (2×2) cell was considered, *i.e.*, coverage 1/2. Various combinations of dissociated and molecular adsorbed

Table 4.1: PBE+D2 adsorption energies and Gibbs free energies (at 300 K), including the respective Boltzmann probabilities P_{ads}, for adsorption of D_2O on α-Al_2O_3(0001), at two different coverages. The values of E_{ads} and G_{ads} for dimers were divided by two, so they are reported as adsorption energies per D_2O molecule. For dimers, adsorption probabilities are referred to dissociated products only. All energies are in eV.

	monomer			dimer		
species	E_{ads}	G_{ads}(T=300 K)	P_{ads}(T=300 K)	E_{ads}	G_{ads}(T=300 K)	P_{ads}(T=300 K)
molecular	-1.31	-1.18	$3 \cdot 10^{-7}$	–	–	–
1-2	-1.69	-1.57	~ 1	-1.68	-1.55	~ 1
1-4	-1.30	-1.18	$3 \cdot 10^{-7}$	-1.21	-1.10	$3 \cdot 10^{-8}$
1-4'	-1.21	-1.10	$1 \cdot 10^{-8}$	-1.33	-1.22	$3 \cdot 10^{-6}$

species and their adsorption sites are now conceivable. In Fig.4.3 we show PBE+D2 optimized structures obtained by simply doubling the optimized 1-2, 1-4 and 1-4' motifs of the monomer at a neighbouring Al CUS site, and reoptimizing. In this case, doubly-dissociated species are obtained which will be used later as starting geometries for AIMD. We emphasize, however, that these doubly-dissociated dimer species are not necessarily the lowest-energy structures. While looking at the effect of surface coverage is certainly of interest, a full configurational sampling of adsorption geometries was not the aim of this work. In fact, during AIMD (at $T = 300$ K) in some cases "mixed configurations" were formed with one dissociated and one molecular adsorbate (see below). This requires a proton / deuteron transfer to form an intact water molecule, out of a dissociated species. For the example of the dissociated "1-4 dimer" in Fig.4.3(e), the formation of such a mixed dimer was studied in Appendix A by computing a reaction path for hydrogen transfer using the Nudged Elastic Band method [77,78]. There it is shown that indeed, the mixed species is by about 0.4 eV (0.2 eV per molecule) more stable than the doubly-dissociated species, and that the activation energy for this process is very small (less than 0.05 eV), suggesting a fast reaction. In fact, also in AIMD simulations of molecular beam scattering events [129], the formation of mixed species was seen . From Tab.4.1 we note that the adsorption energies / free energies per water molecule of the dimers differ by about 0.1 eV the most from the monomers, indicating only weak interactions between the two water adsorbates in the dimer case for the starting configurations shown in Fig.4.3. Interestingly, however, now the 1-4' configuration appears to be more stable than 1-4, *i.e.*, the stability order between these two appears to be reversed.

4.4 Vibrational frequencies and spectra: Results and discussion

In order to characterize frequencies of adsorbed D_2O on the Al-terminated α-Al_2O_3(0001) surface, we performed geometry optimizations for selected supercell models, NMA and AIMD simulations. When calculating vibrational modes within NMA, no frequency rescaling was performed unless stated otherwise.

We performed AIMD simulations within the canonical ensemble (NVT) at 300 K using the Nosé-Hoover thermostat [36–38]. We started our AIMD trajectories from optimized PBE+D2 structures of dissociated species as shown in Fig.4.3. Initial velocities were generated randomly according to a Boltzmann distribution at $T = 300$ K. The equations of motion for nuclear degrees of freedom were propagated according to the Velocity-Verlet algorithm with timestep of

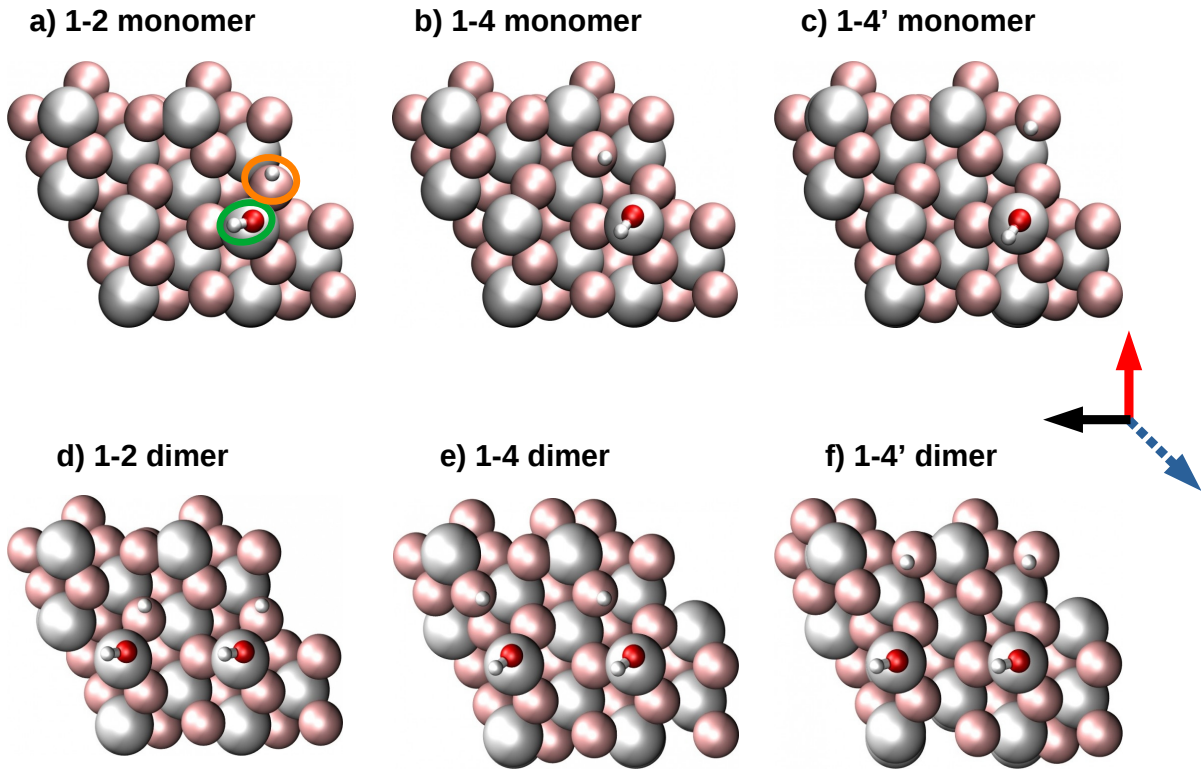

Figure 4.3: Top views of the dissociated D_2O species on Al-terminated α-$Al_2O_3(0001)$ (2×2) surface, used as starting geometries for AIMD. Dissociated species for coverage 1/4 (one water molecule per cell) are in the upper panels: (a) 1-2 monomer, (b) 1-4 monomer, (c) 1-4' monomer. The lower panels show specific dimer models, for coverage 1/2 (two water molecules per cell): (d) 1-2 dimer, (e) 1-4 dimer and (f) 1-4' dimer. All models consist of 9-layer surface supercells with additional water on top of the uppermost (Al) layer, with stoichiometric compositions of $Al_{24}O_{36}$ D_2O and $Al_{24}O_{36}(D_2O)_2$ for monomer and dimer cases, respectively. Optimized PBE+D2 structures are shown. In what follows, the water-hydroxyl groups are also denoted as "adsorbate OD" (circled in green), while OD groups consisting of a water-D plus a substrate O will be denoted as "surface OD" (circled in orange). For later reference, the Cartesian coordinate system used in this work is given by red (x-axis), black (y-axis) and blue (z-axis) arrows, the former in the surface plane, the latter perpendicular and pointing away from it.

$\Delta t = 0.2$ fs. We ran simulations for 50 ps in total. Technically, this was done by running five trajectories for each system, each of them being 10 ps long. Most of the propagation time was used for thermal equilibration, and only the last segment of each trajectory has been employed to sample the correlation functions in an interval $[0,t_{\mathrm{samp}}]$. Different sampling times t_{samp} have been tested. All the results shown below are for $t_{\mathrm{samp}} = 2$ ps, leading to a formal VDOS spectral

resolution of about 17 cm^{-1}.

The velocity-velocity autocorrelation function, whose Fourier transform gives the VDOS according to Eq.(2.38) was evaluated as in Ref. [57]. The correlation functions were evaluated at the same time steps t as those used for the AIMD. Other correlation functions needed in this work were evaluated accordingly. Finally, for Fourier transforms we multiply all (auto)correlation functions by Hann window functions, $w(t)$, as in Eq.2.39.

4.4.1 Vibrational frequencies from Normal Mode Analysis

As a first step towards the characterization of vibrational modes for different dissociated D_2O structures on Al-terminated α-alumina (0001), we report calculated frequencies by NMA using PBE+D2 treatment at the optimized geometries of Fig.4.3. Since our main source of comparison are VSF experiments from Ref. [12], we list only OD-stretching modes in Table 4.2. We also show experimental values and corresponding assignments [12], as well as differences $\Delta\tilde{\nu} = \tilde{\nu} - \tilde{\nu}(\mathrm{OD}^{1-2}_{\mathrm{surf}})$ relative to the lowest-energy OD vibration, $\mathrm{OD}^{1-2}_{\mathrm{surf}}$.

Table 4.2: Comparison between vibrational (stretching) wavenumbers $\tilde{\nu}$ at the DFT/PBE+D2 level of theory and experimental results from Ref. [12] for dissociated D_2O on Al-terminated α-Al_2O_3(0001). $\Delta\tilde{\nu} = \tilde{\nu} - \tilde{\nu}(\mathrm{OD}^{1-2}_{\mathrm{surf}})$ gives resonance positions, relative to the lowest-frequency vibration, $\mathrm{OD}^{1-2}_{\mathrm{surf}}$. All wavenumbers are in cm^{-1}. Subscripts "surf" and "ads" denote "surface OD" and "adsorbate OD" as specified in the text. The theoretical values are for NMA (normal mode analysis), AHO (anharmonic oscillator treatment), and VDOS (vibrational density of states), the latter obtained from AIMD at 300 K.

	experiment[1]		theory, monomer						theory, dimer		
			NMA		AHO[1]		VDOS		NMA	VDOS	
assignment	$\tilde{\nu}$	$\Delta\tilde{\nu}$	$\tilde{\nu}$	$\Delta\tilde{\nu}$	$\tilde{\nu}$	$\Delta\tilde{\nu}$	$\tilde{\nu}_{\max}$	$\Delta\tilde{\nu}$	$\tilde{\nu}$	$\tilde{\nu}_{\max}$	$\Delta\tilde{\nu}$
$\mathrm{OD}^{1-2}_{\mathrm{surf}}$	2729±5	0	2629	0	2523	0	2596	0	2628, 2629	2607	0
$\mathrm{OD}^{1-4}_{\mathrm{surf}}$	2764±5	35	2647	18	2541	18	2636	40	2618, 2624	–[2]	–
$\mathrm{OD}^{1-4'}_{\mathrm{surf}}$	2790±3	61	2687	58	2583	60	2649	53	2693, 2694	2682	75
$\mathrm{OD}^{1-4}_{\mathrm{ads}}$	2900±7	171	2789	160	2696	171	2781	185	2780, 2781	2778	171
$\mathrm{OD}^{1-4'}_{\mathrm{ads}}$	2900±7	171	2789	160	2697	174	2780	184	2787, 2787	2778	171
$\mathrm{OD}^{1-2}_{\mathrm{ads}}$	2910±7	181	2804	175	2713	190	2795	199	2792, 2793	2788	181

[1] From Ref. [12]; [2] broad VDOS in this region.

Our calculated NMA wavenumbers $\tilde{\nu}$ for coverage 1/4 reproduce the harmonic values reported in Ref. [12], obtained at the same level of theory (with slightly different computational settings). As noticed there, there is a consistent and systematic red-shift of about 100 cm^{-1} of the theoretical OD-stretches compared to experimental ones. If we include anharmonicity along the normal modes in a quantum mechanical fashion (but no mode coupling) as done in Ref. [12], we get the values "AHO" (anharmonic oscillator) shown in the table. These indicate that the red-shift from experiment becomes even larger. The anharmonic corrections have been obtained

by fitting of single-point total energy calculations where displacements along a given stretching mode were done [12]. The resulting potential was fitted to a single Morse oscillator, for which anharmonic corrections to $\tilde{\nu}_{01}$ vibrational transitions can be calculated analytically. In this approach, only diagonal contributions to harmonic energies have been considered. However, we note that spacings between resonances (measured by $\Delta\tilde{\nu}$) are quite similar between NMA/AHO theory and experiment, which was the basis for mode assignment in Ref. [12]. In particular, there are large frequency spacings between "adsorbed OD" and "surface OD" vibrations, with the latter being less energetic. Referring to the mismatch in absolute wavenumbers, we mention that a significant improvement of OD stretching frequencies is achieved if scaling factors are used. Using a scaling factor of 1.031 as recommended for PBE in Ref. [131], the harmonic frequencies for the "monomer" case become: 2710 (OD^{1-2}_{surf}), 2729 (OD^{1-4}_{surf}), 2770 ($OD^{1-4'}_{surf}$), 2875 (OD^{1-4}_{ads} and $OD^{1-4'}_{ads}$), and 2891 (OD^{1-2}_{ads}), respectively. This brings absolute measured and theoretical frequencies much closer together, up to $\sim$ 20-35 cm^{-1}.

We also learn from Tab.4.2, that at the higher coverages NMA frequencies don't change much, at least for the simple models shown in Fig. 4.3(d)-(f). Each mode splits into two (symmetric and antisymmetric), with only small splittings (in the order of 1 cm^{-1}) and hardly shifted w.r.t. the monomer cases – the "1-4 surf" case being an exception.

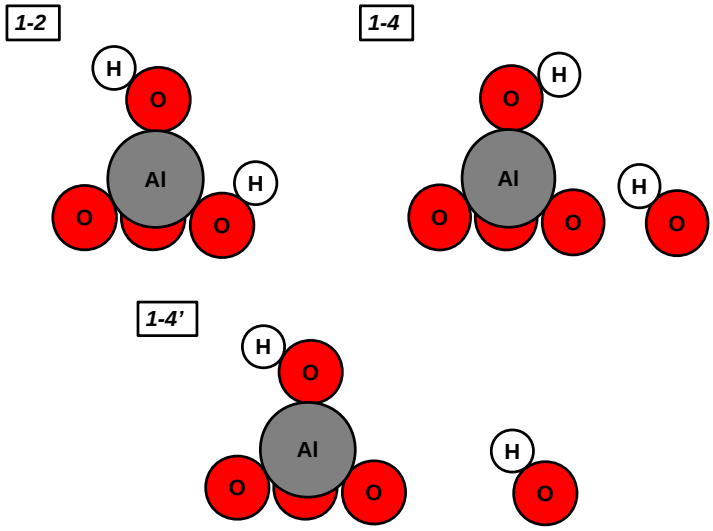

Figure 4.4: Schematic representation of OD fragments resulting from water (D_2O) dissociative adsorption on Al-terminated (0001) surface. The hydroxyls are shown taking into account their relative distances and their orientations. Such characteristics don't change substantially between monomeric and dimeric species.

In Fig.4.4 a schematic side view of different OD bonds related to the three dissociation products (1-2, 1-4 and 1-4') can be seen. As already mentioned, each adsorption state is characterized by an increasing distance between the OD fragments, but the relative orientation of OD_{ads} against OD_{surf} changes as well: in 1-2, the two bonds feel a considerable steric hindrance which forces them to orient in opposite directions, while in the 1-4 they seem to be able to adjust so that partial hydrogen bonding is possible. In the 1-4' situation, the greater distance allows each OD bond to be almost "free". Further intrinsic differences are retrievable among the

"surface" and "adsorbate" deuterated hydroxyls. In fact, they have oxygen atoms in different coordination geometries [121]. In the OD_{ads}, we have a so-called "μ_2-O" corresponding to a twofold coordinated oxygen, while in OD_{surf} we find a threefold coordinated atom, or μ_3-O, same as in other situations, namely the hydroxylated α-alumina(0001) surface.

The presence of vicinal bonds as in the dissociated water structures with so different OD stretching frequencies may lead the reader to consider possible dipolar interactions among adsorbates. Indeed, as investigated for other surfaces like CO on NaCl(100) [132], dipole-dipole interactions between adsorbed fragments can lead to frequency shifts of few wavenumbers because of vibrational excitonic Davydov splitting [133]. In order to sort out this possibility, NMA frequencies have been calculated for the 1-2 monomer considering different levels of deuteration: 1) OH_{ads} *vs.* OD_{surf} 2) OD_{ads} *vs.* OH_{surf} or 3) OH_{ads} *vs.* OH_{surf}. If vibrational Davydov splittings are present, we should expect deuterated and non-deuterated bonds to interact weakly, due to the wider energy spacing of their stretching modes, leading to "unperturbed" frequencies. In fact, the resulting vibrational analysis gives: for 1), $\tilde{\nu}(OH_{ads}) = 3855$ cm^{-1} and $\tilde{\nu}(OD_{surf}) = 2627$ cm^{-1}; for case 2) $\tilde{\nu}(OD_{ads}) = 2806$ cm^{-1} and $\tilde{\nu}(OH_{surf}) = 3616$ cm^{-1}; in case 3) we find $\tilde{\nu}(OH_{ads}) = 3855$ cm^{-1} and $\tilde{\nu}(OH_{surf}) = 3616$ cm^{-1}. As we could expect, the frequency shift with respect to the fully deuterated case shown in Tab.4.2 is at most of 2 cm^{-1}, indicating that vibrational excitonic interactions are totally negligible for this system.

4.4.2 Vibrational Density Of States (VDOS) from NVT/AIMD simulations

In order to go beyond static DFT, we now report the results on VDOS curves calculated from AIMD trajectories at constant temperature (300 K). In Fig.4.5, we show the VDOS for the three dissociated species in the "monomer" (coverage 1/4) and "dimer" (coverage 1/2) models when used as respective starting configurations in AIMD. In the upper panels of Fig.4.5, VDOS curves over a frequency range from 0 to 3000 cm^{-1} are shown, while the lower panels refer to the OD stretching region only, between 2500 and 3000 cm^{-1}.

It appears that the spectra for both triads of reaction products have two main bands. Up to 1000 cm^{-1} surface vibrations and OD bending modes are involved, while above 2500 cm^{-1} we see the signatures of stretching modes for different OD oscillators. For the "monomer" dissociated species, we have two maxima per model (1-2, 1-4 or 1-4'), *i.e.*, we retrieve all six modes reported in Tab.4.2. In the column "monomer, VDOS", we show the maxima of the VDOS curves as $\tilde{\nu}_{max}$. Compared to the NMA results, we notice frequency shifts to lower values for all modes: the OD_{ads} vibrations are red-shifted by between 8 cm^{-1} for OD_{ads}^{1-4} and 38 cm^{-1} for $OD_{surf}^{1-4'}$. In general, red-shifts are larger for "surface OD" than for "adsorbed" fragments. The red-shifts arise from anharmonicity of the potential (including an approximate treatment of mode coupling). Note that, due to the absence of vibrational energy quantization and zero-point energy, in classical dynamics only the low-energy portion of the potential is probed at 300 K, and therefore anharmonic corrections are underestimated w.r.t. to a quantum treatment (AHO) – for which a red-shift ~ 100 cm^{-1} was found above.

For the "dimer", coverage 1/2 dissociative D_2O adsorption structures (right panels in Fig.4.5), a rather similar behaviour compared to the unimolecular example is found. Again, VDOS peaks at high frequency are comparable to NMA frequencies, with a red-shift of OD stretches by $\sim$

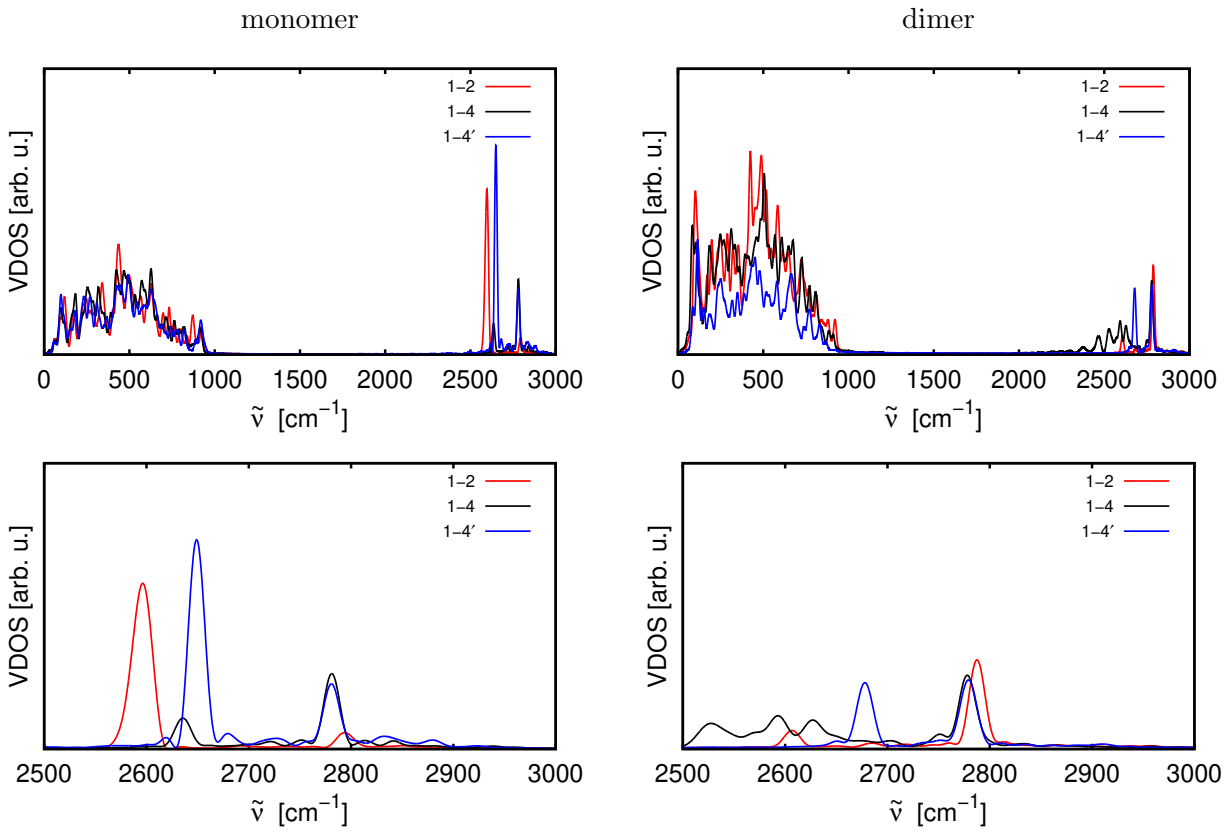

Figure 4.5: VDOS curves obtained by AIMD at 300 K, using the dissociated species 1-2, 1-4 and 1-4' for "monomers" (left) and "dimers" (right) of Fig.4.3 as starting configurations. Upper panels show the frequency range [0,3000] cm^{-1}, lower panels the OD stretching region [2500,3000] cm^{-1}. In the right panels, the VDOS scale is half that of the scale in the left panels.

10 cm^{-1} for OD_{ads} and by $\sim$ 20 cm^{-1} (at most) for OD_{surf} bonds. The frequencies for maxima in the VDOS are also shown in Tab.4.2. No value has been given for OD^{1-4}_{surf}, however, because around 2600 cm^{-1} a broad distribution of frequencies with several, comparably intense maxima is found. This has to do with a peculiar effect, not observed for other structures: in two of the five trajectories we propagated for the 1-4 dimer, a deuterium atom moved from a "surface" configuration to an "OD adsorbate" unit, forming a molecularly adsorbed D_2O species. In fact, as mentioned in Section 5.2 and in Appendix A, we find a mixed structure with one molecular and one dissociated water molecule being more stable, at least for 1-4. As a consequence, also molecular species show up in the VDOS. In Ref. [12], a normal mode analysis for a single D_2O molecule on a (2×2) cell of α-$Al_2O_3(0001)$, gave symmetric and antisymmetric D_2O stretch vibrations of 2550 and 2664 cm^{-1}, respectively, *i.e.*, below and above the OD^{1-4}_{surf} vibrational frequency of 2647 cm^{-1} (*cf.* Tab.4.2).

In addition to the VDOS curves shown so far, we report further spectral responses for both monomeric and dimeric species, where different velocity-velocity autocorrelation functions have been calculated including also atomic cross-correlation terms [134], namely: $\sum_{i,j}^{N} \langle \underline{v}_i(0) \cdot \underline{v}_j(t) \rangle =$

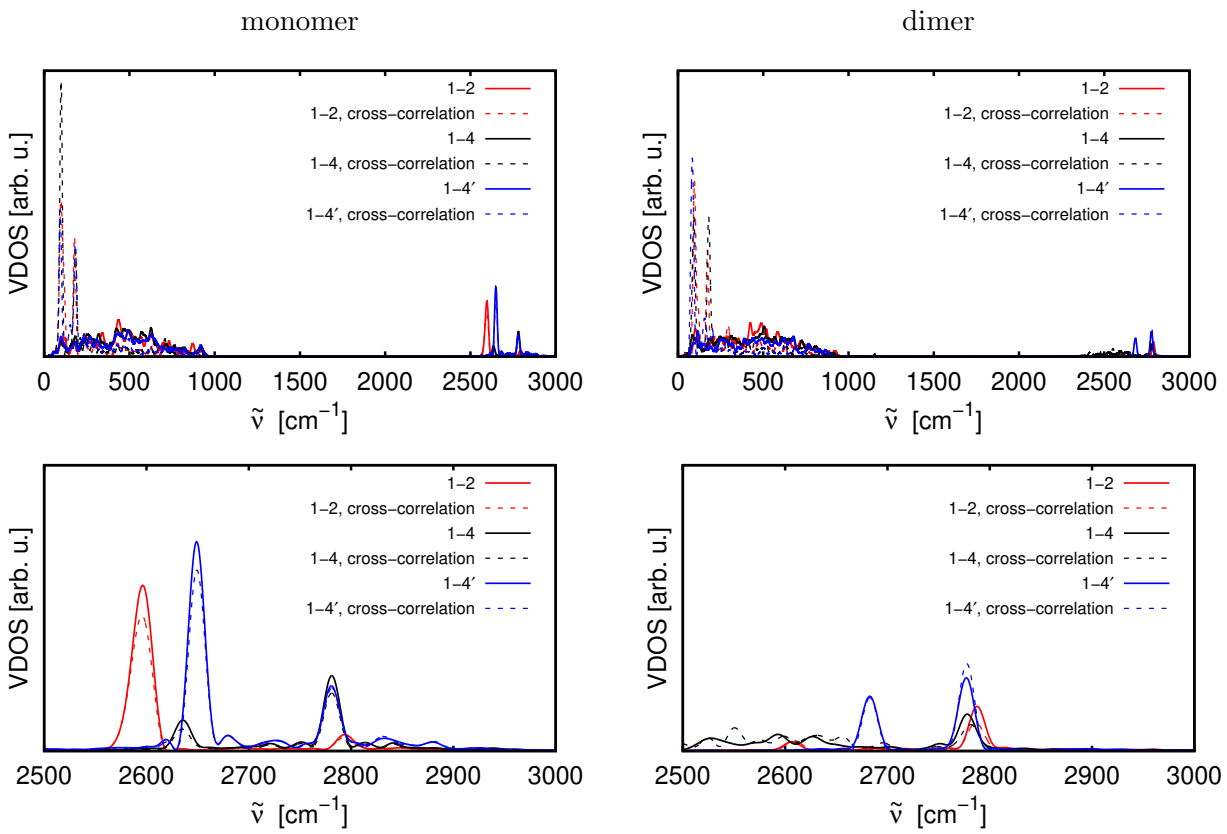

Figure 4.6: VDOS curves obtained by AIMD at 300 K employing full cross-correlation velocity-velocity autocorrelation functions, for the dissociated species 1-2, 1-4 and 1-4' for "monomers" (left) and "dimers" (right) of Fig.4.3 as starting configurations. Upper panels show the frequency range [0,3000] cm^{-1}, lower panels the OD stretching region [2500,3000] cm^{-1}. In the right panels, the VDOS scale is half that of the scale in the left panels.

$\sum_i^N \langle \underline{v}_i(0) \cdot \underline{v}_i(t) \rangle + \sum_{i \neq j}^N \langle \underline{v}_i(0) \cdot \underline{v}_j(t) \rangle$. The idea is to investigate the role played by intermode couplings on vibrational peaks of OD fragments. The new cross-VDOS curves obtained using also cross-correlation terms are shown in Fig.4.6. From the comparison with original VDOS curves, it emerges clearly that high-frequency modes are only slightly affected by the inclusing of $\langle \underline{v}_i(0) \cdot \underline{v}_j(t) \rangle$ in the calculation of VVAFs, namely both OD_{surf} and OD_{ads} stretching modes are quite efficiently decoupled from the other vibrations. On the contrary, the low-frequency portion of the VDOS spectrum is substantially different, if not in terms of absolute frequencies, certainly when looking at peak intensities. This observation is quite intuitive, since modes with lower wavenumber usually involve more collective, large-amplitude motions, as in surface lattice vibrations. Two very prominent peaks around 90-100 cm^{-1} and 170-180 cm^{-1} capture our attention: if compared to NMA results, they should correspond to in-plane motion of topmost surface atoms and to the z-oriented vibration of upper Al- and O-layers, respectively.

In general, the VDOS curves reflect the thermal motion of the adsorbates. This gives rise to new signals beyond NMA (most notably for the "1-4 dimer"), and to broadening of peaks beyond the energy resolution imposed by the finite propagation time. These effects will be analyzed in more detail in the following sections 4.4.3 and 4.4.4.

4.4.3 IR spectra from NVT/AIMD simulations

In this section we calculate IR spectra using AIMD at 300 K and adopting different polarization axes a, *i.e.*, $I_a^{\mathrm{IR}}(\omega) \propto \mathrm{Re}\{\chi_{aa}^{(1)}(\omega)\}$, for $a = x$, y, and z. Again, z is the direction perpendicular to the substrate, and x and y are orthogonal directions in the surface plane, as defined in the caption to Fig.4.3. The different polarization directions serve to model differently polarized IR experiments (*i.e.*, s- and p-polarization), and also improve insight into the nature of the sampled vibrational modes.

Let us consider the z-polarized spectrum of the "monomer" case first (lowest left panel in Fig.4.7), which can be considered as representative for a p-polarized IR spectrum. We see six peaks corresponding to the six different OD vibrations, at positions very close to those found in the VDOS spectra as listed in Tab.4.2. Both for 1-2 and 1-4', the lower-energy "surface OD" vibrations show a higher intensity than the "adsorbate OD" intensities, while for 1-4 it is the other way round. We assume that the intensity order observed for 1-2 and 1-4', is a consequence of the fact that the amplitude of the z-component of the transition dipole moment is larger for the "surface OD" than for the "adsorbate OD" vibrations. This indicates smaller polar angles θ, between the "surface OD" bond and the surface normal (the z-direction), than "adsorbate OD". In fact, the optimized structures of Fig.4.3 give $\theta = 37°$, 26°, and 29° for $\mathrm{OD}_{\mathrm{surf}}^{1-2}$, $\mathrm{OD}_{\mathrm{surf}}^{1-4}$, and $\mathrm{OD}_{\mathrm{surf}}^{1-4'}$, respectively, and 49°, 45°, and 53° for $\mathrm{OD}_{\mathrm{ads}}^{1-4}$, $\mathrm{OD}_{\mathrm{ads}}^{1-4'}$, and $\mathrm{OD}_{\mathrm{surf}}^{1-2}$, respectively. As shown in Appendix B, during the AIMD runs θ-distributions are formed, with similar mean θ values, $\langle\theta\rangle = 37°$, 30°, 35° for "surface OD", and $\langle\theta\rangle = 53°$, 54°, 58° for "adsorbate OD", respectively. Hence, the "surface OD" groups are more upright than the "adsorbate OD", both in the static and dynamic picture. Besides, not only the average orientation but also the distribution of θ-angles and the mobility of different OD groups is of importance for their spectral response, and dependent on the adsorption geometry. As outlined in Appendix B, analysis of the AIMD trajectories shows that for the 1-2 geometry steric hindrance seems to dominate the orientation and dynamic flexibility of OD bonds, while in the 1-4' structure we observe an opposite behaviour, with the two bonds acting as almost "free". An intermediate situation is found for the 1-4 adsorption geometry, where the formation of fluctuating hydrogen bonds seems to introduce a degree of correlation within their angular motion. These observations may provide an explanation for the special ordering of IR z-peak intensities, especially for the 1-4 example. Further, we note that the same intensity ordering as for I_z^{IR} is also found in the VDOS curve of Fig.4.5, lower left panel. We conclude that the z-polarized modes contribute dominantly to the vibrational response in p-polarized measurements.

The x- and y-polarized spectra, which can be related to s-polarized IR signals, are more complicated. First of all we see that different polarizations lead to different spectral behaviour. The x- and y-polarized spectra are less intense than the z-polarized ones (the intensity scale of z is two and four times more extended than x and y, respectively, see the caption of Fig.4.7). Further, for x- and y-polarization, we see that most of the spectra become much more structured than for z-polarization, with additional peaks showing up, even in frequency regions very close to 2900 cm^{-1}. Such high frequency modes can be associated with $\mathrm{OD}_{\mathrm{ads}}$ stretching vibrations oriented parallel to the surface plane. We also see large differences between x- and y-polarization. For instance, for the 1-2 dissociated species the $\mathrm{OD}_{\mathrm{surf}}^{1-2}$ peak around 2600 cm^{-1} is very pronounced in x-polarization, and has basically vanished under y-polarization. For the

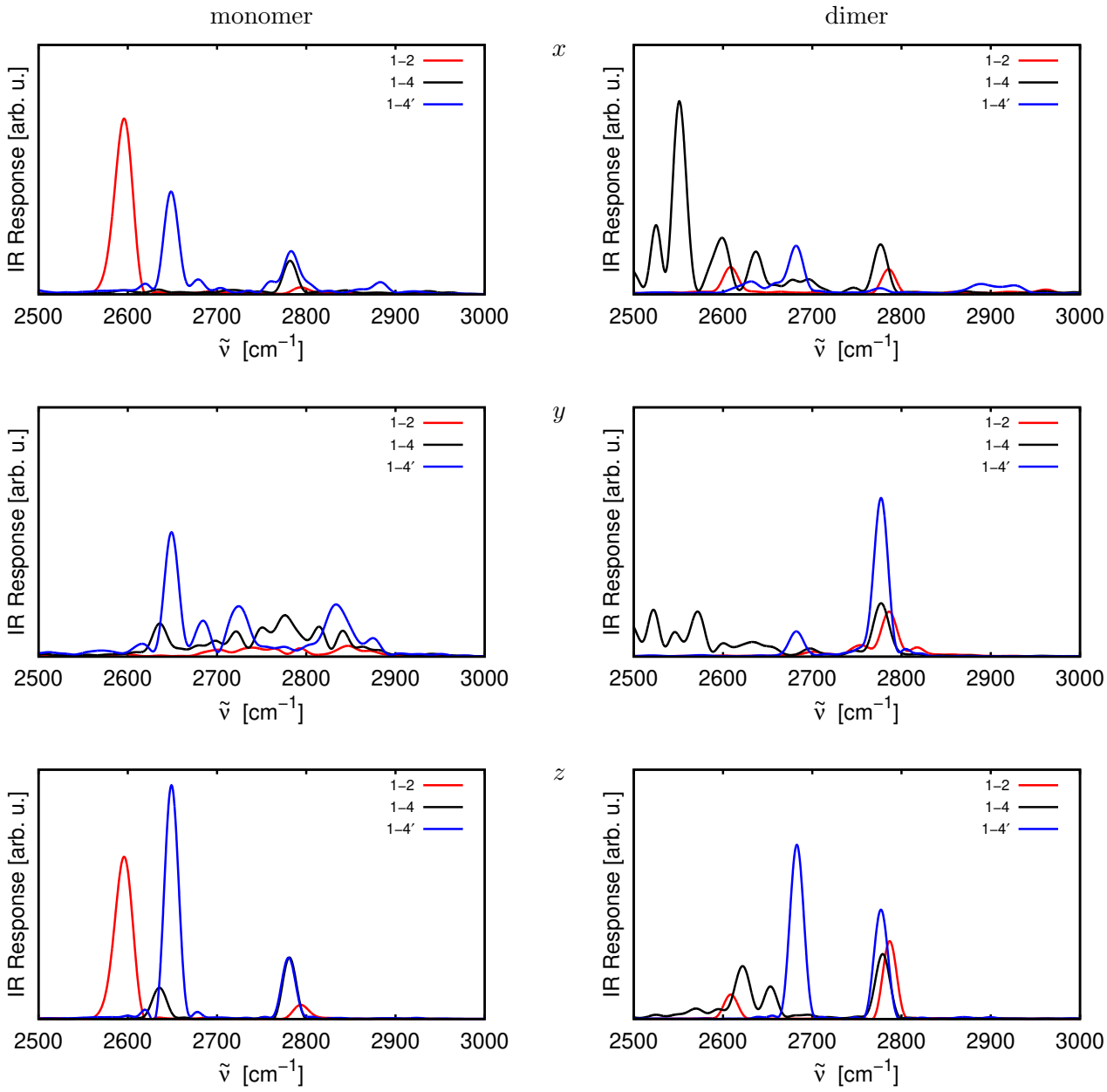

Figure 4.7: IR spectra of dissociated D_2O on α-$Al_2O_3(0001)$, obtained from the real part of the first-order susceptibility as $\mathrm{Re}\{\chi^{(1)}_{aa}(\omega)\}$, with different polarization axes a, namely x (upper panels), y (middle panels), and z (lowest panels). In the left panels IR spectra for the "monomer" dissociated species (coverage 1/4) are shown, in the right panels the corresponding "dimer" dissociated species (coverage 1/2) are considered. The IR intensities are given in "arbitary units", with the full ranges for the monomers obeying the ratio 2:1:4 for x:y:z, and for dimers 1:2:2.

lateral polarizations (in particular y), we see a tendency that higher-frequency signals, typically associated with "adsorbate OD" groups, gain intensity with respect to the lower-frequency "surface OD" peaks. This may be attributed to the higher flexibility of the former, with respect

to motions in the surface plane, compared to the latter. In fact, as one can intuitively expect, the "adsorbate OD" groups can rotate more freely around an azimuthal angle, ϕ, as shown in Fig.4.10 of Appendix B. There, very broad distributions $P(\phi)$ are found for the "adsorbate OD" groups, while those of the "surface OD" are more narrow.

We now analyze the IR spectra of "dimer" dissociated structures, which are shown in the right column of Fig.4.7. For z-polarization, we find similar peaks to those of the monomer case, albeit with different (relative) intensities and with 1-4 behaving somewhat special again, due to the formation of molecular water in some of the trajectories. The peculiarity of the 1-4 species shows up even more in the x- and y-polarized spectra, exhibiting many peaks, also in the low-energy region at 2500 cm^{-1} (and below), where otherwise no signals were found. In the x-polarized spectrum, also in the high-energy region around 2900 cm^{-1} we find resonances, attributable to the OD_{ads} fragments. In summary, for the dimer structures we obtain IR spectra with similar basic features as for the monomeric cases, however, with rather different intensities. If we exclude the interesting behaviour of 1-4, we relate the different intensities to local structural fluctuations, which for dimers are affected by the formation of temporary hydrogen bonds. We conclude that intensities are hence sensitive to the coverage, largely because of enhanced interactions between OD species. Further details on the effects of coverage to vibrational response are investigated in dedicated Appendix C.

4.4.4 VSF spectra from NVT/AIMD simulations

While direct validation of computed IR spectra with experiment is not available so far, VSF spectra obtained from theory can be compared with experimental ones, which have been collected for D_2O on Al-terminated α-$Al_2O_3(0001)$ in Ref. [12]. The coverage was very low in these experiments, but not unequivocally defined as in our structural models. In Ref. [12], both *ppp*- and *ssp*-polarization schemes (and two experimental geometries) had been employed. Here we present theoretical VSF spectra for *ssp*, *i.e.* as $|\chi^{(2)}_{xxz}|^2$. As explained above in Chapter 2, the calculation of *ppp*-polarized VSF spectra would require a weighted averaging over several tensor elements, which we have not attempted here. We show *ssp*-polarized VSF signals in Fig. 4.8, for the monomer (left panel) and dimer (right panel) dissociated structures, respectively.

The spectra in the left panel show that the OD^{1-2}_{surf} VSF signal at the xxz-polarization, around 2600 cm^{-1}, is by far the most intense. In fact, the OD^{1-2}_{ads} peak at around 2800 cm^{-1}, which was slightly noticeable in the z-polarized IR spectrum of Fig.4.7 and in the VDOS curves is now not seen on the scale of Fig. 4.8 – it is about of factor 2000 weaker than OD^{1-2}_{surf}. For the 1-4 and 1-4' structures, both peaks (for surface and adsorbate OD groups) are clearly seen in each case, however, their intensities are by far less intense than the OD^{1-2}_{ads} peak. Considering that under thermal equilibrium conditions at 300 K, the 1-4 and 1-4' adsorbates are minor species one would expect that the dominance of OD^{1-2}_{ads} is even more severe. For 1-4', around 2570 cm^{-1} a shoulder to the main peak at 2640 cm^{-1} is found, which could be assigned to a fluctuating hydrogen bonded vibration between the two OD fragments which is captured thanks to the finite-temperature AIMD sampling. In Tab.4.3, we list peak positions, along with computed linewidths 2Γ (Full Width at Half Maximum) and intensities, relative to the most intense resonance. We note that intensities have to be taken with care, since no weighting with the

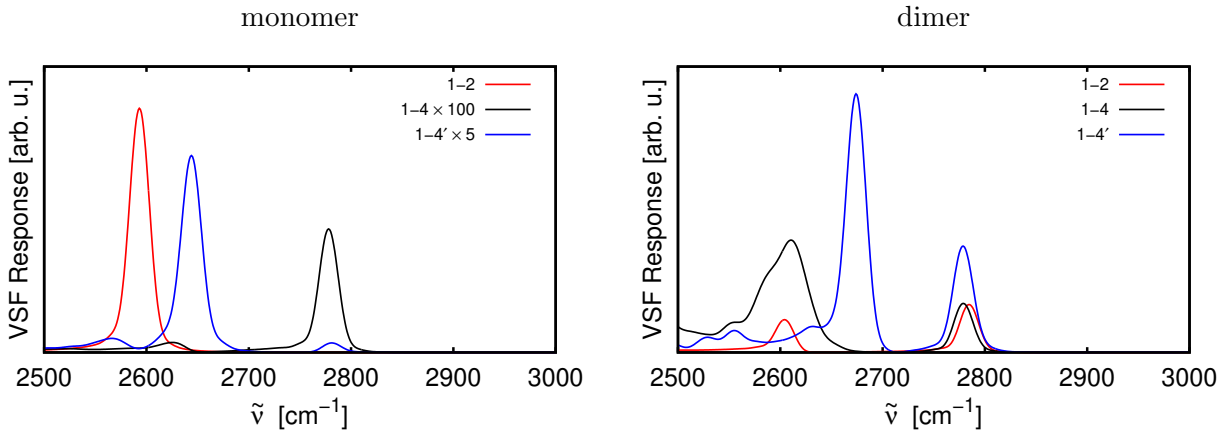

Figure 4.8: VSF signals representative for *ssp*-polarized experiments, obtained as $I_{\mathrm{ssp}}^{\mathrm{VSF}} \propto |\chi_{xxz}^{(2)}(\omega)|^2$. The left panel shows the VSF spectra for the "monomeric" dissociated species, while in the right panel spectra are shown for the "dimeric" dissociated models. For the left panel, scaling factors have been used as shown for 1-4 and 1-4', to make the figure clearer.

population of each species (Boltzmann or non-Boltzmann) was made, *i.e.*, strictly, only intensities for a given model (*e.g.*, $\mathrm{OD}_{\mathrm{ads}}^{1-2}$ with $\mathrm{OD}_{\mathrm{surf}}^{1-2}$) can be compared to each other.

In the experiment [12] (with the aid of NMA from theory), at the *ssp*-polarization, resonances for $\mathrm{OD}_{\mathrm{surf}}^{1-4'}$, $\mathrm{OD}_{\mathrm{ads}}^{1-4}$ and $\mathrm{OD}_{\mathrm{ads}}^{1-4'}$ (the latter two merged in one peak), and $\mathrm{OD}_{\mathrm{ads}}^{1-2}$ have been assigned, with the latter being the most intense, and $\mathrm{OD}_{\mathrm{surf}}^{1-4'}$ being the least intense. With a different geometry and *ppp*-polarization, resonances for the "surface OD" species, $\mathrm{OD}_{\mathrm{surf}}^{1-2}$, $\mathrm{OD}_{\mathrm{surf}}^{1-4}$, and $\mathrm{OD}_{\mathrm{surf}}^{1-4'}$ were reported. Both spectra (*ssp* and *ppp*) differ substantially w.r.t. to their peak intensities – in fact only with two different polarizations all resonances shown in Tabs.4.2 and 4.3 are present. In Tab.4.3 the VSF experimental intensities, relative to the most intense peak for a given polarization are reported, along with experimental linewidths 2Γ and, again, the experimental wavenumbers $\tilde{\nu}$ from Tab.4.3.

Referring to Table 4.3, we first of all recall that comparison between theory and experiment is not expected to be quantitative, because (i) the coverage in theoretical models is most probably higher than realized in experiment and (ii) *ppp*-polarization was not considered in theory as outlined. On top, in experiments the surface was prepared at T = 300 K but VSF measurements were carried out at lower T, whereas our simulations refer to 300 K throughout. Keeping these aspects in mind, we can still make the following observations: there is a certain mismatch of absolute frequencies, while frequency differences are reliable as outlined earlier. We find that theoretical and experimental linewidths agree very well for the "surface OD" species, while the spectral linewidths for the "adsorbate OD" are larger compared to experiment, by a factor of about two. We note, however, that in experiment the signal-to-noise ratio is much worse for *ssp* than for *ppp*, and thus peak widths at the *ssp*-polarization are not clear. We made sure by test calculations, that the theoretical linewidths are mostly due to dynamics and not due to the limited resolution of the Fourier transformation. As far as *ssp*-intensities are concerned,

Table 4.3: Characteristics of VSF spectra for dissociated D_2O at low coverage on a Al-terminated α-Al_2O_3(0001) surface. We show experimental peak positions $\tilde{\nu}$ again, along with corresponding VSF line widths and relative intensities, the latter separately for *ssp*- and *ppp*-polarization. In the right half of the table, the corresponding information as obtained by theory is given, where $\tilde{\nu}_{\max}$ now refers to the maximum of the VSF peaks. All frequencies / widths are given in cm^{-1}.

	experiment[1]				theory, monomer		
assignment	$\tilde{\nu}$	I^{VSF} (pol.)		2Γ	$\tilde{\nu}_{\max}$	I^{VSF} (pol.)	2Γ
OD^{1-2}_{surf}	2729±5	0.39 (ppp)		24	2593	1.00 (ssp)	24
OD^{1-4}_{surf}	2764±5	0.52 (ppp)		22	2630	0.002 (ssp)	18
$OD^{1-4'}_{surf}$	2790±3	1.00 (ppp)	0.11 (ssp)	20	2644	0.006 (ssp)	18
OD^{1-4}_{ads}	2900±7		0.91[2] (ssp)	40	2778	0.144 (ssp)	13
$OD^{1-4'}_{ads}$	2900±7		0.91[2] (ssp)	40	2780	0.005 (ssp)	15
OD^{1-2}_{ads}	2910±7		1.00 (ssp)	42	2797	0.0005 (ssp)	–

[1] From Ref. [12]; [2] both species seen as one peak with relative intensity 0.91.

it is not so easy to bring theory and experiment together. Under *ssp*-polarization (the only one considered in our simulations), we note that according to theory $OD^{1-4'}_{surf}$ is less intense than $OD^{1-4}_{ads}/OD^{1-4'}_{ads}$, in agreement with experiment. However, according to experiment OD^{1-2}_{ads} should be the most intense, contrary to what predicted with simulations. Of course, this may change when the fact is accounted for that 1-2 is the thermodynamically most stable species. On the other hand, from theory we should expect that OD^{1-2}_{surf} is seen also in an *ssp*-polarized VSF experiment (and not only for *ppp*), which is not the case according to Ref. [12]. In fact, OD^{1-2}_{surf} should be by far the most intense peak of all. In summary, when comparing experimental with theoretical VSF spectra, we conclude that, in the "monomer" model (coverage 1/4), frequency spacings between resonances agree very well (absolute frequencies reasonably well after frequency scaling), linewidths are in partial agreement with experiment, while intensities seem to deviate from each other.

Possible reasons for this mismatch in intensities are as follows. First of all, in experiment it is not entirely clear what "low coverage" means quantitatively. In particular the surface coverage defined in theoretical models is higher than in experiments, which obviously has a direct consequence on the VSF spectra. In fact, from Fig. 4.8, right panel, we see that by going to even higher coverage, namely a coverage of 1/2, the VSF spectra depend sensitively on it, as already observed for IR spectra above. Again, we should stress that for such coverage only few of possible dimeric minima have been investigated, so that a full structural sampling may lead to different vibrational responses. While peak positions and peak widths are not so much dependent on the presence of additional water fragments (apart from the fact that new peaks occur, as for IR), the signal intensities are very strongly affected. In fact from the right panel of Fig.4.8 we note that now, for the 1-2 species, for example, the *ssp* signal of OD^{1-2}_{ads} is more intense than the OD^{1-2}_{surf} peak, which is qualitatively in line with experiment. Also, the 1-2 resonances are no longer dominant over the 1-4 and 1-4' signals, at least when not considering that the latter are minor species. This could explain why these less stable species are seen in experiment.

Surface coverage accompanied by local interactions among "adsorbate OD" and "surface OD" also affects their average orientations. As described in Appendix B, the orientation assumed

by OD_{surf} bonds, which is reflected by their angular distributions, is extremely sensitive to the vicinity of the neighbouring OD_{ads}. Moreover, because of finite-temperature AIMD propagation, the angular distributions can span over several degrees. Thermally induced fluctuations in OD orientations are definitely more marked in our AIMD than in the common experimental assumption / condition [12, 135], where the orientational motion is considered very slow, potentially influencing the spectroscopic signals. This assumption has also been the subject of recent works [136, 137], which have underlined the relationship between VSF response and the timescale in which an oscillator reorients.

As explained previously in Chapter 2, the *ssp*-polarized VSF spectrum is not exactly equal to $|\chi^{(2)}_{xxz}(\omega)|^2$, since also the corresponding Fresnel factors for the given polarization scheme should be considered. We tested corrections by Fresnel factors [12, 138] for our systems but did not find any significant changes in the calculated VSF spectral responses. Most probably, this is due to the weak frequency-dependence of alumina's refractive index in the spectral range of OD stretching. Finally, being limited to tens of ps our model does not allow for the formation of surface defects and / or the full equilibration between different adsorbate species. Certainly, also the experiments leave room for improvement since the signals are weak and line fitting comes with considerable errors.

Appendix A: Proton transfer in the 1-4 dimer

As mentioned in the main text, during the canonical AIMD simulations for the 1-4 dimeric structure we observed a proton (more precisely: deuteron) transfer reaction from one of the two OD_{surf} terminations, to form a molecularly adsorbed D_2O, leading to a mixed dissociated and molecular configuration. In one of the two trajectories where such an event occurred, the D atom "jumped" relatively fast and moved to form D_2O after 400 fs. In the other reactive trajectory, such transfer happened later, after nearly 3 ps. In both of the two trajectories, no backreaction was observed, suggesting that the new mixed structure is energetically stabilized.

In order to rationalize these findings from a different angle, we performed Nudged Elastic Band calculations [77] at the DFT/PBE+D2 level of theory as implemented by the VTST package for VASP. Here we report the results obtained with the Climbing Image Nudged Elastic Band (CI-NEB) method [78] to study the reaction from the 1-4 doubly dissociated dimer, to the new (optimized) mixed structure. The result is shown in Fig.4.9.

As we see from the figure, the proton transfer leads to an energetically favoured mixed product, which is about 0.42 eV more stable than the educt configuration. Looking in more detail at the total energy profile (red curve), a possible transition state was found at the second CI-NEB image, with an activation energy $\Delta E^{\ddagger} = E^{\ddagger} - E(\text{educt})$ being only 0.01 eV ($\ddagger$ indicates a transition state). Static NMA calculations on this structure retrieved a single imaginary frequency, indicating a transition state (TS). Specifically, we found that the TS frequency $\tilde{\nu}_{TS} = 57i$ cm^{-1}, corresponding to the upward motion of Al CUS atom connected to the OD_{surf} from which the D-atom transferred. We also calculated an activation free energy, $\Delta G^{\ddagger} = G^{\ddagger} - G(\text{educt})$ at 300 K, giving 0.036 eV. We may also estimate a rate for the reaction, using Eyring's equation [139] $k(T) = \frac{k_B T}{h} e^{-\Delta G^{\ddagger}(T)/k_B T}$, giving $k = 1.53 \times 10^{12}$ s^{-1}. We thus expect a transfer process on the timescale of picoseconds, which makes our observations in AIMD plausible. A backreaction

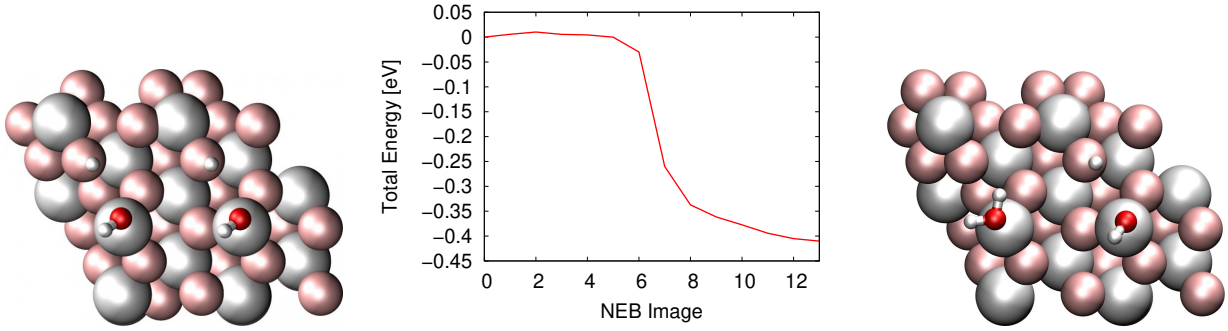

Figure 4.9: Reaction profile for the proton (deuteron) transfer in the 1-4 dimer model. In the doubly dissociated model (left), a deuteron moves from a OD_{surf} fragment to an OD_{ads} fragment to form molecularly adsorbed D_2O, in a mixed configuration (right). In the middle, a CI-NEB path is shown, showing that the mixed configuration is more stable and separated from the reactant configuration by a very shallow barrier only.

will happen on much longer timescales, since then the activation free energy is an order of magnitude larger. We note that PBE+D2 usually underestimates activation barriers and overestimates rates (see Ref. [130] for a quantitative statement), but it is nevertheless conceivable that ultrafast proton (deuteron) transfers will happen on the water / alumina interface, aided by cooperative surface phonon involving topmost Al atoms.

A pending question concerns why such phenomenon has been observed only for the 1-4 dimeric structure and not for the other two dimers as well, at least within the limited simulation times adopted here. A possible explanation is the fact that the 1-4 dissociated dimer structure is the least stable according to Tab.4.1 (in contrast to the monomer, where 1-4' is the least stable). In addition, the higher surface coverage allows for a long-range stabilization among the different OD fragment due to fluctuating hydrogen bonds which are not easily inferable from static DFT calculations. Further, among the possible dissociation sites (1-2, 1-4 and 1-4'), the 1-4 configuration allows for an intermediate distance between the "OD surface" and "OD adsorption" fragments (around 2.85 Å) which may be favourable for deuteron motion: In 1-2, this distance maybe too short ($\sim$ 2.5 Å) and lead to a greater steric hindrance in the 1-2 structure, or too large for 1-4' ($\sim$ 4.1 Å) for an effective deuteron transfer to take place.

Appendix B: Orientational distribution of OD bonds

In the main text we have shown that even at low coverages (1/4 and 1/2) structural fluctuations affect vibrational (IR and VSF) spectra. In this Appendix we want to further analyze orientational behaviour of the various OD bonds during NVT / AIMD trajectories at 300 K. To this end, in Figs.4.10 and 4.11 we show angular distributions for both OD_{surf} and OD_{ads} fragments for all monomeric and dimeric, dissociated starting structures. In particular, we calculated angular distribution (percentage) probabilities as $P(\theta) = \frac{n_\theta}{N_t} \times 100\%$ and $P(\phi) = \frac{n_\phi}{N_t} \times 100\%$, respectively. Here, n_θ and n_ϕ are the numbers of timesteps associated to a certain value of the polar (θ) and the azimuthal (ϕ) angles in "boxes" 5° wide (see figure), and N_t is the total number of timesteps. The polar and azimuthal angles are respectively defined as: $\theta = \arccos(\frac{z_{OD}}{l_{OD}})$ and $\phi = \arctan(\frac{y_{OD}}{x_{OD}})$, where q_{OD} ($q = x, y, z$) indicates the q-th Cartesian component of an OD

interatomic bond vector (see Fig.4.3 for the coordinate system), and $l_{\mathrm{OD}} = \sqrt{x_{OD}^2 + y_{OD}^2 + z_{OD}^2}$ is the bond length corresponding to this bond vector.

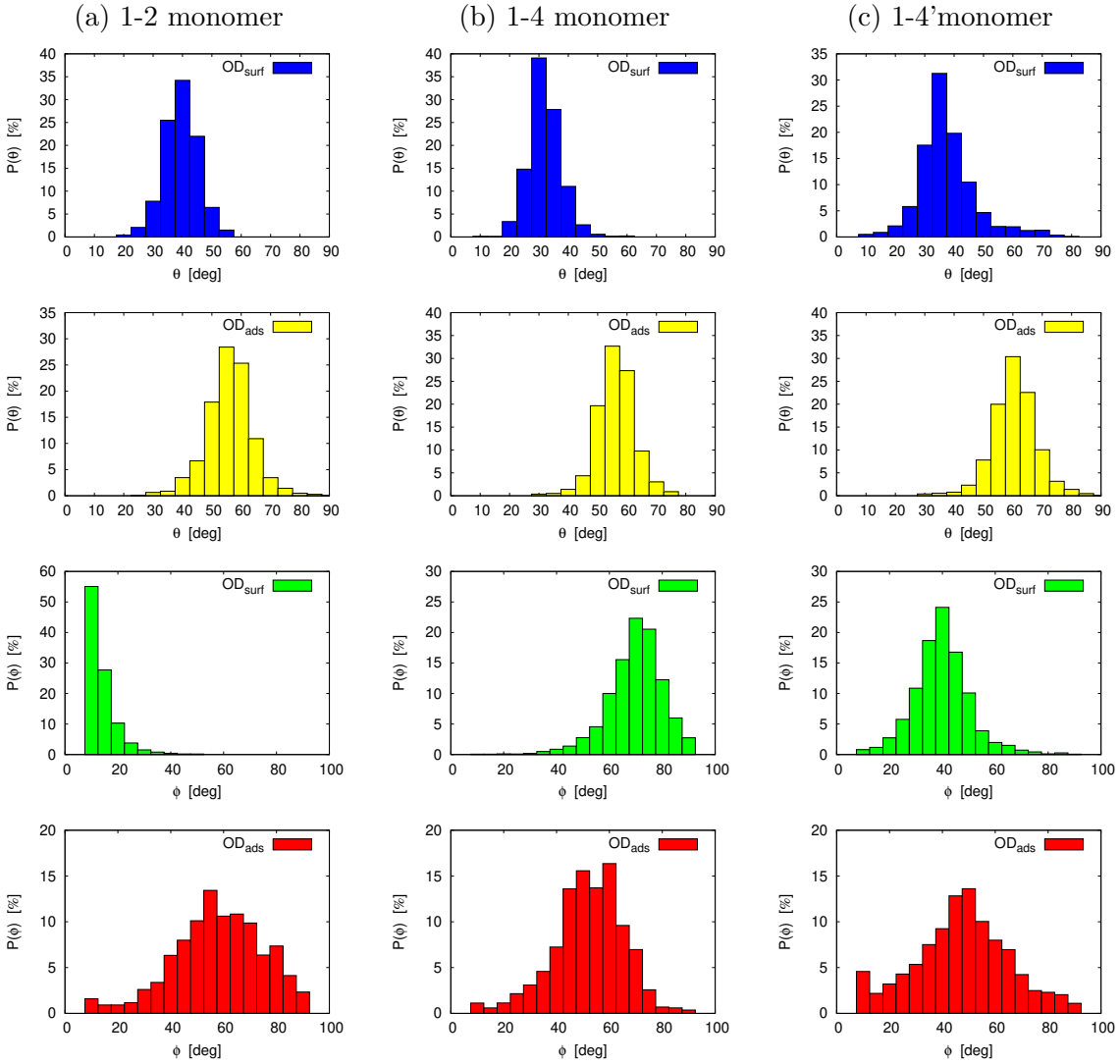

Figure 4.10: Ensemble-averaged, percentage probability distributions of polar and azimuthal angles, $P(\theta)$ and $P(\phi)$, for both $\mathrm{OD_{surf}}$ and $\mathrm{OD_{ads}}$ fragments during AIMD trajectories at 300 K. Each column corresponds to the different monomer dissociated structures as in Fig.4.3: 1-2, 1-4 and 1-4'.

Looking at the monomer dissociated samples first, from Fig.4.10 we note that the three 1-2, 1-4 and 1-4' structures are characterized by an increasing conformational freedom thanks to the larger distance between dissociated D_2O fragments. We can observe that while OD polar angles seem not to be greatly affected by how close $\mathrm{OD_{surf}}$ and $\mathrm{OD_{ads}}$ are, the lower panels of Fig.4.10 clearly show that the "in-plane" angular dynamics depends on steric hindrance especially for

the OD_{surf} fragment.

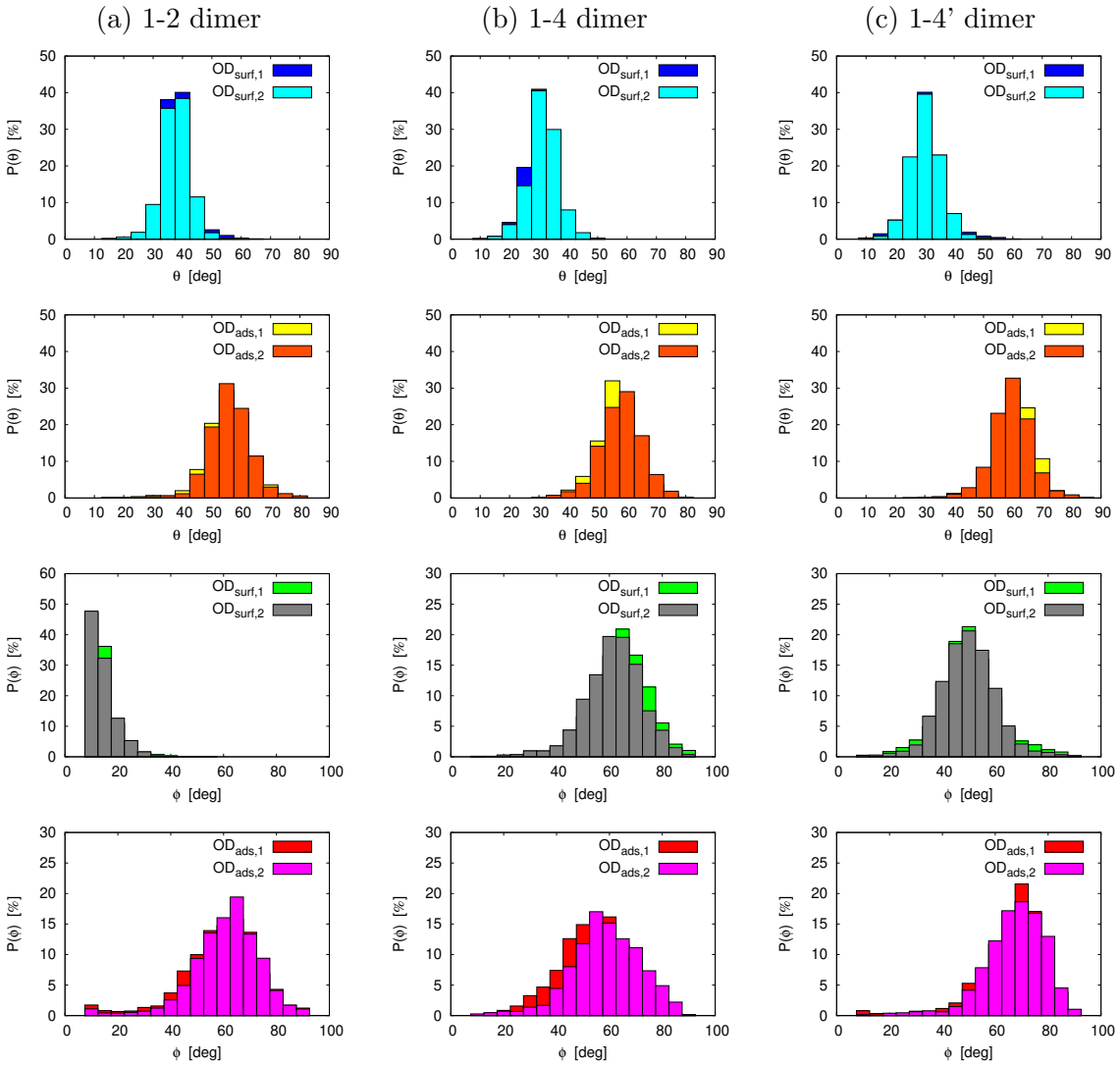

Figure 4.11: Ensemble-averaged, percentage probability distributions of polar and azimuthal angles, $P(\theta)$ and $P(\phi)$, for all four OD_{surf} and OD_{ads} fragments during AIMD trajectories at 300 K. Each column corresponds to the different dimer dissociated structures: 1-2, 1-4 and 1-4'.

Similar arguments can be put forward for the dissociated, bimolecular structures reported in Fig.4.11. Looking at both polar and azimuthal angular distributions we retrieve similar features as observed above. While the relative symmetry of adsorption sites seems to generally characterize the orientational dynamics of dimeric structures, we notice that in the 1-4-dim case the two OD_{surf} bonds have on average a slightly "uneven" behaviour. This special feature can again be explained with the occurrence of trajectories affected by D atom transfer.

Appendix C: VDOS from NVE/AIMD simulations

When employing (*ab initio*) classical molecular dynamics for spectral simulations, an important issue regards the effect which the canonical propagation may have to the computed spectra. In fact, as one realizes the constant T propagation thanks to coupling with a thermal bath, such bath may introduce spurious effects which are seen in the vibrational responses. For instance, by coupling with specific system's degrees of freedom, the bath may alter their "natural" vibrational frequencies. To avoid such effects, a strategy is to employ the NVT / AIMD propagation only as thermalization and then to further propagate in the microcanonical (NVE) ensemble the equilibrated trajectories. Within NVE conditions, no coupling to external bath (or fictitious Nosé-oscillators) is employed, hence all artificial interactions can be avoided. This procedure, of course, charges the price of not setting the temperature to a fixed value, therefore allowing greater thermal fluctuations.
In order to check the reliability of computed NVT / AIMD spectra, we took the same trajectories and further ran them in the NVE ensemble. Here we focus on the monomeric species (1-2, 1-4 and 1-4') for which we collected additional 50 ps (5 trajectories × 10 ps, each), where the last 2 ps of each AIMD run have been sampled to collect vibrational responses as VDOS curves (analogously to what was done before).

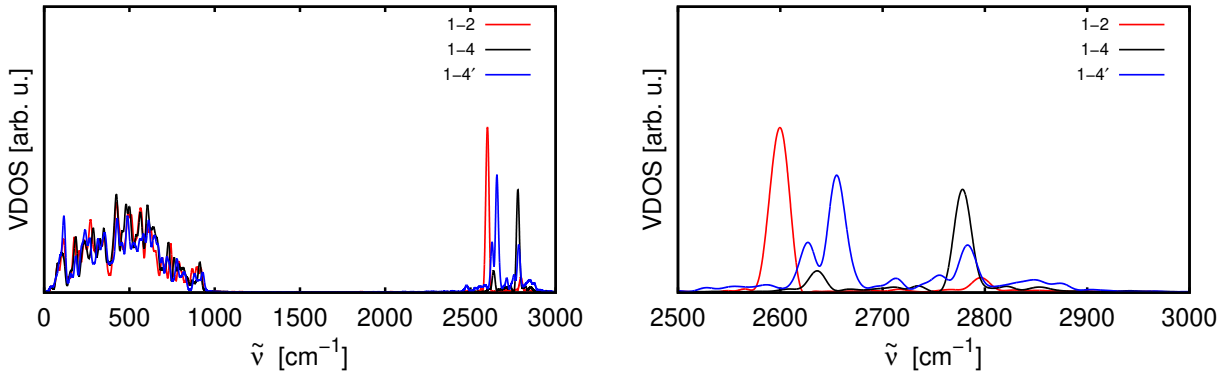

Figure 4.12: VDOS curves obtained by AIMD at 300 K within the microcanonical ensemble (NVE), using the dissociated species 1-2, 1-4 and 1-4' for "monomers". Left panel show the frequency range [0,3000] cm^{-1}, right panel the OD stretching region [2500,3000] cm^{-1}. In the right panel, the VDOS scale is half that of the scale in the left one.

Despite few changes in the individual peaks, for instance the OD_{surf} stretching signals for 1-4' seems splitted in two resonances, no substantial difference can be observed when comparing the VDOS curves obtained from NVT or from (thermalized) NVE propagation. In fact, while certain differences would arise simply by the longer propagation time (in total, NVT + NVE trajectories have been run for 20 ps) and by the consequent better equilibration of adsorption structures, Fig.4.12 clearly shows that the NVT dynamics cannot be considered an appreciable source of errors in the calculation of vibrational responses, at least within the timescales and

the temperature range considered here.

Appendix D: Vibrational spectra of molecularly adsorbed water (D_2O) from AIMD

For the sake of completeness, AIMD simulations for the molecularly adsorbed water species have been run, with both NVT and (further) NVE settings. For such a system, given the less rigid structure and the possible encounter of on-surface diffusion / reactions, we calculated canonical trajectories starting from the PBE+D2 optimized structure shown in Fig.4.2 for a total of 80 ps (16 ps × 5), while the microcanonical ones have been propagated for additional 40 ps (8 ps × 5). In analogy with the unimolecularly dissociated D_2O species (1-2, 1-4 and 1-4'), we computed vibrational responses from NVT / AIMD trajectories (taking the last 2 ps of each run for sampling), which are shown in Fig.4.13 as VDOS curves. Clearly, the spectrum of molecularly adsorbed water (D_2O) differs from the dissociated monomers: first, we notice the appearence of an additional low-frequency band around 1150 cm^{-1} corresponding to water bending vibration. Secondly, even the higher frequency portion of the spectrum has different features, most notably the total absence of peaks above 2700 cm^{-1}. This indicates that even considering the pre-discussed 100 wavenumbers redshift compared to experimental VSF resonances, no molecularly adsorbed water should be found on the Al-terminated (0001) surface where D_2O has been impinged using MBS, otherwise unequivocal signatures of its vibrational modes would have been detected.

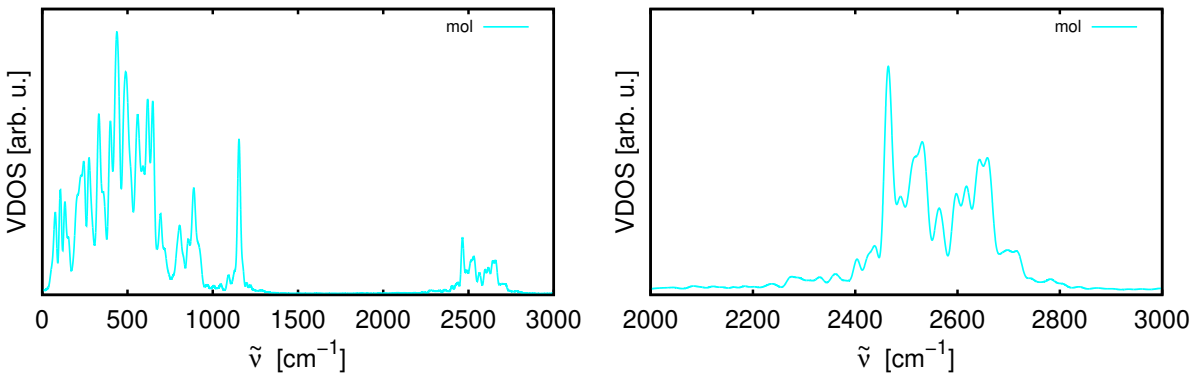

Figure 4.13: VDOS curves obtained by AIMD at 300 K for molecularly adsorbed water from Fig.4.2. Left panel shows the frequency range [0,3000] cm^{-1}, while right panel the OD stretching region [2500,3000] cm^{-1}. In the right panel, the VDOS scale is half that of the scale in the left panel.

As further investigation of the behaviour manifested by adsorbed water on the (0001) surface, NVE / AIMD trajectories have been calculated starting from the equilibrated NVT runs. Interestingly, while in the canonical dynamics no reactive processes could be observed but rather

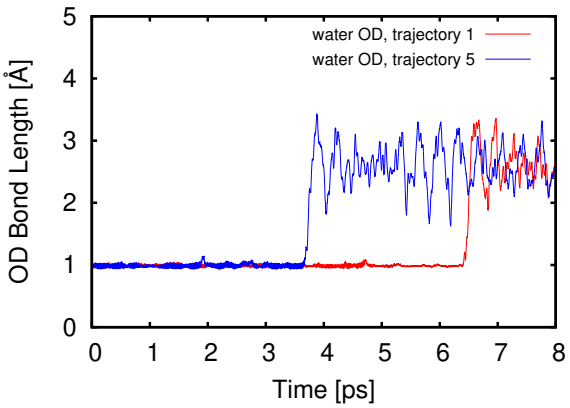

Figure 4.14: Plots of dissociating OD bond lengths in molecularly adsorbed water during thermally-equilibrated NVE / AIMD trajectories.

only rearrangements of D_2O molecule around its adsorption position on an Al CUS atom, during two of the NVE trajectories water did eventually split to form the 1-2 dissociated species. We report this reactive trajectories in Fig.4.14, where the internuclear OD distance is plotted for the dissociating bonds: in one case, trajectory n. 1, the reaction happened after nearly 6.5 ps, while in ther other case the D_2O splitting occurred after not even 4 ps. Overall, the timescale over which the water dissociation happened is in very good agreement with kinetic estimations done by Wirth *et al.* [128], where a reaction rate of $\frac{1}{20}$ ps^{-1} had been computed. Interestingly, when comparing with the mixed dissociated structure examined in Appendix B, where the CI-NEB computed rate was 1.5 ps^{-1}, we see that the presence of already dissociated water on the (0001) surface can presumably speed the D_2O splitting reaction by a factor of 30.

Appendix E: Coverage effects on VDOS spectra, from 1/4 to 1 ML

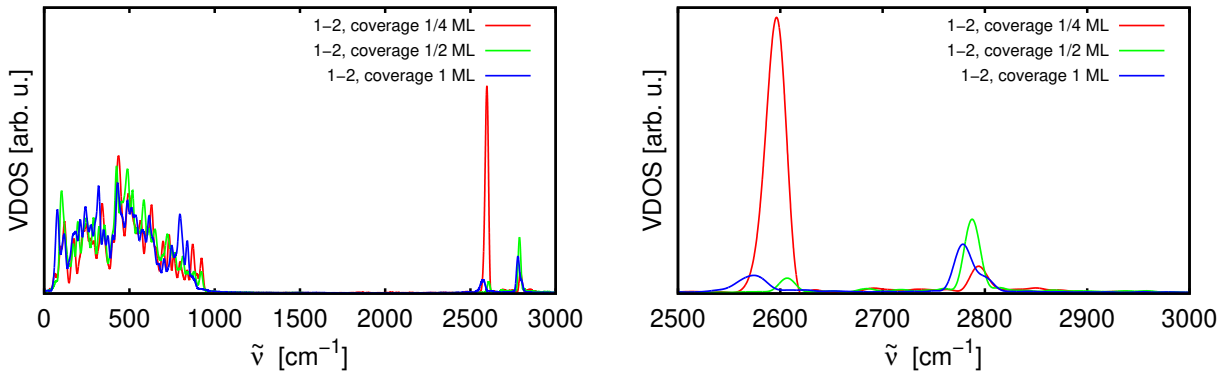

Figure 4.15: VDOS curves obtained by AIMD at 300 K for "1-2" dissociated species, considering the monomer (in red, coverage 1/4 ML), the dimer (in green, 1/2 ML) and the tetramer (in blue, 1 ML). Upper panel show the frequency range [0,3000] cm^{-1}, while right panel the OD stretching region [2500,3000] cm^{-1}. In the right panel, the VDOS scale is half that of the scale in the left panel.

As pointed out in the main text, our theoretical spectra show a clear dependence on surface coverage, as already visible in Fig.4.5, when comparing VDOS of monomeric and dimeric species. While coverage seems to affect OD stretching frequencies only slightly, the effect on vibrational peaks is more prominent. In order to further investigate the role played by water content on the Al-terminated (0001) surface vibrational response, we ran additional NVT / AIMD simulations using the very same settings and time propagation described above. For such a case, we considered a new "1-2 tetrameric" structure, corresponding to a full 1 ML coverage, namely with all four Al CUS atoms saturated by D_2O adsorption. The resulting picture can be observed in reported VDOS curves of Fig.4.15, where the full range of coverages (from 1/4 to 1 ML) is shown.
As we can see by comparing the different VDOS spectra obtained, increasing the number of dissociated water molecules on the 2×2 (0001) surface produces strong modifications, especially in the OD stretching region. Absolute stretching frequencies are only partially affected, with a coverage-dependent redshift of few wavenumbers, fully consistent with the increasing hydrogen bonding interactions. Peak intensities are instead definitely influenced, with the OD_{surf} stretching signal being very pronounced for the 1/4 coverage case, but becoming less and less intense due to higher water loading. Interestingly, no big changes are seen in the low frequency band of the VDOS, indicating that surface vibrations and OD (frustrated) bending may be less affected by the coverage effect.

5 Vibrational Spectra of the Hydroxylated α-Al_2O_3(0001) Surface with (and without) Water [2]

The theory of quantum mechanics also explained all kinds of details, such as why an oxygen atom combines with two hydrogen atoms to make water, and so on. Quantum mechanics thus supplied the theory behind chemistry. So, fundamental theoretical chemistry is really physics.

Richard P. Feynman

5.1 Water-covered α-Al_2O_3(0001) surfaces: A DFT and AIMD investigation

The behaviour of water towards the (0001) surface of aluminum oxide has been investigated in this work, so far only with respect to UHV conditions [1, 12]. However, as already pointed out in the surface science literature [140–145], the importance of atomistic simulations about metal oxides in aqueous environments is undeniable. This is why we turn now to the aforementioned α-alumina surface, persuing computational models that go in the direction of modelling the solid / liquid interface.

In the present, theoretical work we investigate as a model system the α-Al_2O_3(0001) surface [12, 126, 128, 146], in particular its hydroxylated, or OH-terminated, form which results from the interaction of α-alumina with air or water H_2O under ambient conditions. By adding small amounts of water to the naked, but hydroxylated, surface its spectroscopic response will change, giving molecular insight into the water / metal oxide interface. Employing the same methodology [1, 61] used to simulate vibrational spectra (VDOS, IR and VSF) of dissociatively adsorbed water on the Al-terminated (0001) surface we now address the spectroscopic responses of different systems, namely the hydroxylated alumina surfaces, with and without additional water [2]. The analysis performed at very low water coverage presented in Chap.4 can be seen as complementary to the current subject.

The aqueous alumina / water interface has extensively been studied in the past both from experimental and theoretical points of view, thus serving as an ideal testing ground for new theoretical methods. Most previous computational studies on the vibrational spectroscopy of α-Al_2O_3(0001) in contact with water focused on the surface / liquid (bulk) water interface, partially using methods similar to ours. For instance, in the seminal works of Refs. [121, 147] the interfacial properties of oxide/water systems (including α-alumina) were characterized by DFT-AIMD with respect to their vibrational properties (analyzed by VDOS curves) and their surface acidity. Another example is the DFT-AIMD calculation of IR spectra reported in Ref. [122]. For the IR spectra dipole-dipole correlation functions were used, as determined by maximally

localized Wannier functions [60]. In both studies the authors considered the (0001) termination in contact with (bulk) $H(D)_2O$, addressing the different vibrational signatures related to "ice-like" and "liquid-like" bands from interfacial water and to "in-plane" or "out-of-plane" surface OH(D) bonds forming H-bonds to neighbouring water molecules. Finally, we would like to mention the study [125], in which mixed molecular dynamics simulations based on classical force fields and DFT were adopted to (re)parametrize dipole moments and polarizabilities. In this study both VDOS and *ssp*-polarized VSF spectra were calculated with methods similar to ours [2], however, using more sophisticated (and costly) approaches for dipole moments and polarizabilities required in VSF spectroscopy.
To the best of our knowledge, no work exists so far on a systematic comparison of VDOS-, IR- and VSF-based vibrational analysis of water on α-alumina in environmental conditions, in particular not in case of model system consisting of a hydroxylated surface with and without (a few) adsorbed water molecules. This is one motivation of the present work, as we already achieved for the study of water dissociative adsorption on the Al-terminated (0001) surface [1] as reported in Chap.4. The most important goal of our work, as in the previous section, is an in-depth analysis of the high-frequency signals in vibrational spectra particularly of the alumina / water interface. In particular, we offer a new interpretation of the vibrational signals around 3700 cm^{-1} to be dominated by "upward"-oriented non H-bonded aluminol OH groups of the hydroxylated alumina surface, independently of the presence or absence of additional water.

5.2 Computational models and their realization

5.2.1 Details of DFT and AIMD calculations

For studying the hydroxylated α-Al_2O_3(0001) surface with and without additional water, we performed geometry optimizations, NMA and AIMD simulations at the DFT / PBE+D2 level of theory, as previously reported in Chapters 3,4. We used 2×2 cell slab models, with same dimensions and characteristics as the ones employed in Refs [1, 2, 12, 128]. Based on these references, we built and considered two main structural models: the fully hydroxylated α-Al_2O_3(0001) surface ("HS" in what follows, being the (0001) surface the most stable termination under UHV conditions [11, 92, 98, 100, 112, 118, 119]), and the latter with additional eight, adsorbed H_2O molecules ("HS+2ML" in what follows). We refer to this system as the "2 MonoLayers" (2ML) model, HS+2ML, because there are twice as many water molecules as Al-CUS sites of an Al-terminated 2×2 cell of α-Al_2O_3(0001). They are shown in Figs.5.1(a) and (b), respectively, as top and side views.

For NMA, no frequency rescaling was performed despite the PBE exchange-correlation functional usually underestimates water frequencies by typically a few tens of wavenumbers [148].
For AIMD, a set of trajectories was collected within a canonical ensemble (NVT) at 300 K using the Nosé-Hoover thermostat [36–38]. We chose to start our AIMD trajectories from the optimized PBE+D2 geometries of the HS and HS+2ML models, as shown in Fig.5.1. Initial velocities were generated randomly according to a Boltzmann distribution at $T = 300$ K. For the two systems, using a timestep of $\Delta t = 0.2$ fs we ran simulations for a total of 200 ps for HS, and 240 ps for HS+2ML. Technically, this was done by running ten trajectories for each system, each of them being 20 or 24 ps long, respectively. Most of the propagation time was used for equilibration, and only the last segment of each trajectory as a "production run" for sampling correlation functions in an interval $[0,t_{\mathrm{samp}}]$. Different sampling times t_{samp} between

2 and 6 ps have been tested, leading to VDOS spectral resolutions between 6 cm^{-1} (for 6 ps) and 17 cm^{-1} (for 2 ps). Convergence tests showed no significant changes among the calculated VDOS using different sampling times, therefore we decided to employ $t_{samp} = 2$ ps, in analogy to the analysis reported in Chapter 4.

5.2.2 Details of surface slab models

The hydroxylated surface ("HS") in Fig.5.1(a) forms from the so-called Al-terminated, UHV-stable (0001) surface [11, 92, 98, 100, 112, 118, 119]. The latter has an atomic-layer sequence Al-O_3-Al-Al-O_3-Al-R, where "R" stands for a repetition of the Al-O_3-Al sequence into the bulk (when referring to a 1×1 cell). Under ambient conditions, *i.e.*, when exposed to air or liquid water, the top layer Al-atoms are removed and the (now) topmost O layer is saturated with hydrogen. In this case the atomic-layer sequence becomes $(HO)_3$-Al-(Al-O_3-Al)-R. We consider in addition, five Al layers (two double-layers with four Al each, one single layer with four Al atoms), and two oxygen layers (each with twelve O atoms), giving a simulation cell of composition $Al_{20}O_{36}H_{12}$. Within a 2×2 cell, we have therefore twelve terminating OH bonds.
It has been already observed in previous studies [121, 122, 125, 146, 147], that the terminating Al_2-OH units of the hydroxylated alumina, henceforth called "aluminols", can be found in two main, quite stable configurations depending on the relative orientation of the OH bond with respect to the surface plane: one more perpendicular (u) where the polar angle θ between the OH bond and the surface normal is $< 45°$, and one more "parallel" (p) where the polar angle is $> 45°$, sometimes close to 90°. As indicated in the main text, in Fig.5.1(a) an optimized structure with eight parallel (green ellipses) and four upright OH bonds (red circles) is shown, called a "p_8u_4" configuration there (or "*ppu*" when referring to a 1×1 cell with three OH groups). From an earlier investigation [146] of the hydroxylated surface with a 1×1 unit cell (using a centro-symmetric, two-sided model with 36 atomic layers and three OH groups on both sides of the slab), we know from PBE+D2 energies that a configuration with one of the three aluminols arranged with OH "up" and two "parallel" (*i.e.*, a *ppu* configuration), is the most stable arrangement in that case; another structure with two perpendicular aluminols and one parallel (*uup*) being almost degenerate and only 0.01 eV higher in energy. Other arrangements were found to be energetically more unstable.

For the "HS" system, in AIMD and also for geometry optimizations and NMA, only the uppermost three atomic layers (an O layer and a double-layer of Al) plus the hydrogens were allowed to move, while the lower layers were kept frozen at bulk geometries [146]. This limitation was partially dictated by the costly AIMD calculations; its reliability was checked in comparison with models with more extended, multi-layer models [128, 146].

The "HS+2ML" surface structure in Fig.5.1(b) was found particularly stable in this work, as outlined in the main text. This is due to the formation of a quite stable honeycomb-like layer network consisting of water hexagons. Indeed, the adsorption energy per water molecule computed as $E_{ads} = (E_{HS+2ML} - E_{HS})/8 - E_{H_2O}$, is -0.83 eV on the PBE+D2 level of theory. Specifically, the formation of hydrogen bonds between aluminol OH groups and molecular H_2O becomes possible, in addition to those H-bonds which already exist for HS, between p aluminol OH groups and neighbouring surface O atoms. The additional H-bonds also affect the configuration assumed by the different aluminol OH units. In the structure shown we have: four u aluminol OH bonds which are H-bonded to water (all u, red-circled OH of Fig.5.1(a), upper

panel) and four p aluminol OH bonds which are H-bonded. For the remaining four non-hydrogen bonded aluminols, two are found with a p orientation and the others being more upright, u (*e.g.*, the OH in the center of the six-ring is u). Hence, the overall structure is p_6u_6 in this case.

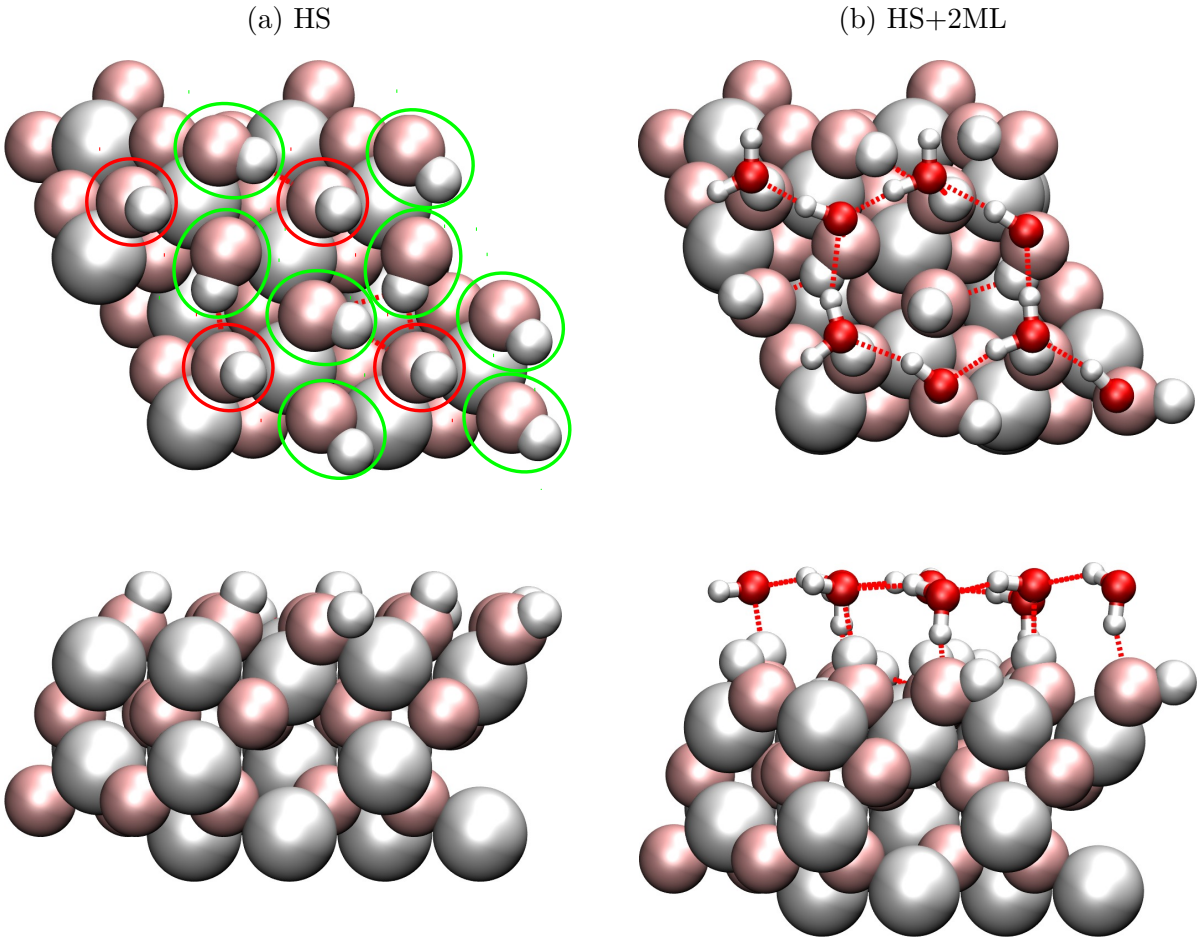

Figure 5.1: Top (top) and side views (bottom) of the hydroxylated α-$Al_2O_3(0001)$ surface (2×2), without (a, HS) and with additional eight water molecules (b, HS+2ML). Our models have a stoichiometric composition of 68 ($Al_{20}O_{36}H_{12}$) and 92 atoms ($Al_{20}O_{36}H_{12} \cdot (H_2O)_8$), respectively. Surface atoms are shown as "van-der-Waals spheres" in pale colors, water thin films in a "ball-and-stick" representation (H in white, Al in grey and O in red). For HS, top, "upright" u and "parallel" p aluminol OH groups are indicated by red circles and green ellipses, respectively. In (b), hydrogen bonds are indicated by dashed red lines. In AIMD, only the upermost two atomic layers (an O layer and a double-layer of Al) plus the adsorbate atoms were allowed to move, while the lower layers were kept frozen at bulk geometries.

We stress that both the HS and HS+2ML structures shown are only two of many possible minima. We use these optimized structures as starting points for AIMD simulations at finite temperature. In fact, at 300 K, u and p aluminol OH groups flip rapidly between each other, on a ps-timescale (see Appendix), this way probing many local structural minima. This demonstrates

the advantage if not necessity, of basing the analysis of vibrational spectra at finite temperature on AIMD, as already pointed out in seminal reviews [121, 147, 149].

5.3 Results and discussion

5.3.1 Vibrational frequencies from Normal Mode Analysis

The characterization of vibrational modes was first of all achieved by NMA. Tab. 5.1 lists calculated frequencies for the systems of Fig.5.1: the fully hydroxylated surface (HS) and the hydroxylated surface with 2ML of water (HS+2ML).

HS		HS+2ML	
ω [cm^{-1}]	assignment	ω [cm^{-1}]	assignment
3746-3745	OH str (al-OH (u))	3761-3758	OH str (al-OH (u), no hb)
3682-3606	OH str (al-OH (p))	3603-3599	OH str (al-OH (p), no hb)
		3515-3016	OH str (al-OH+water, hb)
		1663-1600	H_2O bend
1078-115	al-OH bend, surf-pho	1195-136	H_2O libr, al-OH bend, surf-pho
		100-64	H_2O layer-pho

Table 5.1: Vibrational frequencies at the DFT/PBE+D2 level of theory for the fully hydroxylated α-Al_2O_3(0001) surface (HS), and HS with water, HS+2ML. Abbreviations: "al-OH"= aluminol OH, "u"= up, "p"= parallel, "str" =stretching, "bend"= bending, "libr"= libration, "(sur-)pho"= (surface) phonons, "hb"= hydrogen-bonded (to water molecules).

The HS system has a high-frequency regime at $\sim$ 3600-3750 cm^{-1} and a low-frequency regime at and below $\sim$ 1100 cm^{-1}. The higher frequencies are due to aluminol OH vibrations, with the p aluminol OH being red-shifted with respect to the u aluminol OH bonds by $\sim$ 70-140 cm^{-1}. The red-shift is due to the fact that the latter form hydrogen-bonds with neighbouring O atoms of the alumina surface, while the upright OH bonds remain quasi-free. The low-frequency regime found for HS in Tab.5.1, left half, is due to Al_2-OH bending modes and AlO surface phonons [146].

For HS+2ML the vibrational signatures are enriched by, for instance, the bending mode of H_2O around 1600-1700 cm^{-1}, or low-frequency "phonons" of the entire water layer at 100 cm^{-1} and below. Moreover, the whole region between 3500 and 3000 cm^{-1} emerges with addition of water. This band corresponds to hydrogen-bonded OH stretching vibrations of water or aluminol OH groups. Further, the HS vibrational region between $\sim$ 1100 and 130 cm^{-1} which we attributed to "bending" of Al_2-OH units and to surface phonons, contains now also water librations in case of HS+2ML. Another detail to note when looking at OH stretching vibrations of HS+2ML for aluminols which are free, *i.e., not* bound in H-bonds with water molecules ("no hb"), is that these vibrations are shifted compared to the aluminol OH vibrations of the water-free HS surface: the p aluminol-OH without H-bonds to water are red-shifted by between 10-80 cm^{-1} compared to HS, and the free u aluminol OH bends without H-bonds to water are slightly blue-shifted with respect to corresponding HS OH bonds. Hence, the water network has also an influence on those aluminol OH bonds which are not H-bonded to water.

Concerning the accuracy of the reported NMA and the effect of layer thickness on it, we should mention that a comparison with previous calculations using double-slab two-sided 1×1 unit cell models with 36 atomic layers [146] indicates almost perfect agreement with only slight changes in absolute frequencies for OH stretching modes (at most by 16 wavenumbers).

In summary, the adsorption of non-dissociated water causes new features and also frequency shifts of previously observed modes. In particular, a general relationship regarding OH (aluminol) vibrational stretching frequencies is found as:

$$\omega(\mathrm{OH}_u^{\mathrm{nhb}}) > \omega(\mathrm{OH}_p^{\mathrm{nhb}}) > \omega(\mathrm{OH}_p^{\mathrm{hb}}) > \omega(\mathrm{OH}_u^{\mathrm{hb}})$$

where *"nhb"* stands for "non-hydrogen bonded" (to water). Such new features can be pictorially understood by looking at the structural heterogeneity of OH bonds associated with aluminols and water layer. In Fig.5.2 we sketched this variety of hydrogen bonding from the HS to the HS+2ML models, represeting different configurations of p-, and u-aluminols involved (or not) in hydrogen bonds with neighbouring H_2O molecules.

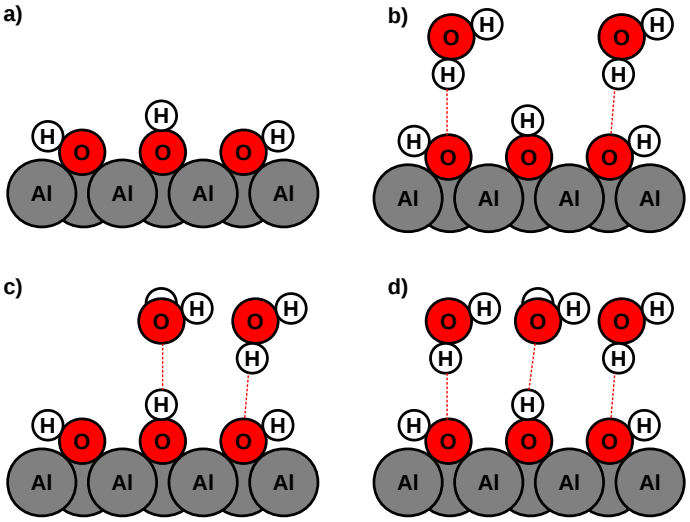

Figure 5.2: Pictorial representation of different hydrogen bonding and structural configurations present in the HS and HS+2ML models. In a) aluminols of the fully hydroxylated surface are shown, while the cases b), c) and d) focus on the latter water-covered surface.

5.3.2 Vibrational Density Of States (VDOS) from NVT/AIMD simulations

To account account for anharmonic motion and finite temperature beyond NMA, we computed VDOS curves through MD trajectories with Eq.(2.18). The *total* velocity-velocity autocorrelation function $C_{vv}(t) = \langle \underline{v}(0)\underline{v}(t) \rangle$ gives the VDOS *via* its Fourier transform according to Eq.(2.38).

Fig.5.3 shows resulting VDOS curves obtained for (a) the fully hydroxylated surface (HS) and (b) the water-covered surface (HS+2ML), respectively, with total and atom-projected contributions, in the interval [0,4000] cm^{-1} (upper panels) and in the "OH region" [3000,4000] cm^{-1}

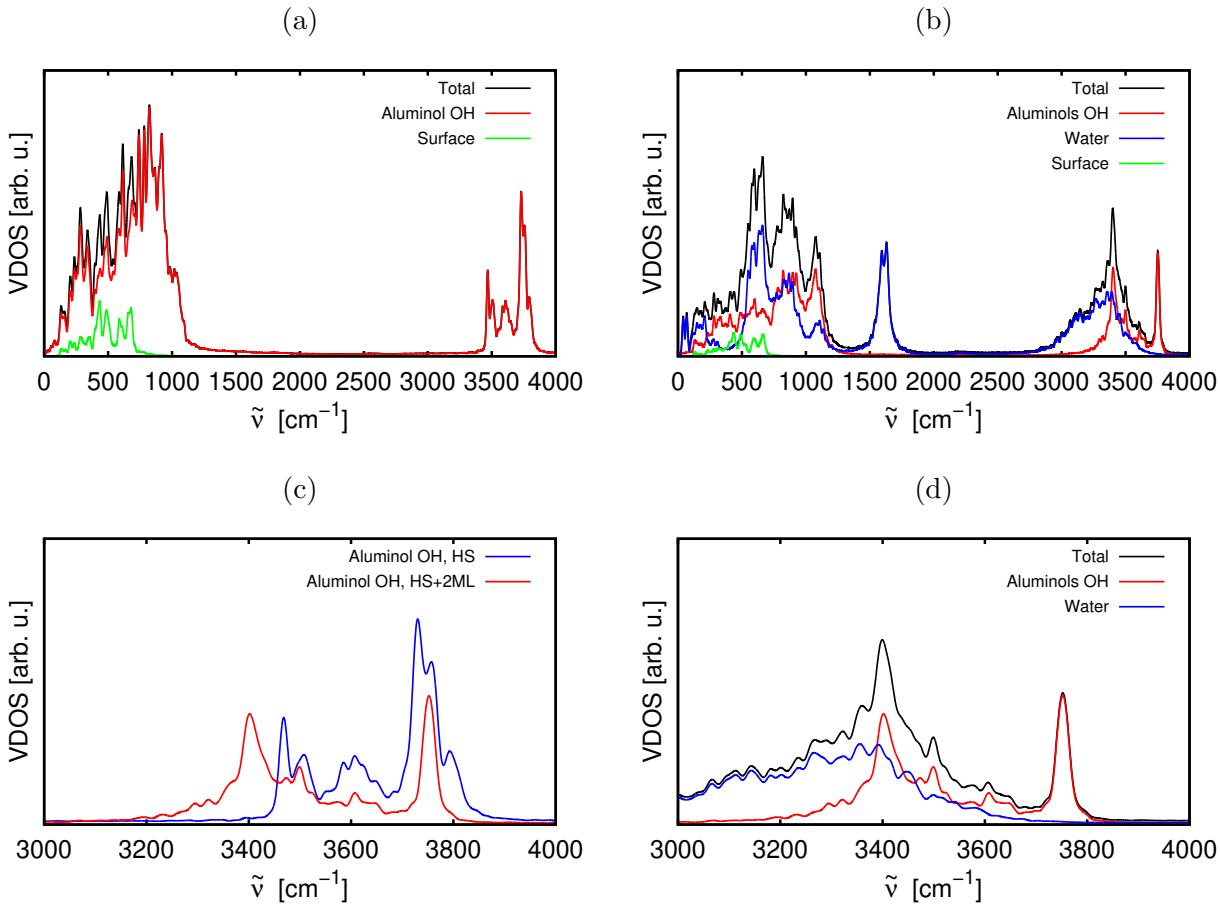

Figure 5.3: Calculated total (black curves) and subsystem VDOS (aluminols: red, water layer: blue, surface atoms: green) obtained from AIMD/NVT at 300 K: (a) for the fully hydroxylated (0001) surface, HS, and (b) for the fully hydroxylated (0001) surface with eight water molecules, HS+2ML. (d) is a zoom of (b) into the "OH region". In (c) the aluminol OH VDOS is shown in the "OH-region", now for HS and HS+2ML models in comparison. VDOS curves were obtained as average from ten trajectories, each one propagated for 20 ps (for HS) and 24 ps (for HS+2ML), respectively, whereby only the last 2 ps were used as sampling times t_{samp} in Eq.(2.38).

(lower panels). Both total and subsystem VDOS (for aluminol OH and water layer) are shown. For the subsystems, only the O and H atoms of the aluminol OH were considered in the correlation function (for HS), or aluminol O and H and all water atoms were considered (for HL+2ML).

Comparing the AIMD VDOS curves with frequencies calculated by NMA indicates that the harmonic frequency regions are roughly resembled by the VDOS. In particular, the additional features due to the adsorbed water are also clearly seen in VDOS curves, most notably those around 1600 cm^{-1} (the H_2O bending modes), and the broadened nature (with respect to HS), of the high-frequency band centered around 3700 cm^{-1} towards lower frequencies.

The VDOS at 300 K contains also features which are missing in the NMA spectra. For instance, the OH-region of the hydroxylated surface without water (Fig.5.3(c), in blue), shows

non-vanishing VDOS in regions where no normal modes frequencies are found: in the low-frequency OH region between 3450 and 3550 cm^{-1} and in the high-frequency OH region above 3750 cm^{-1}. The new features result in an overall broadening of the vibrational signal. This broadening can be due to thermal motion, anharmonic shifts (which are expected to lead to red-shifts mostly), and, possibly, due to combination bands (which can lead to higher frequencies than found in NMA).

Comparing the VDOS of the total HS system with that of the aluminol OH bonds only in Fig.5.3(a), we can clearly see that the VDOS for HS is dominated by aluminol OH vibrations, especially in the high-frequency region where the total and aluminol VDOS curves match almost perfectly. Only at very low frequencies below 1000 cm^{-1}, in the phonon band, the total VDOS slightly differs from the aluminol one, indicating that non-OH vibrations come into play here.

In Fig.5.3(b) and (d) (the OH-frequency region of (b)), the total VDOS for HS+2ML is compared to the VDOS of aluminol OH bonds only, and of the water layer only, respectively. We see for HS+2ML (Fig.5.3(b) and (d)) that the total spectrum is dominated by both aluminol OH and water vibrations. From Fig.5.3(b) we can immediately assign the peak at $\sim$ 1600 cm^{-1} to H_2O (bending) modes. From Fig.5.3(d) we note that the peak around 3750 cm^{-1} and several peaks in the range 3300-3600 cm^{-1} are aluminol OH vibrations. Closer inspection shows (see also Tab.5.1), that the peak at $\sim$ 3750 cm^{-1} is due to non-hydrogen bonded, "free" aluminol OH with dominant u orientation. The (red-shifted) peaks in the range 3300-3600 cm^{-1} are hydrogen-bonded OH stretching modes. In particular, the peak at 3400 cm^{-1} is assigned to the (four) u aluminols, which are hydrogen-bonded to water molecules on top (*cf.* Fig.5.1(b)). In the broader interval [3000,3600] cm^{-1}, there is also an appreciable contribution of water-OH stretching vibrations (in blue), which in fact dominate the region between 3000 and 3300 cm^{-1}. It is also of interest to directly compare the effect of water adsorption on hydroxylated (0001) on aluminol OH vibrations, which is displayed in Fig.5.3(c). In fact, the nature of these modes has been discussed widely in several works both from the theoretical and the experimental point of view [110,121,122,125]. As seen from the figure, the presence of additional H_2O creates the new peak located at around 3400 cm^{-1} and diminishes peak intensity associated to parallel (p) and perpendicular (u) non-hydrogen bonded aluminols in the range [3600,3800] cm^{-1} of HS. Further, in the HS+2ML model we have the single peak around 3750 cm^{-1} (non-hydrogen bonded, free, u aluminol OH), while without water we see a broader peak (with three sub-peaks) $\sim$ 3750 cm^{-1}. This broader peak arises from larger conformational flexibility for the u aluminol OH groups (see Appendix).

5.3.3 IR and VSF spectra from NVT/AIMD simulations

Based on the understanding of VDOS signatures, we explore IR and VSF spectra. First, we calculated IR spectra, $\chi^{(1)}_{zz}(\omega)$, *via* Eq.(2.43). In Fig.5.4(a), we show the real part of $\chi^{(1)}_{zz}(\omega)$ as a measure for the IR spectrum, both for naked and water-covered α-Al_2O_3.

We see that stretching of non-hydrogen bonded, perpendicular (u) aluminols between 3700 and 3800 cm^{-1} dominate the spectra and, signals in the range between 3450-3650 cm^{-1} for HS+2ML, and a strong peak at 3400 cm^{-1} for HS are missing. The missing features are due to aluminol OH bonds and / or to water vibrations parallel to the surface.

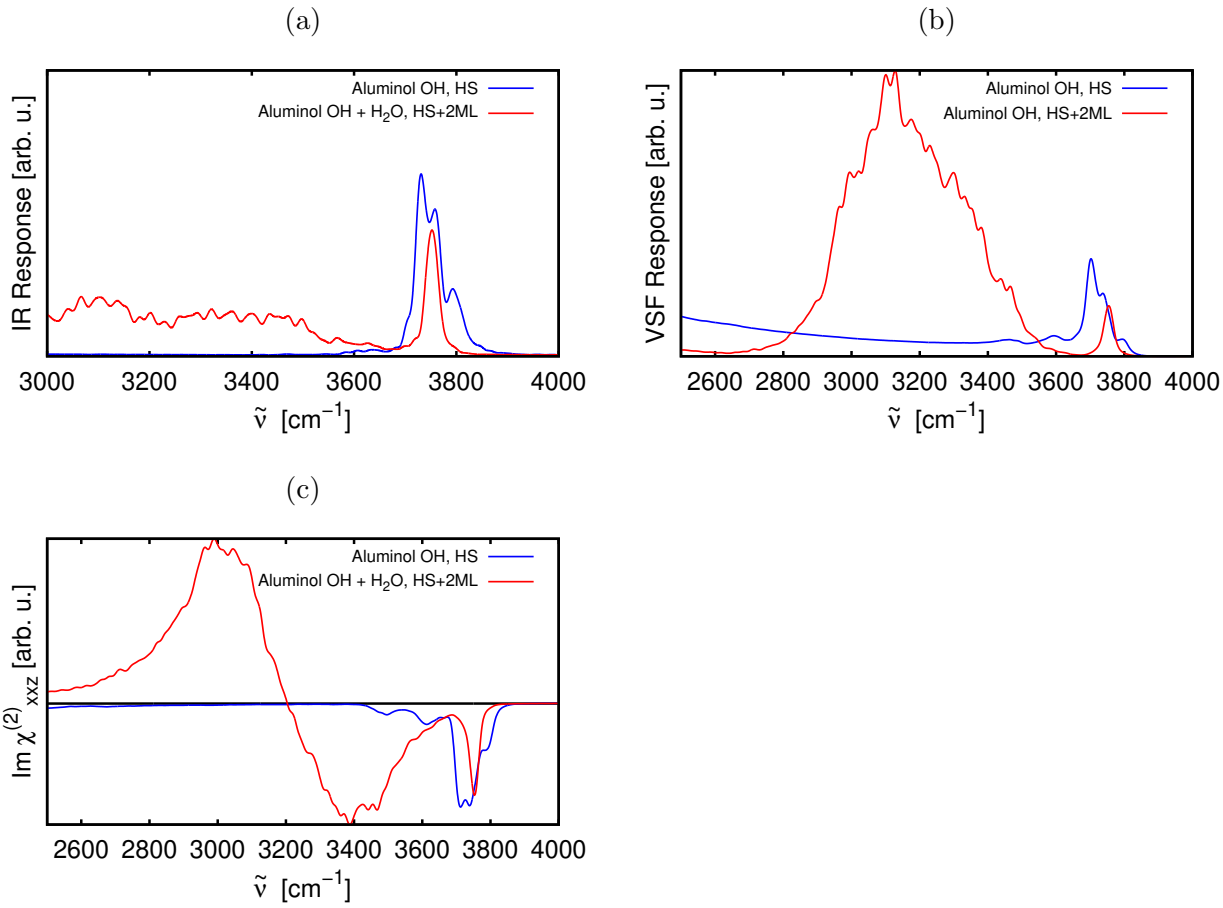

Figure 5.4: (a) IR response (as real part of the first-order susceptibility, $\mathrm{Re}\{\chi^{(1)}_{zz}(\omega)\}$) for OH stretching of the fully hydroxylated surface HS (blue) and the HS+2ML surface (red). (b) VSF response (as square of the second-order susceptibility $|\chi^{(2)}_{xxz}(\omega)|^2$) for OH bonds from the fully hydroxylated surface HS (blue line) and the water-covered surface, HS+2ML (red line), in the interval [2500,4000] cm^{-1}. (c) The corresponding imaginary part of the second-order susceptibility, $\mathrm{Im}\{\chi^{(2)}_{xxz}(\omega)\}$. The horizontal line is the zero-line in (c). All curves were calculated as averages over the same trajectories as before, from correlation functions involving only the O and H velocities over the last 2 ps of each trajectory.

On the other hand, other features of the IR spectra as the high-frequency peaks between 3700 and 3800 cm^{-1} are almost indistinguishable from the VDOS curve. This indicates that the non-Franck Condon prefactor in Eq.(2.43) plays a limited role in this region. Therefore, the IR spectrum deviates from the VDOS spectrum mostly due to orientational effects.

Besides IR spectra, we here present simulations of VSF spectra for the two systems under study, using the NVT/AIMD approach. As mentioned above, we are interested in an *ssp*-polarization experiment with exciting UV/vis and IR light sources being s-polarized, and the detection of the sum-frequency signal is done in p-polarization. This is achieved by approximating the VSF signal as $I_{\mathrm{ssp,VSF}}(\omega) \propto |\chi^{(2)}_{xxz}|^2$. The VSF signal is calculated *via* Eq.(2.44),

including all OH groups of the naked and water-covered, hydroxylated α-alumina (0001) surfaces.

Fig.5.4(b) displays the computed VSF signal for the HS and HS+2ML models. We recognize the high-frequency peaks located at $\sim$ 3700-3800 cm^{-1}, similar to the IR and VDOS spectra. For both systems there are no strong signals corresponding to non-hydrogen bonded, parallel (p) aluminols, since their stretching modes do not break the surface symmetry. These modes were clearly seen in VDOS (see Fig.5.3(c)), in the region from 3400-3700 cm^{-1}, but were also absent in IR spectra (*cf.* Fig.5.4(a)). For HS+2ML, the strongest signal is in the hydrogen-bonded region between 2800 and 3500 cm^{-1}: this indicates that VSF probes stretching modes from hydrogen-bonded aluminols as well as various OH stretching modes of H_2O molecules.

Further structural information on VSF-active modes can be gained from the imaginary part of the second-order susceptibility, which is experimentally accessible *via* so-called "heterodyne detection" [150]. Roughly speaking, for the present case, the imaginary part gives information on the orientation of VSF-active OH groups.

In Fig.5.4(c) we show $\mathrm{Im}\{\chi^{(2)}_{xxz}(\omega)\}$ for both model systems. Accordingly, for HS, the features which appear in the VSF spectrum (a) (between 3400 and 3800 cm^{-1}) have $\mathrm{Im}\{\chi^{(2)}_{xxz}(\omega)\} < 0$, *i.e.*, the corresponding OH groups are dominatly upward-oriented, with O closer to the surface than H – as it trivially should be the case for this surface. In contrast for the HS+2ML surface, there are two regions: VSF signals above 3200 cm^{-1} have also $\mathrm{Im}\{\chi^{(2)}_{xxz}(\omega)\} < 0$, while for $\omega < 3200$ cm^{-1}, $\mathrm{Im}\{\chi^{(2)}_{xxz}(\omega)\} > 0$. This sign alternation of the imaginary susceptibility is consistent with the usual convention such that the surface-normal vector is directed towards the solid. We interprete the negative portion as being due to OH bonds (aluminol and / or water) which are dominatly oriented upward, while the positive portion comes from OH bonds of the water layer pointing downward to the (0001) surface.

At this point it is worthwhile to make contact with experiment. Shen and coworkers [110] reported VSF measurements on the α-alumina (0001) / air and α-alumina (0001) / water interfaces. The total VSF spectrum measured at the the alumina/air interface shows a clear peak at ca. 3700 cm^{-1} and a smaller peak at around 3400 cm^{-1}. The 3700 cm^{-1} peak is preserved by adding water, while additional peaks at 3450 and 3200 cm^{-1} appear. The different peaks located in the hydrogen-bonded region were assigned to Al_2-OH bonds and H_2O molecules involved in hydrogen bonds with different possible orientations [110]. Furthermore, the imaginary part of the second-order susceptibility was reported. For example, for the alumina/water interface at pH=9, both negative and positive regions were found for the imaginary part in a region between 3000 and 3800 cm^{-1} similar to Fig.5.4(c), with a sign-change occurring around 3300 cm^{-1}.

In a more recent work of Tong *et al.* [146], a systematic experimental VSF study of α-Al_2O_3(0001) surfaces with various levels of hydroxylation was performed, from the fully hydroxylated to the OH-free, Al-terminated surface. The authors provided VSF spectra in the OH stretching region between 3400 and 3900 cm^{-1}. They found a peak centered at ca. 3710 cm^{-1}, and a very small signal at ca. 3480 cm^{-1} for the hydroxylated surface, similar to Ref. [110]. No clear signal was found for the Al-terminated surface. The first peak has a full width at half maximum (FWHM) of nearly 120 cm^{-1}.

When we compare our simulated VSF spectra with these experimental works we notice that the high-frequency signals at and slightly above 3700 cm^{-1} are present in experiment and in theory. Moreover, both experimental studies provide support for the conservation of the high-frequency peak(s) for the air/solid and the liquid/solid interface of α-alumina. The experimental VSF given in [110] for the liquid/solid interface, suggests the presence both of aluminols, and of physisorbed water on the surface in order to explain the sign alternation in the imaginary part of the second-order susceptibility. Although the relative intensities of the experimental spectra for the water-covered interface do not fully match our calculated *ssp*-VSF spectra, we can find reasonable similarities between our simulation of the HS+2ML model system and the experiments performed by Zhang *et al.* for the alumina/water interface. In particular, we find a sign-change of the imaginary part of the second-order susceptibility in the same region as they do (for pH=9). The experimental VSF spectra provided by both Zhang *et al.* and Tong *et al.* for the fully hydroxylated (presumbaly water-free) surface is also consistent with our result (blue curve in Fig.5.4(b)), both as far as the width of the main signal and the occurrence of (a) low-frequency side-peak(s) are concerned.

There are also differences between theory and existing experiment, however. For instance, in the simulated VSF for the water-covered surface we see a strong, even dominating signal centered around 3100 cm^{-1}, while in experiment this region shows only low-intensity signals (compared to the highest-frequency peak). In fact, according the difference between alumina/air and alumina/water interfaces is less pronounced than in our calculations. Of course it must be noted that, from the experimental side, it is not entire clear how water-free the alumina/air interface is. From the theoretical side, it is also not clear if the HS+2ML model adequately represents the alumina/water interface (at finite pH) as studied in Ref. [110]. It is also possible that certain discrepancies may result from the OH transition dipole and polarizability parametrization we employed as multiplicative factors for the first-order and the second-order susceptibilites. While the parametrization by Skinner and coworkers should be in principle applicable to different aqueous environments as metal oxide / water interfaces, we cannot exclude that new parametrizations could improve the spectroscopic signatures of the aforementioned systems.

Appendix: Orientational behaviour of surface aluminols

As previously reported for dissociated water species on the Al-terminated (0001) surface, AIMD trajectories at 300 K are accompanied by distinctive orientational freedom of aluminols. Trajectories were analyzed, with special emphasis on the surface OH bonds and the effect of water on them. First of all, the four upright (u) (corresponding to the four red encircled OH groups in Fig.5.1(a)) and the four parallel (p) aluminol OH bonds of the HS+2ML starting structure which are engaged in H-bonds with water molecules on top, are found to be rather stiff in dynamics: they stay in u or p orientation, only slightly vibrating around their equilibrium positions in the AIMD runs (not shown). All other (four) non H-bonded aluminol OH groups of the HS+2ML starting structure, and also all (twelve) aluminol OH of the HS starting structure, on the other hand, are dynamically more flexible at 300 K.

In Fig.5.5 we report average angular distributions obtained from NVT/AIMD for OH polar angles ($\theta = \arccos(\frac{z_{\mathrm{OH}}}{l_{\mathrm{OH}}})$, where l_{OH} is the bond length). Distributions are calculated as $P(\theta) = \frac{n_\theta}{N_t} \times 100\%$, where N_t is the total number of MD timesteps and n_θ is the number of

timesteps associated to a certain value of the polar angle. Different histograms are reported for initially "up" and "parallel" aluminols orientations, considering the two HS and HS+2ML models.

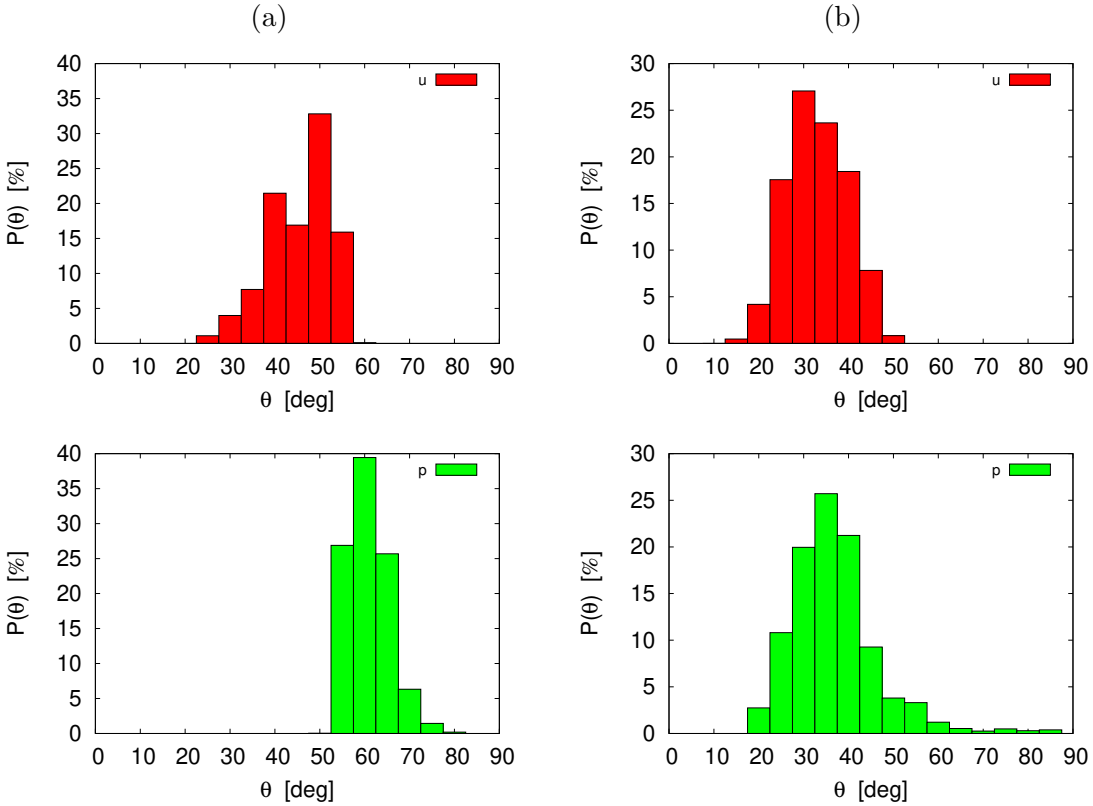

Figure 5.5: Calculated average OH polar angle distributions, $P(\theta)$, obtained from AIMD/NVT at 300 K: (a) for the fully hydroxylated (0001) surface, HS, and (b) for the fully hydroxylated (0001) surface with eight water molecules, HS+2ML. In green, θ values for the initially parallel (p) aluminols over ten trajectories are shown. Correspondingly, the average $P(\theta)$ for originally perpendicular (u) aluminols are reported in red.

The analysis of Fig.5.5 indicates that, especially for the HS model, two angular distributions, distinct but adjacent, are formed in the course of canonical dynamics. In contrast, the probability of finding an OH group in a given configuration (u or p) becomes substantially equivalent in the case of the HS+2ML model, regardless of the initial aluminols orientation.

To gain further insight into the dynamics, in particular the ability of aluminol OH groups to flip between u- and p-orientations, we look at the temporal evolution of θ-angles during the course of AIMD trajectories. This is reported in Fig.5.6, where the average OH polar angles (θ) for the twelve (for HS) and four (for HS+2ML) mentioned u and p aluminols are shown for the entire simulation time.

We note that:

- For the water-free surface (Fig.5.6(a)), at early times (*i.e.*, in the time interval around 1

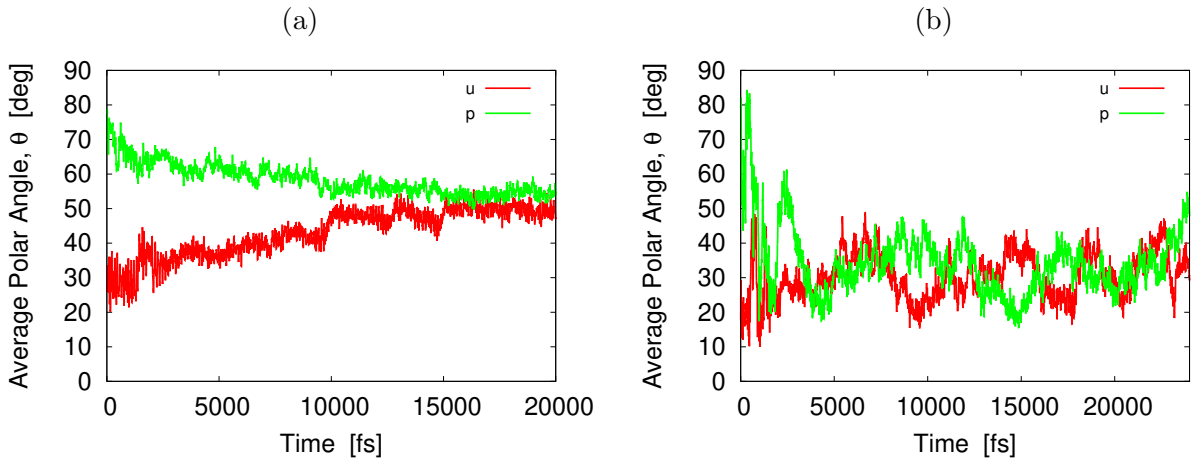

Figure 5.6: Calculated average OH polar angle curves obtained from AIMD/NVT at 300 K: (a) for the fully hydroxylated (0001) surface, HS, and (b) for the fully hydroxylated (0001) surface with eight water molecules, HS+2ML. In green, θ values for the initially parallel (p) aluminols over ten trajectories are shown. Correspondingly, the average θ for originally perpendicular (u) aluminols are reported in red.

ps), there are two distinct distributions centered around 30° and ca. 75° for the originally u (red) and p configurations (green). With time passing, both distributions approach each other, forming a single distribution at later time (10 ps ca.), centered at a value of about $\theta \sim 55°$, which is roughly the average value for u and p. This behaviour is due to rapid switching between u and p orientation which happens, as closer inspection shows [146], on a one-ps timescale. At around 15 ps or so, the memory of the aluminol OH groups of their initial u or p is completely lost.

- For the alumina surface with water, HS+2ML (Fig.5.6(b)), we note for the movable aluminol OH shown (which are not of the H-bonded type), that the distributions of originally p or u oriented OH groups are rather broad and overlapping already at early time intervals. Then, the previously p aluminol OH units drift towards the u orientation, forming a single distribution centered around 30-40°. Memory is lost on a similar timescale as for HS.

In conclusion we see that (i) u and p aluminols flip between each other (except the H-bonded aluminols of HS+2ML) on a ps-timescale; (ii) memory of the initial distributions of movable θ angles of aluminol OH bonds is lost after $\sim$ 15 ps; (iii) there are differences between HS and HS+2ML: for HS+2ML, the long-time behaviour of the movable aluminol OH bonds is biased towards the u configuration. (Also, the initially u or p OH bonds with H-bonds to water molecules on top, stay in their starting configurations.)

6 Vibrational Energy Relaxation of Interfacial OH on a Hydroxylated, Water-Covered α-Al_2O_3(0001) Surface

Available energy is energy which we can direct into any desired channel. Dissipated energy is energy which we cannot lay hold of and direct at pleasure, such as the energy of the confused agitation of molecules which we call heat.

James Clerk Maxwell

6.1 Time-resolved VSF spectroscopy of water on α-Al_2O_3

In this part of the work, theory is directed towards the simulation and description of vibrational energy relaxation of an excited OH chromophore at the water / α-alumina interface. The motivation for this investigation arises from experiments done by the group of R. K. Campen at FHI in Berlin to unravel dynamical aspects of a water-covered α-Al_2O_3(0001) surface under various conditions. The idea has been to employ VSF spectroscopy (previously described only in a "static" manner) in the time-resolved regime. In fact, temporally resolved Sum Frequency generation techniques allow to grasp details about the (vibrational) dynamics of adsorbates upon illumination *via* ultrafast laser pulses [151–154].

In the experiments, VSF spectra were done in a pump-probe fashion, enabling to follow the (ultra)fast evolution of a vibrational mode after excitation. Specifically, time-resolved *ssp*-polarized VSF was done with a pump infrared laser with a center frequency of 3710 cm^{-1}, and vibrational population dynamics from the vibrationally excited state to ground state was monitored in time. Decay of this population of its original value, and an exponential fit, defines a lifetime, τ. Depending on the different experimental setups, the α-Al_2O_3(0001) surface was prepared with either very low water coverages (*i.e.*, an air/alumina interface), or with medium to high water coverages up to liquid H_2O. In the air/surface case, isotopic substitution with deuterated water was also employed, or the surface was moderately heated. By these procedures, mostly the adsorbed water is probably affected (by isotopic substitution or desorption), and thus, indirectly, also the surface O-H bonds ("aluminols", see below), and their vibrational lifetimes. In Table 6.1, measured lifetimes are summarized.

The following is observed:

- Vibrational lifetimes are in the order 3-7 ps depending on conditions, with error bars around 1 ps.
- The O-H lifetimes without surface heating are in the order of 3 ps, and only weakly dependent on water coverage.

experimental setup	vibrational lifetime, τ [ps]
surface / air, RT	3.5 ± 0.6
surface / liquid H_2O, RT	3.3 ± 1.1
surface / air, after surface heating	6.2 ± 0.8
surface / air, after D_2O exchange, RT	7.2 ± 0.7

Table 6.1: Vibrational lifetimes τ obtained by time-resolved VSF experiments performed by the group of R.K. Campen (FHI Berlin), using an α-Al_2O_3(0001) surface sample exposed to water in different experimental conditions. RT denotes room temperature.

- After the surface has been heated, the O-H vibrational lifetime is increased.
- Deuterating the system, leads also to an increase of lifetimes, to about 7 ps.

Vibrational lifetimes of O-H (or, generally, surface atom-H) stretching vibrations in the order of several ps are "unusual". On the one-hand-side, they can be considered as very long, if the OH bond was part of a hydrogen-bonded network, *e.g.*, a water layer: in fact, time-resolved VSF experiments for the air/water interface gave lifetimes ≤ 1 ps [150, 155]. Here the excited interfacial OH relaxes efficiently thanks to direct coupling with H_2O bending overtone, which then allows further relaxation into the hydrogen bonding modes. If, on the other hand, an isolated O-H stretch mode, say, was directly coupled to surface phonons only, then much longer lifetimes than several ps are expected. In this case the high-frequency O-H mode ($\sim$ 3700 cm^{-1}) can only relax *via* multi-phonon relaxation, because the Debye frequency of the surface is much lower. For α-alumina, the Debye frequency is in the order of 1000 cm^{-1}, so three to four phonons would be required for relaxation at least. Multi-phonon relaxation is indeed a slow process: An extreme example of a long lifetime for a high-frequency adsorbate mode due to multi-phonon relaxation, is the C-O stretch mode of carbon monoxide on NaCl(100) with $\tau \sim 4$ ms [156]. Another example, chemically closer to α-alumina is represented by the O-H stretching relaxation of interfacial silanols in silica: early time-resolved vibrational spectroscopy measurements [157, 158] indicated a lifetime in the order of 100 ps, much longer than the ones obtained for this system.

For H_2O/α-Al_2O_3(0001), the experimentalists hypothesized that the excited bond is an *interfacial* O-H bond, or aluminol, of the hydroxylated alumina surface which forms when the α-Al_2O_3(0001) surface is exposed to water (see below). To explain a lifetime of several ps, the aluminol should not be directly involved in a H-bonded network, *e.g.*, (an) adsorbed water layer(s). This mode should also not be coupled to low-frequency substrate phonons only. Instead, some intermediate situation should be in operation, *i.e.*, the aluminol should at least weakly be coupled to other modes with higher frequencies, *e.g.*, those of a water layer. Still, the aluminol in question would behave as a "quasi-free" hydroxyl group [121]. The anticipated, prominent excitation of these quasi-free surface aluminols fits also nicely to measured and computed vibrational frequencies which match the chosen IR frequencies of the pump IR laser, in contrast to, *e.g.*, water hydroxyl groups (see below). The adsorbed water, weakly coupled to the excited aluminol, is affected by temperature and deuteration, both most probably decreasing the coupling strength (due to water desorption and frequency mismatch, respectively). This, in turn, should lead to longer lifetimes as observed in experiment.

In this subproject our aim is, on the basis of non-equilibrium Ab Initio Molecular Dynamics (AIMD) simulations, to (i) rationalize the several-ps lifetime of surface aluminols in H_2O/α-$Al_2O_3(0001)$, and (ii) to better understand the vibrational relaxation mechanism and energy flow in this system.

6.2 Computational models and their realization

6.2.1 Details of surface slab model

As the pump-probe VSF experiments were conducted by taking an α-$Al_2O_3(0001)$ surface sample and exposing it to air or to liquid water at room temperature, we employed a surface model that roughly represents α-alumina at low / medium water coverage. The model is the same as used in Ref. [2] for the interpretation of vibrational spectra of water-covered α-alumina(0001), which we described in Chapter 5. It consists of a hydroxylated alumina surface which forms from the so-called Al-terminated, UHV-stable (0001) surface [11, 100, 119, 120]. The HS is then covered by a few intact H_2O molecules, namely eight when considering a 2×2 cell, leading to the so-called "HS+2ML" structure. This was found to be particularly stable by DFT / PBE+D2 calculations (adsorption energy of -0.83 eV *per* water molecule), due to the formation of a honeycomb-like layer network consisting of water hexagons [2]. Specifically, the formation of hydrogen bonds between aluminol OH groups and molecular H_2O becomes possible.
In the HS+2ML model (b) of Fig.5.1, four of the twelve aluminol OH groups are non-hydrogen bonded ("quasi-free"), while eight are involved in H-bonds. This distinction is based mostly on a structural basis, due to the mismatch between the number of adsorbed H_2O molecules and the aluminols groups beneath. The relative rigidity of the water layer makes this distinction between hb- and nhb-aluminols completely valid throughout all the course of AIMD trajectories. As already described above, the quasi-free aluminols can come in "upright" and more "parallel" orientations (relative to the surface), rapidly switching between both orientations at room temperature according to AIMD simulations (see Ref. [2], Chapter 5 and Appendix below).

6.2.2 Vibrational analysis from static DFT and AIMD calculations

The HS+2ML has been taken as ideal candidate to further describe the vibrational response of water on α-alumina, yet in the time-resolved regime. The characterization of vibrational modes and frequencies is based on the work reported in Chapter 5, where we largely employed DFT calculations at the PBE+D2 level of theory, both with the static (NMA) and dynamic (AIMD) approaches. In particular, the analysis obtained from canonical (NVT) trajectories at 300 K and using time-correlation functions methods [2, 61], yielded the following observations. Calculated vibrational spectra for OH groups belonging either to surface aluminols or to molecular from adsorbed water layer indicate that:

- parallel aluminols show vibrational frequencies around 3600 cm^{-1} if not involved in accepting hydrogen bonds from nearby water molecules;
- non-hydrogen bonded upright aluminols have higher vibrational frequencies, in the range of 3750-3760 cm^{-1};
- hydrogen-bonded aluminol OH and water-OH groups are both red-shifted with respect to the quasi-free OH groups, to a range between 3000-3500 cm^{-1};
- water bending modes are found around 1600-1660 cm^{-1};

- below $\sim$ 1100 cm^{-1}, one finds H_2O librational modes, aluminol OH bending, substrate phonons and water layer vibrations, respectively.

We shall refer to these frequencies later. These observations are corroborated by experimental VSF spectra [110,146]. At an IR excitation frequency of around 3700 cm^{-1}, we therefore expect that mainly the quasi-free aluminol OH groups are excited. Further, due to selection rules for IR light polarized perpendicular to the surface, notably the "upright" non-hydrogen bonded OH bonds should be excitable.

6.2.3 AIMD calculations after vibrational excitation by "velocity swapping"

In order to model the IR preexcitation and subsequent relaxation, measured by time-resolved VSF, we employ a combination of equilibrium and non-equilibrium AIMD methods. Specifically, a protocol illustrated in Fig.6.1 is followed, consisting of the following steps:

(1) *Starting geometry and equilibration phase:* A geometry optimization at the PBE+D2 level of theory is done for the initial HS+2ML structure. From there, five canonical NVT/AIMD trajectories at 300 K are run, each 24 ps long.

(2) *Post-equilibration phase:* Starting from the end points of phase (1), five microcanonical NVE/AIMD trajectories are run, first for 10 ps, then for another 10 ps. The post-equilibration phase is introduced to remove spurious effects caused by coupling with the thermostat. The two different end times of phase (2) are used to test the influence of the length of the post-equlibration phase. We will loosely refer to phase (2) also as the "equilibrium NVE" phase.

(3) *IR excitation by "velocity swapping", subsequent non-equilibrium dynamics:* The two end times of phase (2) (10 ps and 20 ps after equilibration phase (1)), are used as starting times for two sets of non-equilibrium AIMD simulations after "IR excitation" (NEQ_1, NEQ_2), called also "non-equilibrium NVE" in what follows. Both for NEQ_1 and NEQ_2, five NVE / AIMD trajectories are run after "swapping" of nuclear velocities of specific O-H bonds, all 10 ps long.

(4) *Analysis:* Data are analyzed for energy relaxation.

Overall, in total 370 ps of DFT-based AIMD simulations have been run, 120 ps for phase (1) (5×24), 150 ps for phase (2) ($5 \times (20 + 10)$), and 100 ps for phase (3) ($(5 + 5) \times 10$).

Let us specify stage (3) of the scheme in Fig.6.1, where atom velocities of selected O-H bonds associated with interfacial aluminols are "swapped" [159]. This step is used to mimic the experimental IR excitation in the pump-probe scheme. The interaction of a single vibrational chromophore with IR light involves the absorption of a vibrational quantum of energy, $\hbar\omega_{10}$ (here we refer only to the excitation between vibrational ground and first excited states, $0 \rightarrow 1$). In our AIMD scheme, this excess energy is assumed to be fully converted into kinetic energy of atoms involved in excited aluminols. In this way, swapping of atom velocities enables us to perform *non-equilibrium* simulations, without the need of more complex techniques (*e.g.*, explicit coupling to an IR pulse).
The "kinetic energy-only model" used here does not include any atom displacements initially, along (unknown) vibrational coordinates. Of course, the excess energy stored in the O-H bonds at the beginning of phase (3), will rapidly and periodically be transferred into potential energy,

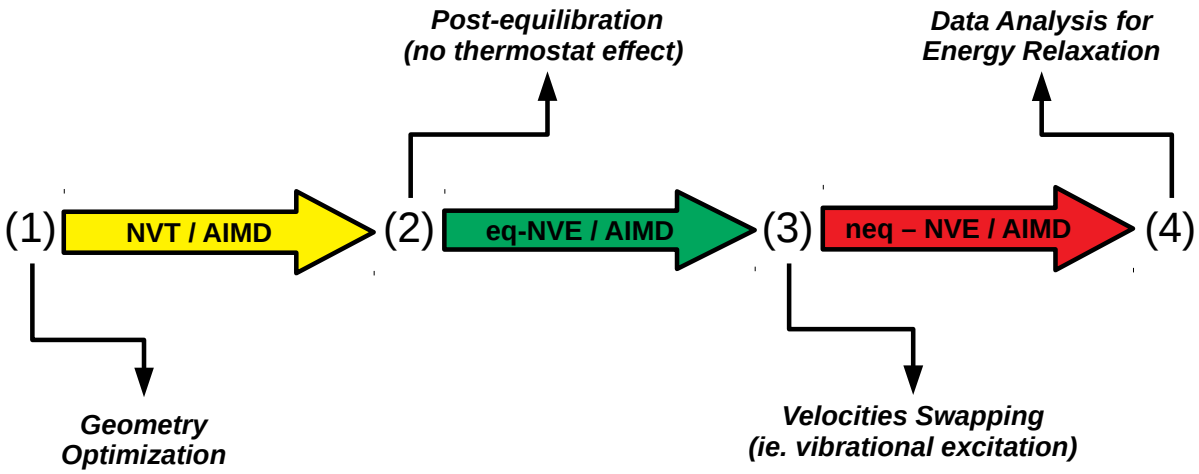

Figure 6.1: Schematic representation of non-equilibrium AIMD protocol: In phase (1), first the initial HS+2ML structure is optimized at the PBE+D2 level of theory. Then, canonical *ab initio* molecular dynamics (NVT / AIMD) trajectories at 300 K are propagated until thermal equilibrium is reached after 24 ps. At (2), AIMD trajectories are further propagated within the microcanonical ensemble to remove any spurious effect caused by coupling with the thermostat. This phase results in a "post-equilibration". After a certain time (10 ps for NEQ_1 and 20 ps for NEQ_2), nuclear velocities of specific O-H bonds are changed, at the beginning of phase (3). Then, a "non-equilibrium" phase begins during the course of which excited O-H kinetic energies are monitored, for 10 ps. Finally, in step (4) data are analyzed to unravel details of the vibrational relaxation process.

and then be redistributed into other modes. Also important, by introducing an excess of kinetic energy along certain vibrational coordinates, we can then monitor the relaxation process and even infer a vibrational lifetime. This is achieved in the analysis of non-equilibrium trajectories in stage (4), either by looking at the OH-bond kinetic energy decay or by time-resolved vibrational spectral densities as discussed below.
For further features of the original equilibrium / non-equilibrium AIMD model, see Refs. [159–161].

The velocity swapping itself proceeds as follows. First, as an idealization we only swap velocities of H- and O-atoms associated with an excited aluminol. This is achieved by choosing, as swapped velocities $\underline{\tilde{v}}(0)$ at time $t = 0$ (the time at the end of phase (2)) [159]:

$$\underline{\tilde{v}}_H(0) = \underline{v}_H(0) + \epsilon_H \; \underline{\hat{r}}_{OH}(0) \tag{6.1}$$

$$\underline{\tilde{v}}_O(0) = \underline{v}_O(0) + \epsilon_O \; \underline{\hat{r}}_{OH}(0) \quad . \tag{6.2}$$

Here,

$$\epsilon_H = \frac{(p - p_0)}{m_H} \tag{6.3}$$

$$\epsilon_O = -\frac{(p - p_0)}{m_O} \tag{6.4}$$

$$p_0 = \mu_{OH}[\underline{v}_H(0) - \underline{v}_O(0)] \cdot \hat{\underline{r}}_{OH}(0) \tag{6.5}$$

$$p = (p_0^2 + 2\mu_{OH}\ \Delta E)^{1/2} \tag{6.6}$$

In the equations above, $\mu_{OH} = \frac{m_H m_O}{m_H + m_O}$ is the O-H bond reduced mass and $\hat{\underline{r}}_{OH}(0) = \frac{\underline{r}_{OH}(0)}{|\underline{r}_{OH}(0)|}$ the normalized OH bond vector. The excess energy is represented by ΔE and in our simulations this value is taken as $\hbar\omega_{10} = 3750$ cm^{-1} (rather than the precise experimental value of 3710 cm^{-1}), in order to account for slight deviations of computed and measured frequencies. Velocities $\underline{v}(0)$ are those prior to swapping.

Only selected aluminol OH bonds are pre-excited in our AIMD simulations. Specifically, due to IR frequency and dipole orientation issues as described above, we excite only non-hydrogen bonded "upright" aluminols. This is achieved in practice by analyzing at the end of phase (2), polar angles of all non-hydrogen-bonded aluminols. Then, if $\theta_{\mathrm{OH}} < 45^{\mathrm{o}}$ the O and H atom velocities of the considered aluminol are velocity swapped, otherwise not. According to this method, not all (four, see Fig.5.1) non-hydrogen bonded aluminols are excited at the beginning of step (3). We shall see below that on average, around three aluminols are excited in our AIMD simulations.

6.3 Results of non-equilibrium AIMD

6.3.1 Analysis of time-dependent average kinetic energies

In the following section results from the non-equilibrium AIMD trajectories are reported, concerning the evolution of excited non-hydrogen bonded aluminols from the HS+2ML system shown in Fig.5.1.

We first show in Fig.6.2(a), the total kinetic energy $E_{kin}(t) = \frac{1}{2}\sum_i^N m_i v_i^2(t)$ for phases (2) and (3), NVE simulations NEQ_1 and NEQ_2, respectively. In this figure, $t = 0$ refers now to the end of phase (1) / beginning of phase (2), and the two curves are averaged over the five trajectories in each case.[1] We note that the velocity swapping at $t = 10$ ps (for NEQ_1) and $t = 20$ ps (for NEQ_2), leads to an increase of the average kinetic energy of close to 0.7 eV in the long-time limits. In our AIMD setup, this excess energy will be (re-)distributed over all $N = 68$ movable atoms. Note that at the beginning of phase (3), at $t = 10$ or $t = 20$ ps, respectively, the kinetic energy gain is around 1.4 eV (from ~ 2.7 to ~ 4.1 eV). Given $\hbar\omega = 3750$ cm^{-1} (0.46 eV), this corresponds to the excitation of around three aluminols on average.

A more detailed analysis of the time evolution of the kinetic energy before and after velocitiy swapping is provided in Figs.6.2(b) and (c), for different subsystems of the HS+2ML model. As we can observe in panels (b) and (c), both sets of AIMD trajectories NEQ_1 and NEQ_2 are characterized by an initial, pre-excitation phase which is then perturbed by the excitation of the

[1] The two curves are on top of each other for the first 10 ps by construction.

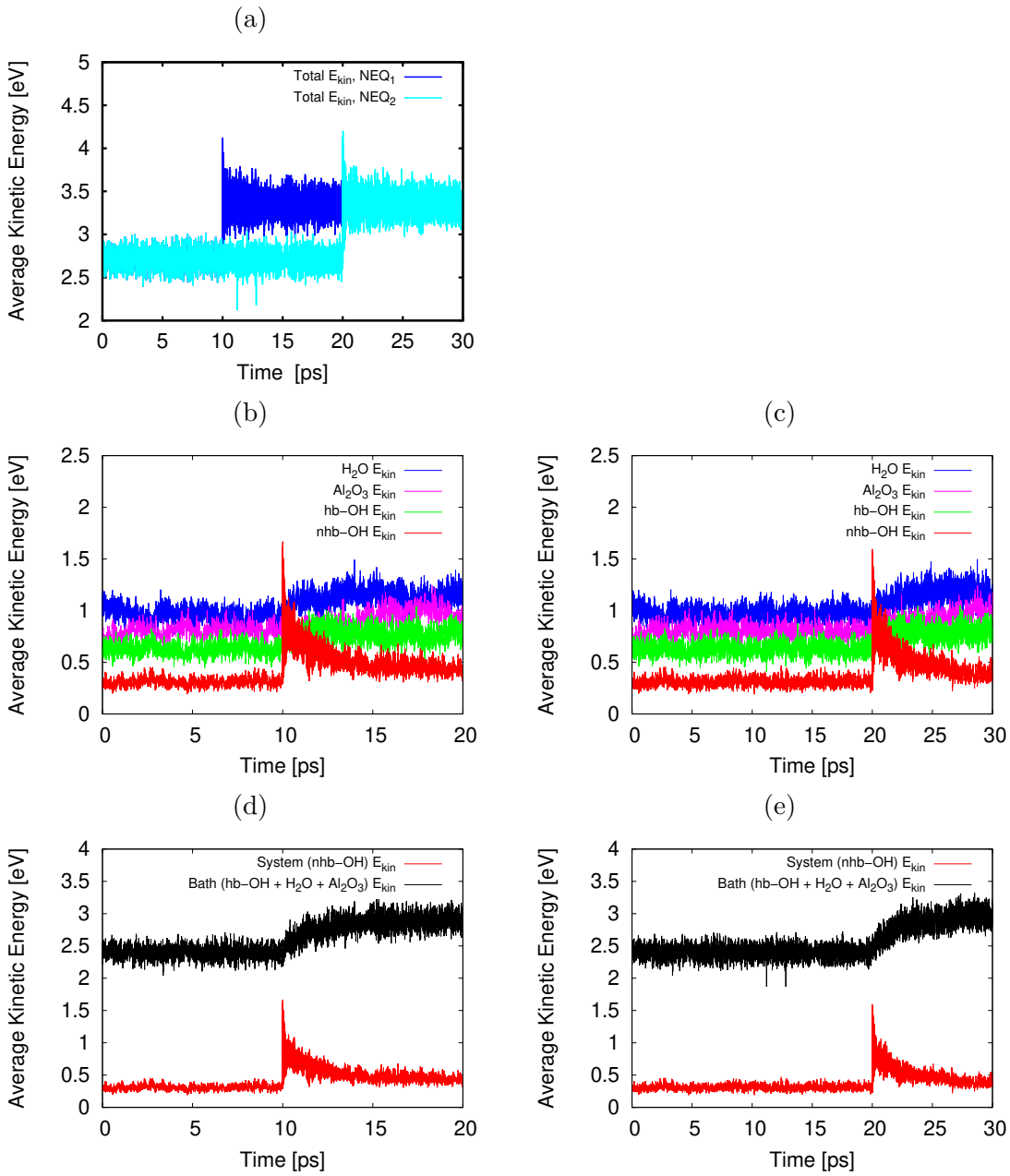

Figure 6.2: (a) Averaged (over five trajectories) kinetic energy of the total HS+2ML system, for the two sets of non-equilibrium AIMD simulations, NEQ_1 and NEQ_2. (b) Analysis of the averaged kinetic energy of different subsystems, for NEQ_1: *nhb-OH* denotes non-hydrogen bonded aluminols (excited and unexcited ones), *hb-OH* the hydrogen-bonded aluminols, and H_2O and Al_2O_3 the water layer and the surface atoms, respectively. (c) The same as (b), for NEQ_2. (d) Coarse-grained analysis of averaged kinetic energies, for NEQ_1: Kinetic energies of the "system" containing the chromophores, $E_{kin}^{sys} = E_{kin}^{nhb-OH}$, and a "bath" consisting of the rest, $E_{kin}^{bath} = E_{kin}^{hb-OH} + E_{kin}^{H_2O} + E_{kin}^{Al_2O_3}$. (e) Same as (d), for NEQ_2.

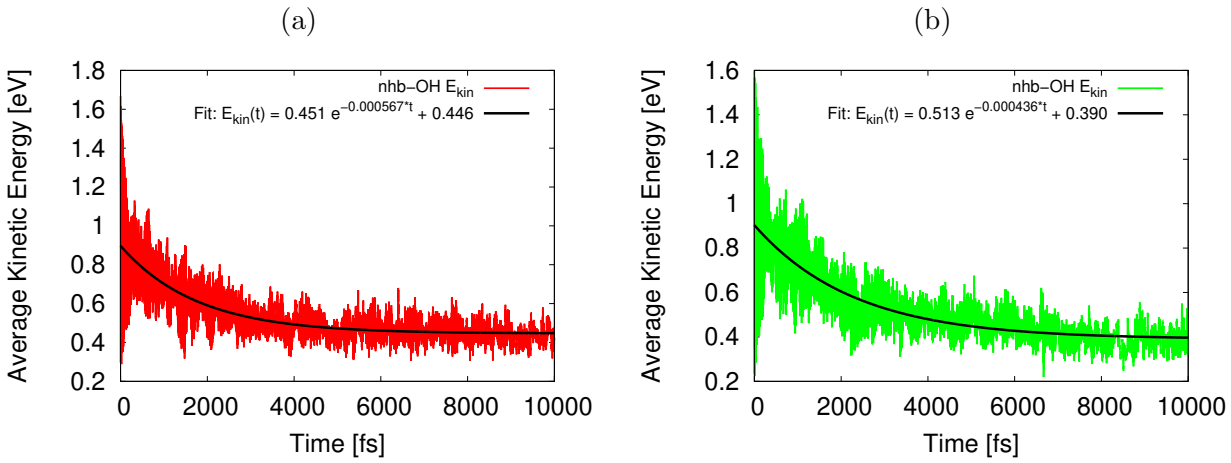

Figure 6.3: (a) Averaged kinetic energy of nhb-OH aluminols, including fitting with single exponential curve, $E_{kin}^{nhb-OH}(t)$, for NEQ_1. (b) Same plot as for NEQ_2.

selected aluminols. In particular, we report averaged E_{kin} values for four different subsystems of HS+2ML, namely:

- the four non-hydrogen bonded aluminols, among them the excited, "upright" OH bonds ("nhb-OH");
- the hydrogen-bonded aluminols ("hb-OH");
- the water molecules forming the adsorbed layer ("H_2O");
- and the remaining surface atoms ("Al_2O_3").

This simple partitioning allows already to disentangle different possible relaxation pathways. First of all we see from Figs.6.2(b) and (c), both for NEQ_1 and NEQ_2, that the average kinetic energy of non-hydrogen bonded aluminols, E_{kin}^{nhb-OH}, after the chosen post-equilibrium phase (10 ps or 20 ps, respectively) shows a sudden increase up to nearly 1.7 eV, from ca. 0.3 eV. This is close to the energy gain of above, of 1.4 eV, consistent with the average number of around three excited bonds. It is also seen that after excitation, E_{kin}^{nhb-OH} gradually decreases within the 10 ps employed to propagate the non-equilibrium trajectories, in phase (3), until the initial, excess kinetic energy is redistributed. From the other three curves in Figs.6.2(b) and (c), we note that both neighboring water molecules ($E_{kin}^{H_2O}$) and hydrogen-bonded aluminols (E_{kin}^{hb-OH}) are both effective channels for vibrational energy dissipation: the average kinetic energies of the water layer and the hb-OH bonds, increase rapidly within the first 2-3 ps after vibrational excitation of the chromphores, reaching a new, "equilibrium-like" plateau after 5 ps. In contrast, surface atoms ($E_{kin}^{Al_2O_3}$) seem to increase their kinetic energy more slowly, time-delayed (after 5-6 ps), and to a lesser extent. Of course, the contribution played by different structural domains as dissipative channels is related to the construction of our surface model. For instance, we cannot exclude *a priori* that a thicker (0001) surface model and / or a rigid surface may influence the relaxation timescale, although we believe that surface atoms contribute only marginally to the dissipation process.

A less detailed but quite instructive, more coarse-grained picture of the relaxation dynamics is provided in Figs.6.2(d) and (e), showing the kinetic energy of a "system" containing the non-

hydrogen bonded aluminols, $E_{kin}^{sys} = E_{kin}^{nhb-OH}$, and a "bath", $E_{kin}^{bath} = E_{kin}^{hb-OH} + E_{kin}^{H_2O} + E_{kin}^{Al_2O_3}$. The two graphs in Figs.6.2(d) and (e),clearly reflect a quasi-exponential decay for excited aluminols (the "system"), while the average "bath" kinetic energy follows an incremental trend which reaches a new steady-state like condition within the last picoseconds of the non-equilibrium AIMD.

Figs.6.3(a) and (b) provide a first, possible way to compute vibrational lifetimes for the O-H stretching modes. This is done by fitting the average kinetic energy of non-hydrogen bonded aluminols, E_{kin}^{nhb-OH}, for $t > t_0$, with an exponential curve:

$$E_{kin}^{nhb-OH}(t - t_0) = E_{kin}^{nhb-OH}(t_0)\ e^{-(t-t_0)/\tau} + \Delta E_{kin}^{nhb-OH} \quad . \tag{6.7}$$

Here, t_0 denotes the time of IR excitation of the chromophores. Further, τ is the relaxation time and ΔE_{kin}^{nhb-OH} represents the long-time limit of E_{kin}^{nhb-OH}. Best fits to the curves n Figs.6.3(a) and (b), give τ = 1.8 and 2.3 ps, and ΔE_{kin}^{nhb-OH} = 0.446 eV and 0.390 eV, for NEQ_1 and NEQ_2, respectively. These results are already in good qualitative agreement with experimental values, especially if we compare to the unmodified air/solid or liquid/solid interface, where in both cases vibrational lifetimes in the order of 3 ps were found. Deviations between the two sets NEQ_1 and NEQ_2 indicate some dependence on the choice of the length of the post-equilibration phase (2), fitting errors for highly oscillatory data sets, statistical errors, and the use of a single exponential, which cannot necessarily describe a multi-channel decay.

6.3.2 Analysis of time-dependent Vibrational Densities Of States (VDOS)

An alternative to the analysis of vibrational relxation based on the kinetic energy decay, perhaps less sensitive to numerical errors, is to employ so-called "instantaneous kinetic energy spectral densities" for non-equilibrium MD, as proposed in Refs. [160, 161]. These are obtained *via* Fourier transforming mass-weighted velocity-velocity autocorrelation functions (VVAFs) in individual time intervals along the AIMD trajectories. Here we use a variant of this approach by considering the Fourier transforms of non-mass weighted VVAFs, by which we obtain a Vibrational Density Of States (VDOS) as a function of both frequency ω and time t. The latter is an approximation to a time-dependent vibrational spectrum. (A similar procedure has been proposed by Lesnicki *et al* [162], but here the computed spectral densities are directly obtained by the VVAFs, in analogy to previously reported VDOS curves computed from NVT/AIMD trajectories at 300 K for both HS and HS+2ML models, see Ref. [2] and Chapter 5.) The analysis based on VDOS(ω, t) can also be done for individual atoms or various subsystems of HS+2ML. Specifically, the total VDOS(ω, t) is calculated from real parts of the Fourier transforms as

$$\text{VDOS}(\omega, t) \propto \int_{t-T}^{t} C_{vv}(\tau; t)\ \cos(\omega\tau)\ w(\tau)\ d\tau \quad . \tag{6.8}$$

Here, t indicates the time slice since the beginning of phase (3) from Fig.6.1, while T is the time interval over which the correlation function is computed at time t. We employ T = 1 ps in this work in order to balance an adequate spectral resolution with appropriate time sampling of AIMD trajectories. We also adopt a window function $w(\tau)$ for the Fourier transform, with $w(\tau) = \cos(\frac{\pi\tau}{2T})$, as reported in Eq.2.39. Further, the VVAFs $C_{vv}(\tau; t)$, which indirectly depend on time t, are computed in complete analogy to Eq.2.38 as

$$C_{vv}(\tau; t) = \frac{1}{N_t}\frac{1}{N}\sum_{i=1}^{N}\sum_{j=1}^{N_t}\langle \underline{v}_i(t_j)\underline{v}_i(t_j + \tau)\rangle \quad . \tag{6.9}$$

Here, N_t is the number of timesteps employed to sample the correlation function in the interval $[t-T,t]$ and N represents the total number of (moving) atoms. The time variable is $t_j = (j-1)\Delta t$. $\Delta t = 0.2$ fs is the spacing between two timesteps. Finally, $\langle \cdots \rangle$ denotes an ensemble average (over all trajectories). The correlation functions are therefore sampled along (non)-equilibrium trajectories to probe the spectral evolution of the excited system. In what follows, we evaluate VDOS(ω, t) during phase (3) of our AIMD trajectories, at ten snapshot times $t = 1, 2, \ldots, 10$ ps after "IR excitation" / velocity swapping.

Let us look at the time evolution of VDOS(ω, t) following the course of the non-equilibrium dynamics, as shown in Fig.6.4. From the spectral density of the total HS+2ML system, we note the very intense peak around 3600 cm^{-1} at early times of the non-equilibrium AIMD. This peak in the VDOS at $t = 1$ ps, for example, arises from the vibrationally excited non-hydrogen bonded aluminols. Its position at a lower frequency, not centered around 3750 cm^{-1} as found by NMA and room temperature AIMD in Ref. [2], can be explained by taking into account both the large anharmonicity of the O-H bond when pre-excited and the classical motion of nuclei [160,161]. In contrast, at room temperature without O-H pre-excitation, the trajectories explore predominantly the harmonic, low-energy portion of the O-H potential curve. With increasing time after pre-excitation, we see that the 3600 cm^{-1} peak looses intensity, and is being blue-shifted towards a vibrational frequency of ~ 3740 cm^{-1}. In the classical dynamics picture, the blue-shift arises from the fact that O-H vibrations loose energy and amplitude, and the corresponding trajectories then also start to probe the harmonic low-energy regions of the O-H potential curves. The ~ 3740 cm^{-1} signal is rather stable in position and intensity, after a few ps.

Appreciable modifications of VDOS curves can be also noticed for the hydrogen-bonded modes, located between 3000 and 3500 cm^{-1}, as seen in the lower panels of Fig.6.4. Further, a distinct H_2O bending-mode peak around 1600 cm^{-1} seems also to vary during the first 5 ps or so: While its position remains largely unaltered, its intensity increases somewhat. Finally, no significant spectral changes are observed for the low-frequency modes below 1100 cm^{-1}, which are associated to surface phonon and low-frequency aluminol vibrations [2]. All of these findings are qualitatively consistent with what has been found above, from kinetic energy distributions.

In order to directly address the spectral changes due to vibrational energy redistribution in time, we define the following function, ΔVDOS(t), by integrating for a given t over frequency, and referring to VDOS(0), which is the VDOS sampled within the last 1 ps of the equilibrium-NVE phase (2), *i.e.*, right *before* velocity swapping:

$$\Delta\text{VDOS}(t) = \int_0^\infty \left[\text{VDOS}(\omega, t) - \text{VDOS}(\omega, 0)\right] d\omega \quad . \tag{6.10}$$

Again, this quantity can be decomposed into atomic or subsystem contributions.

In Fig.6.5, we report the integrated VDOS curves for different time frames, *i.e.*, ΔVDOS(t) in Eq.(6.10). We employ again a constant time interval of 1 ps. The analysis is done for the total HS+2ML system, but also for subsystems. In particular, we consider hydrogen- and non-hydrogen bonded aluminols ("hb-OH" and "nhb-OH"), their sum ("Aluminols (hb-OH + nhb-OH)"), the water layer ("H_2O"), and the surface ("Al_2O_3").

Since each total VVAF is normalized for the given time interval $T = 1$ ps, the integrated total spectral density doesn't change as a function of time, so that the total ΔVDOS(t) remains con-

(a) NEQ_1, full range

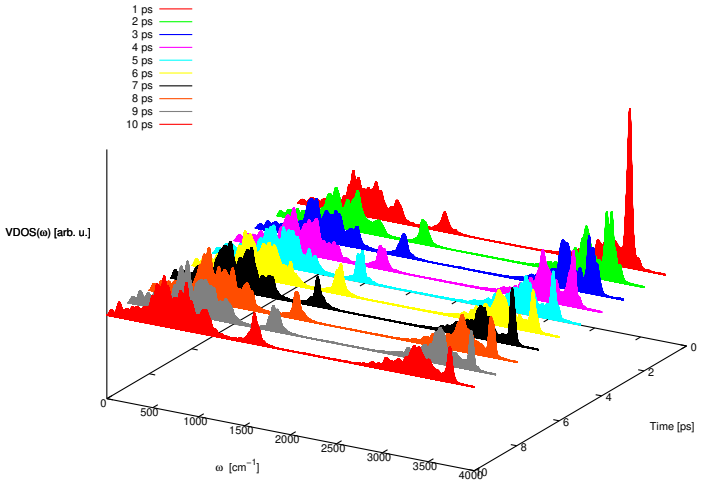

(b) NEQ_2, full range

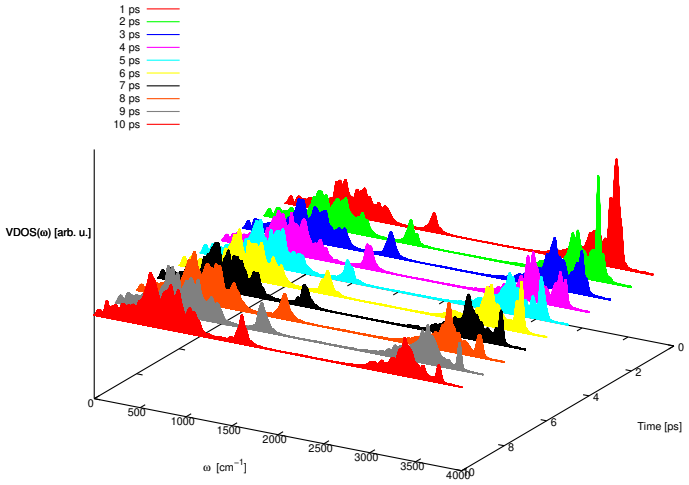

(c) NEQ_1, zoom

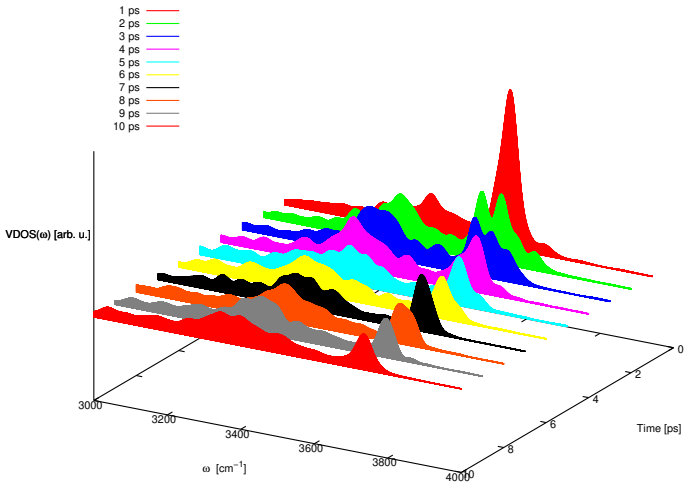

(d) NEQ_2, zoom

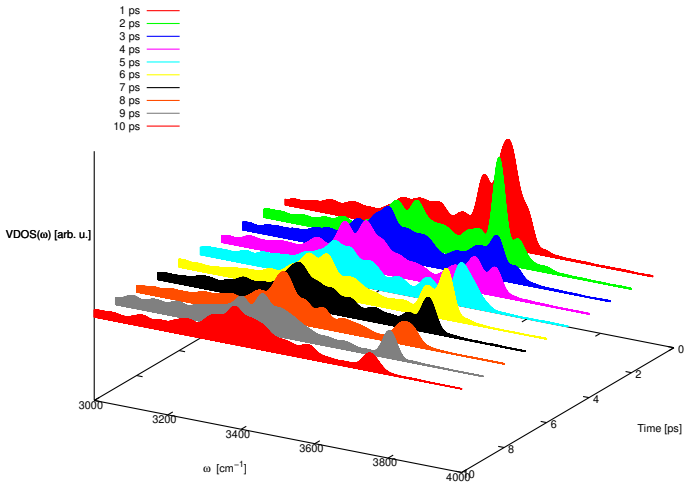

Figure 6.4: Time-evolution of the vibrational density of states, VDOS, for the total HS+2ML system in the two sets of non-equilibrium AIMD simulations, NEQ_1 ((a): full frequency range, (c): high-frequency range) and NEQ_2 ((b), (d)). Time is with respect to the beginning of phase (3), *i.e.*, after "IR excitatoon". Upper panel show full VDOS spectra, while lower panels show a closer look at O-H stretching frequencies between 3000 and 4000 cm^{-1}.

stant at 0. On the other hand, spectral densities of individual subsystems manifest significant changes during the 10 ps of propagation. The $\Delta VDOS(t)$ of non-hydrogen bonded aluminols (dark blue), suddenly increase between 0 (end of phase (2)) and 1 ps, then progressively decaying by at least 85% within the 10 ps propagation time. During the first set of trajectories, NEQ_1, the non-hydrogen bonded aluminols seem to decay at a faster rate and more uniformly than in the second set, NEQ_2, though without reaching full relaxation, *i.e.*, $\Delta VDOS(t) \to 0$.

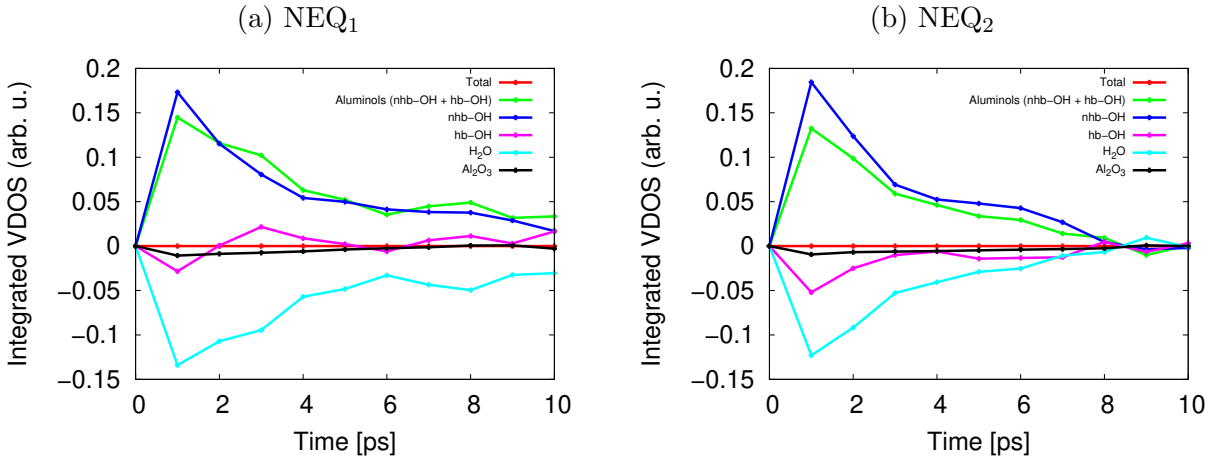

Figure 6.5: Time-evolution of the integrated VDOS curves $\Delta\text{VDOS}(t)$, for the two sets of non-equilibrium AIMD simulations, NEQ_1 (a) and NEQ_2 (b). The analysis is done for the total system, and for various subsystems.

As we would expect, the integrated spectral densities of hydrogen-bonded aluminols (in pink), water layer (in light blue) and surface atoms (in black) have an increasing behaviour within at least the very first 2 or 3 ps after 1 ps. This can be interpreted as a "vibrational population flow" into these subsystems, which are all part of the "bath". We also see that the water layer seems most affected, followed by the hydrogen-bonded aluminols and the surface, which shows only very small changes in $\Delta\text{VDOS}(t)$. While the relative inertness of the surface atoms is obvious, the relative importance of individual water molecules *vs.* hydrogen-bonded aluminols is debatable, because there are more water atoms than atoms belonging to hydrogen-bonded aluminols. At longer times, for the various bath subsystems, we see oscillatory behaviours, probably due to energy exchange within different dissipating channels.

Due to the relative inactivity of the surface atoms, the green ΔVDOS curve, which is associated with both non-hydrogen bonded and hydrogen-bonded aluminols, is close to a mirror image of the integrated spectral density of all water molecules (light blue). This reinforces the hypothesis that vibrational energy relaxation happens by coupling to modes of energy between 3000 and 3500 cm^{-1}, which are located in the hydrogen-bonded VDOS band. Further, when looking at the pink and light blue ΔVDOS curves, we also notice that spectral densities of hydrogen-bonded aluminols and water molecules evolve almost symmetrically, which may indicate an efficient energy exchange between these two, strongly hydrogen-bonded subsystems.

Overall, by inspection of Fig.6.5, we could also deduce that the main relaxation happens within the first 4 ps or so, and shows signatures of non-exponential behaviour.

Appendix: Orientational behaviour of surface aluminols

As pointed out previously while describing the non-equilibrium AIMD procedure and, specifically, the approach to select only non-hydrogen-bonded aluminols in an "upright" configuration, the orientational dynamics of surface OH groups is crucial to get further insights on the VSF experiments. In Ref. [2] and Chapter 5 it was already described how aluminols can be found

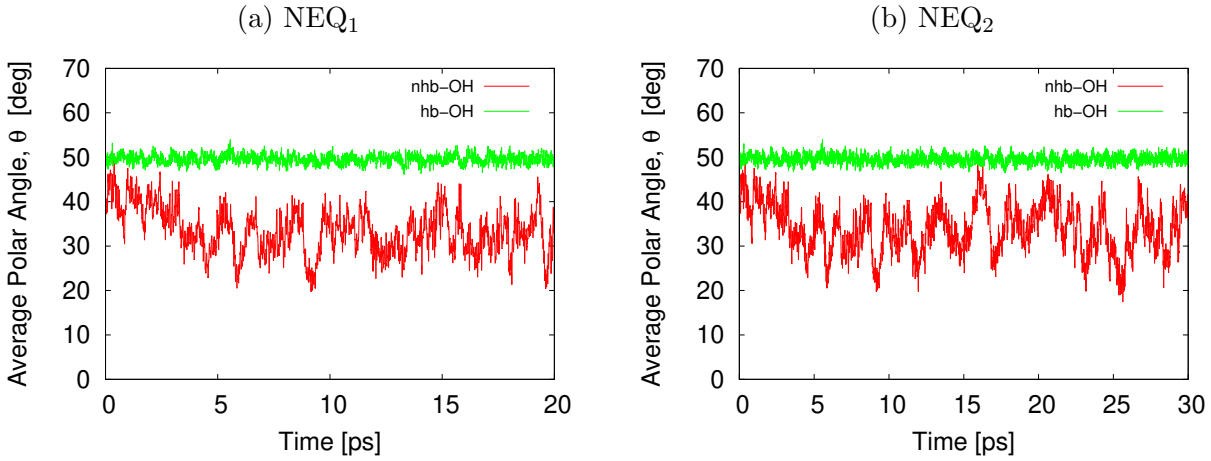

Figure 6.6: Time-evolution of average OH polar angle, θ_{OH}, for non-hydrogen bonded (red) and hydrogen-bonded aluminols (green), for the two sets of non-equilibrium AIMD simulations, NEQ_1 (a) and NEQ_2 (b).

in two main orientations with respect to the surface plane, either "upright" or "parallel". Each OH bond can flip from one configuration to another at room temperature as observed in NVT / AIMD trajectories. In the fully hydroxylated surface (without additional water layer) the $u \rightleftharpoons p$ process happens within a ps timescale. However, in the HS+2ML model considered here the presence of adsorbed water layer creates additional constraints. In fact, aluminols which form an hydrogen bonding network with overlying H_2O molecules (either H-bond donating or accepting) are now in "fixed (u or p) configurations". In total, eight are the hb-aluminols while the other four are not directly coordinated by water; these four can flip from upright to parallel orientations, yet feeling the long-range interactions with neighboring hydrogen bonds.
In Fig.6.6 we show the calculated OH polar angle ($\theta_{\mathrm{OH}} = \arccos(\frac{z_{\mathrm{OH}}}{l_{\mathrm{OH}}})$, where l_{OH} is the bond length), averaged over all thermalized NVE / AIMD trajectories (including post-equilibration and non-equilibrium phase) and over all eight hb-aluminols (in green) or all four nhb-aluminols (in red). As it can be immediately seen by looking at the θ_{OH}(t) curves, hydrogen-bonded OH groups are orientationally fixed, slightly vibrating around their equilibrium configurations (the mean 50° value must be understood as an average between the four hb-upright and the four hb-parallel aluminols, whose θ values lie around 10-20° and 80-90°, respectively). On the other hand, nhb-aluminols can orientate almost freely as represented by the fluctuating red plots.

Conclusions

The best that most of us can hope to achieve in physics is simply to misunderstand at a deeper level.

Wolfgang Pauli

In this doctoral project we have studied the adsorption of water on the α-Al_2O_3(0001) surface by considering various coverages and atomistic models, representing structures relatable to different conditions, from the gas / solid up to the liquid / solid interface. Because of the strong collaboration with experimental partners from the Interfacial Molecular Spectroscopy group (FHI, Berlin) and their expertise in surface-science techniques such as Vibrational Sum Frequency (VSF) generation, our focus has been devoted to address the vibrational modes of adsorbates belonging to the H_2O / α-alumina system.

Methodologically, this has been achieved by combination of periodic Density Functional Theory (DFT) calculations together with classical nuclear trajectories within the framework of *Ab Initio* Molecular Dynamics (AIMD). In particular, the calculation of vibrational frequencies has been reached following two different paths: a "static" one based on harmonic Normal Modes Analysis (NMA) and a "dynamic" one, the latter centered around the use of classical time-correlation functions. Specifically, anharmonic Vibrational Densities Of States (VDOS) as well as IR and VSF spectra have been obtained from AIMD trajectories at finite temperature employing an efficiently parametrized velocity-velocity correlation functions approach [61].

The approach has been applied to study water adsorption at low coverages on the UHV-stable Al-terminated α-Al_2O_3(0001) surface, using a 1/4 coverage model (one deuterated water, D_2O, molecule per (2×2) cell). We have considered three dissociated D_2O structures, 1-2, 1-4, and 1-4'. These had been suggested as particularly stable dissociation products of water at low coverage on the mentioned surface [9, 10, 12, 128]. To allow for higher coverage, also closely related, 1/2 coverage models (two D_2O molecules per (2×2) cell) were studied.

Focusing primarily on the singly dissociated forms, we found static vibrational frequencies at the DFT/PBE+D2 level of theory provide in good agreement with experimental findings, as far as frequency spacings between various "OD surface" and "OD adsorbate" species are concerned. Quantitatively, however, there is a constant ($\sim$ 100 cm^{-1}) red-shift of harmonic PBE+D2 frequencies in agreement with Refs. [12,130]. Employing appropriate scaling factors for vibrational frequencies [131] improves the agreement considerably, bringing theoretical frequencies up to 20-35 cm^{-1} close to experiment. Introducing dynamical effects and anharmonicity through AIMD at 300 K, on the other hand, the vibrational frequencies are (further) red-shifted by $\sim 10 - 40$ cm^{-1}, making the agreement between experiment and theory worse again. We also find that the anharmonic corrections are considerably smaller in classical AIMD compared to a quantum mechanical treatment, because only low-energy parts of the potential energy surface are probed in classical mechanics. In Ref. [130] it has been shown that the use of higher level electronic

structure methods can lead to vibrational frequencies in better agreement with experimental values already without scaling, and in even better agreement with scaling. Still, all theoretical frequencies appear to be red-shifted with respect to suggested experimental values, when the ideal surface models used here are adopted. In particular, no very high frequencies close to 2900 cm^{-1} suggested by experiment [12], have been found in theory by NMA and simple anharmonic corrections to it. Interestingly, such high frequencies do show up already in unscaled AIMD, when looking at spectroscopic signals, *e.g.*, x and y-polarized IR spectra (*cf.* Fig.4.7). We cannot claim here with certainty that the unusual, high-frequency peaks proposed in Ref. [12] are fully confirmed by theory, however, our work shows that dynamics, in particular when probing regions of the potential surface outside the directions of normal modes, can lead to unusual peak positions. In concert with findings made in Ref. [130], that the frequencies are considerably higher when hybrid functionals are used instead of GGA functionals as here, it seems fair to say that the occurrence of high-frequency signals (around 2900 cm^{-1}) in vibrational spectra of D_2O/α-$Al_2O_3(0001)$ is not unrealistic.

Another effect of thermal motion is line broadening. Comparing experimental linewidths for VSF signals as suggested in Ref. [12] to the theoretical linewidths computed here by AIMD, shows that at least for the "OD surface" species good agreement ($2\Gamma \sim 20\,cm^{-1}$). The linewidths of the "OD adsorbate" species seem to be underestimated somewhat, by a factor of about two. The reasons are unknown so far, however, we note again that classical AIMD probes the bottom of a potential well only, where vibrations are of low amplitude. In general, contributions by quantum mechanical treatment of nuclei to the broadening are absent. Therefore, a narrower distribution can be expected in AIMD.

While theoretical peak positions and linewidths are in reasonably good agreement with experimental observations, only poor agreement concerning line intensities in VSF spectra was found. For example, the relatively high intensity of VSF signals of 1-4 and 1-4' in experiment are surprising, given that the latter are minor species at least under thermal equilibrium conditions, and given the fact that our calculations suggest intense peaks in particular for OD^{1-2}_{surf}.

Using simple periodic models with higher coverage (1/2), we have seen, however, that VSF intensities depend very sensitively on coverage. This suggests that the ideal, perfect 1/4 coverage surface models may not be fully realistic. Rather, the presence of defects (experimentally in the process of surface preparation and / or in theory in the course of long-time thermalization), local water clustering, and, generally, the trapping of non-equilibrium configurations over long time periods after molecular beam dosing, may have a pronounced effect on measured spectra.

Furthermore, in order to explore the behaviour of H_2O on α-alumina in environmental conditions, we have considered a reconstructed, fully hydroxylated α-$Al_2O_3(0001)$ surface (HS), and of a model system of the same surface with a layer of water molecules (HS+2ML). These should serve as model systems of water-covered aluminum oxide structures and act as templates for further investigations on the solid / liquid interface. As for the first example, the main focus has been spent on the calculation of OH-vibrations, starting from NMA frequencies up to VDOS, IR and VSF spectroscopic responses from AIMD trajectories at 300 K.

Among our main results we could provide an assignment of modes for the hydroxylated alumina surface with and without water. For the OH stretching region, clear assignments could be made for OH vibrations of aluminols (which are either oriented parallel or perpendicular to

the surface, and hydrogen- or non-hydrogen bonded to water), and water-OH stretching vibrations. In particular the highest frequencies around 3700 cm^{-1} are dominated by non-hydrogen bonded, perpendicular (u) aluminol OH groups. Water adsorption creates new features, notably in ranges below 3500 cm^{-1} where hydrogen-bonded OH stretches (of both aluminal and water OH) and vibrations of the water layer are situated. The hydroxylated alumina surface, with and without water, appears to be a highly dynamical object at ambient temperatures: in particular, aluminol OH bonds rapidly flip back and forth between u and p orientations. Dynamics has a large influence on vibrational spectra. Main features of measured VSF spectra for alumina/air and alumina/(bulk) water interfaces are quite consistent with our low-coverage calculations, showing that water molecules closest to the surface are decisive for spectroscopy.

We would like to remark the persistance of such high-frequency peaks associated with non-hydrogen bonded perpendicular aluminol OH groups for both HS and HS+2ML surface models within our comparative spectral simulations. These results allow a direct comparison with previous theoretical studies done for the solid/(bulk) liquid interface, where the assignement of such modes located at $\sim$ 3700 cm^{-1} involved a different interpretation. In fact, the simple surface models we adopted for hydroxylated α-alumina clearly suggest us that high-frequency modes between 3700 and 3800 cm^{-1} can only be due to aluminol vibrations which are structurally decoupled from hydrogen bond networks, *i.e.* from the water layer. These observations are also tested and corroborated by comparison with experimental studies.

While the reasonable, semi-quantitative agreement between theoretical and experimental VSF spectra is gratifying, especially concerning the identification of high-frequency OH stretching modes within our approach, it is also clear that the current work can be improved in many ways. The methodology presented here offers a route to do so. Possible improvements have to do first of all with the model itself: the HS+2ML model system is not still not a good representative of a real, water-covered surface in particular at finite pH. Apart from issues related to computational effort, there is no principle restriction of the present methodology to go to larger, more realistic models, which have already been the subject of previous AIMD simulations [121, 122, 125]. When comparing to experiment, also a proper averaging over various elements of the second-order susceptibility tensor should be done [146] – a task which was beyond the purpose of this work. In this context also systems with very low water coverage which were the objects of experimental VSF measurements [12,146], are valuable targets for theory. On the other end of applications, the introduction of electrolytes and ions in (bulk) water are of interest.

Eventually, the collaboration with experimental partners brought us on even more challenging grounds from a simulation point of view. To address the dynamical behaviour of adsorbed water on the hydroxylated surface, pump-probe VSF experiments have been conducted, yielding curious results for the O-H stretching relaxation lifetimes. Indeed, in the experiments, vibrational energy relaxation occurred on a timescale of a few picoseconds. We decided to tackle this problem, employing and implementing a non-equilibrium AIMD scheme that would allow to mimic the IR excitation and then to follow the energy dissipation of selected OH bonds. We took the HS+2ML model to simulate a water-covered α-Al_2O_3(0001) surface as close as possible to experimental conditions.

The analysis of both kinetic energy and vibrational spectral densities provides qualitative and in part quantitative tools to unravel the energy redistribution of excited upright non-hydrogen bonded aluminols, which were in the focus of this part of the work. The latter subsystem of the

HS+2ML surface is also spectroscopically unique, with a vibrational band located between 3700 and 3800 cm^{-1}, outside the other high-frequency bands which are associated with hydrogen-bonded modes. The analysis of non-equilibrium AIMD trajectories suggests that, once the non-hydrogen bonded, upright aluminols are excited, they relax rapidly within the first picoseconds of propagation. Relaxation times obtained either *via* an exponential fit of their average kinetic energy, or by looking at the time-evolution of the frequency-integrated spectral densities, both suggest a "lifetime" between 2 and 4 ps. This is in good agreement with experimental measurements. More importantly, the tools we adopted also allow us to disentangle the role of various other subsystems of the HS+2ML model for the relaxation process. Indeed, we can identify as main dissipative channels both hydrogen-bonded aluminols and, in their sum even more important, water molecules in the adsorbed water layer. In general, hydrogen-bonded modes with frequencies between 3000 and 3500 cm^{-1} act as efficient pathways for the redistribution of the initial excess of kinetic energy in quasi-free, high-frequency O-H aluminols.

In summary, the study of vibrational spectroscopy and dynamics of water on α-alumina continues to be an interesting and challenging subject for both theory and experiment. Our endeavour has hopefully contributed to shed more light on this topic.

Acknowledgments

I have been dreaming about the doctorate since I was 16 years-old. Already at that time, I was almost certain I would have done it abroad, eager to learn, to make new experiences and to live in a different environment. Yet, some years later, I would have never imagined to be in Potsdam and to actually reach this important personal achievement.
These last four years have been enormously significant for my scientific, academic but also personal development. Working and living abroad, driven by the dream of pursuing a scientific career, has not been easy at all. It forced me to adopt new perspectives, to question my previous beliefs and my alleged abilities, to constantly confront my ideas with those of others, eventually shaping my character in ways that will resonate for the years ahead. The time spent for my doctorate strongly influenced my connections to other people as well, either sacrificing some of the strongest relationships I had or building up new friendships and collaborations for the future.

Not only I would have never been able to accomplish most of the results of this work, but I certainly wouldn't have overcome many of the difficulties I faced, nor I would have appreciated the great moments I have encountered during my life as doctoral student, without the help and the presence of many people, to whom goes my deepest gratitude.

First, I need to thank my supervisor, or *doktorvater*, Prof. Dr. Peter Saalfrank for giving me the opportunity to join the Theoretical Chemistry group back in 2015, for always supporting me and for never giving up on guiding and trusting this clumsy, messy and (too much) talkative Italian student. I will be forever in dept with him for his lessons (academic and not) for the rest of my career. I need to sincerely thank also my second supervisor, Prof. Dr. Beate Paulus, for the important feedbacks about my projects and for carefully reading my thesis. Let me also express my gratitute to Prof. Dr. Marialore Sulpizi, who kindly agreed to be my external referee and for her advices. Coming back to Potsdam, many of my technical troubles would have not been solved without the endless help of PD Dr. Tillmann Klamroth, who I also want to thank for his generous willingness to teach me the most varied curiosities about German language and culture, as well as for our interesting political and philosophical discussions.

It seems obvious that in four years at the University of Potsdam, many colleagues have played a strong role on my daily working life. Among these, I certainly have to thank Dr. Foudhil Bouakline, who (although he will never admit it) has undoubtedly become a great friend, thanks to all the time spent together talking about science, politics, but also about what it means to live away from home. Another trusted colleague has been Dr. Radosław "Radek" Włodarczyk, whose help on technical issues does not even come close to the precious friendship he gave me. A huge and deep acknowledgment surely goes to my great project partner Dr. Sophia Heiden, who shared worries and excitements dealing with water on alumina and related experiments. And how to forget Dr. Pascal Krause, whose precious aesthetic skills have often corrected the appearance of my posters and presentations, but whose closeness and trust will endure for long time.
Special thanks goes to my office mates, no doubt to the past ones, but above all to the current

ones: Florian Bedurke and Eric Fischer. They have witnessed the most intense moments linked to this doctoral work, also on the personal level, they gave me a huge help in many occasions, and I will never forget our days together in room D2.17. Last but not least, I wish my master student Pierre Schwarz a flourishing career and a bright future.
Eventually, let me express my sincere gratitude and my best wishes to other (present and past) members of the TC group: Manuel, Christopher, Boyke, Jan, Ulf, Jonas, Gereon, Evgenii, Jörg, Tao, Robert (Scholz and Edler von Zander), Clemens, Steven, Tina, Hilke, Daniel, but also to the staff Galina, Kerstin and Rainer. Each of you has been very important for me while working in Potsdam and I would not be at this stage of my life without you.

During my doctorate I have also had the pleasure and honor to be a member of the International Max Planck Research School of the Fritz-Haber Institute in Berlin. I then need to thank the organizers of this school for their guidance and help, Dr. Tobias Kampfrath and Dr. Alex Paarmann, as well as the secretaries, Bettina Menzel and Ines Bressel. Thanks to the school I had the fantastic chance to organize and attend the VI IMPRS Workshop "From Models to Reality" in 2018, whose realization is certainly not due to me but to my friend and bright colleague Kristin Werner.
Collaborations and scientific exchanges have been at the heart of my doctoral project, especially thanks to the Max Planck Society. Therefore, let me thank my experimental partners, lead by Dr. R. Kramer Campen, for the stimulating discussions and the challenging work we did together, but also my collaborator from MPIP Mainz, Dr. Yuki Nagata, for his endless help while learning the "art" of spectroscopic simulations.

The life of the doctoral student, especially if abroad, as I said, certainly has a strong impact on his relationships and on the people he loves. I cannot therefore fail to thank my big (and sometimes "bulky") family, especially my parents Alberto and Maria Laura and my brother Filippo, without whose constant support and unconditional love I could never have taken this path and then continue it.
If some relationships offer the certainty of lasting over the years, regardless of the distance, others must also be accepted, appreciated and valued despite their limited duration. Indeed, their importance will resonate over time. So it has been for my beloved Cecilia, whose presence and feelings for me have deeply affected the last years together, filling them with joy and passion, travelling between Potsdam and Livorno.
Many other important people have been involved in my life as a young researcher abroad, some in Germany some that I left in Italy. Among these, my gratitude naturally goes to my intimate friends, for their closeness and emotional support, and to my mentors, such as Prof. Dr. Maurizio Persico and my science teacher Rossella Di Batte, whom I thank for having guided and routed me on the way to research.
I want to conclude this section of acknowledgments, expressing my indescribable gratitude and incommensurate affection for my beloved grandmother Ghighi, who passed away right during my doctorate. This work is dedicated to her.

La vita dello studente di dottorato, soprattutto se all'estero, come dicevo, ha sicuramente una forte impatto sulle sue relazioni e sulle persone che ama. Non posso quindi esimermi dal ringraziare la mia grande (e a volte "ingombrante") famiglia, in particolar modo i miei genitori Alberto e Maria Laura e mio fratello Filippo, senza il cui costante sostegno e l'incondizionato affetto mai avrei potuto intraprendere questo percorso e poi proseguirlo.
Se alcuni rapporti offrono la certezza di perdurare nel tempo, indipendentemente dalla distanza,

altri devono essere accettati, apprezzati e valorizzati nonostante la loro durata limitata. Infatti, la loro importanza risuonerà nel tempo. Così è stato per la mia amata Cecilia, la cui presenza e i cui sentimenti nei miei confronti hanno profondamente influenzato gli anni trascorsi insieme, riempiendoli di gioia e di passione, viaggiando tra Potsdam e Livorno.
Molte altre importanti persone sono state coinvolte nella mia vita di giovane ricercatore all'estero, alcune in Germania altre che ho lasciato in Italia. Fra queste, la mia riconoscenza va naturalmente ai miei amici, per la loro vicinanza e sostegno emotivo, e ai miei mentori, come il Prof. Dr. Maurizio Persico e la mia insegnante di scienze Rossella Di Batte, che ringrazio per avermi guidato e instradato sulla via della ricerca.
Voglio concludere questa sezione di ringraziamenti, esprimendo la mia indescrivibile riconoscenza e l'incommensurato affetto per la mia adorata nonna Ghighi, la quale è venuta a mancare proprio durante il mio dottorato. A lei è dedicato questo lavoro.

Publications

Related to this work:

1. **G. Melani**, Y. Nagata, J. Wirth, and P. Saalfrank: « Vibrational spectroscopy of hydroxylated α-Al_2O_3(0001) surfaces with and without additional water: An *ab initio* molecular dynamics study », *J. Chem. Phys.* **2018,** *149,* 014707-014717.

2. **G. Melani**, Y. Nagata, R. K. Campen, and P. Saalfrank: « Vibrational spectra of dissociatively adsorbed D_2O on Al-terminated α-Al_2O_3(0001) surfaces from *ab initio* molecular dynamics », *J. Chem. Phys.* **2019,** *150,* 244701-244716.

Other publications:

1. F. Bouakline, U. Lorenz, **G. Melani**, G. K. Paramonov, and P. Saalfrank: « Isotopic effects in vibrational relaxation dynamics of H on a Si(100) surface », *J. Chem. Phys.* **2017,** *147,* 144703-144714.

2. G. Granucci, **G. Melani**, M. Persico, and P. Van Leuven : « Energy selection in nonadiabatic transitions », *J. Phys. Chem. A* **2018,** *122,* 2, 678-689.

List of Abbreviations

AIMD *Ab Initio* Molecular Dynamics

CUS Coordinatively Unsaturated Sites

CI-NEB Climbing Image Nudged Elastic Band

DFT Density Functional Theory

D2 / D3 Grimme's dispersion corrections

GGA Generalized Gradient Approximation

GO Geometry Optimization

HF Hartree-Fock

HK Hohenberg-Kohn

HS Hydroxylated Surface

HS+2ML Hydroxylated Surface with additional water layer (2 MonoLayers)

IR Infrared

KS Kohn-Sham

LDA Local Density Approximation

LMP2 Local 2^{nd}-order Møller-Plesset Perturbation Theory

MD Molecular Dynamics

NEB Nudged Elastic Band

NMA Normal Modes Analysis

NVE Microcanonical ensemble (fixed number of particles / volume / total energy)

NVT Canonical ensemble (fixed number of particles / volume / temperature)

PAW Projector Augmented Wave

PBE Perdew-Burke-Ernzerhof functional

PW Plane Waves

SFG Sum Frequency Generation

TDSE Time-dependent Schrödinger equation

TISE Time-independent Schrödinger equation

UHV Ultra High Vacuum

VASP Vienna Ab initio Simulation Package

VDOS Vibrational Density Of States

VSF Vibrational Sum Frequency

VVAF Velocity-Velocity Autocorrelation Function

Bibliography

[1] G. Melani, Y. Nagata, R. K. Campen, and P. Saalfrank. Vibrational spectra of dissociatively adsorbed D_2O on Al-terminated α-$Al_2O_3(0001)$ surfaces from *ab initio* molecular dynamics. *J. Chem. Phys.*, 150(24):244701–244716, (2019).

[2] G. Melani, Y. Nagata, J. Wirth, and P. Saalfrank. Vibrational spectroscopy of hydroxylated α-$Al_2O_3(0001)$ surfaces with and without water: An *ab initio* molecular dynamics study. *J. Chem. Phys.*, 149(1):014707–014717, (2018).

[3] J. H. Seinfeld and S. N. Pandis. *Atmospheric Chemistry and Physics*. John Wiley and Sons, (2016).

[4] A. L. Goodman, E. T. Bernard, and V. H. Grassian. Spectroscopic study of nitric acid and water adsorption on oxide particles: Enhanced nitric acid uptake kinetics in the presence of adsorbed water. *J. Phys. Chem. A*, 105(26):6443–6457, (2001).

[5] H. A. Al-Abadleh and V. H. Grassian. FT-IR study of water adsorption on aluminum oxide surfaces. *Langmuir*, 19(2):341–347, (2003).

[6] H. A. Al-Abadleh and V. H. Grassian. Oxide surfaces as environmental interfaces. *Surf. Sci. Rep.*, 52(3):63–161, (2003).

[7] G. Rubasinghege and V. H. Grassian. Role(s) of adsorbed water in the surface chemistry of environmental interfaces. *Chem. Commun.*, 49:3071–3094, (2013).

[8] A. Abdelmonem, E. H. G. Backus, N. Hoffmann, M. A. Sánchez, J. D. Cyran, A. Kiselev, and M. Bonn. Surface-charge-induced orientation of interfacial water suppresses heterogeneous ice nucleation on α-alumina (0001). *Atmospheric Chem. Phys.*, 17(12):7827–7837, (2017).

[9] K. C. Hass, W. F. Schneider, A. Curioni, and W. Andreoni. The chemistry of water on alumina surfaces: Reaction dynamics from first principles. *Science*, 282(5387):265–268, (1998).

[10] K. C. Hass, W. F. Schneider, A. Curioni, and W. Andreoni. First-principles molecular dynamics simulations of H_2O on α-$Al_2O_3(0001)$. *J. Phys. Chem. B*, 104(23):5527–5540, (2000).

[11] T. Kurita, K. Uchida, and A. Oshiyama. Atomic and electronic structures of α-Al_2O_3 surfaces. *Phys. Rev. B*, 82(15):155319–155333, (2010).

[12] H. Kirsch, J. Wirth, Y. Tong, M. Wolf, P. Saalfrank, and R. K. Campen. Experimental characterization of unimolecular water dissociative adsorption on α-alumina. *J. Phys. Chem. C*, 118(25):13623–13630, (2014).

[13] P. Atkins and Friedman R. *Molecular Quantum Mechanics*. Oxford Universiy Press, (2010).

[14] A. Szabo and N. S. Ostlund. *Modern Quantum Chemistry*. Dover Publications, (1996).

[15] N. W. Ashcroft and N. D. Mermin. *Solid State Physics*. Cengage Learning, (1976).

[16] M. P. Allen and D. J. Tildesley. *Computer Simulation of Liquids*. Oxford University Press, (2017).

[17] W. Kohn and L. J. Sham. Self-consistent equations including exchange and correlation effects. *Phys. Rev.*, 140:1133–1138, (1965).

[18] D. M. Ceperley and B. J. Alder. Ground state of the electron gas by a stochastic method. *Phys. Rev. Lett.*, 45:566–569, (1980).

[19] J. P. Perdew and A. Zunger. Self-interaction correction to density-functional approximations for many-electron systems. *Phys. Rev. B*, 23:5048–5079, (1981).

[20] J. P. Perdew and Y. Wang. Accurate and simple analytic representation of the electron-gas correlation energy. *Phys. Rev. B*, 45:13244–13249, (1992).

[21] J. P. Perdew, K. Burke, and M. Ernzerhof. Generalized gradient approximation made simple. *Phys. Rev. Lett.*, 77(18):3865–3868, (1996).

[22] J. P. Perdew, K. Burke, and M. Ernzerhof. Generalized gradient approximation made simple [Phys. Rev. Lett. 77, 3865 (1996)]. *Phys. Rev. Lett.*, 78:1396–1396, (1997).

[23] A. D. Becke. Density-functional exchange-energy approximation with correct asymptotic behavior. *Phys. Rev. A*, 38:3098–3100, (1988).

[24] C. Lee, W. Yang, and R. G. Parr. Development of the Colle-Salvetti correlation-energy formula into a functional of the electron density. *Phys. Rev. B*, 37:785–789, (1988).

[25] A. D. Becke. A new mixing of Hartree–Fock and local density-functional theories. *J. Chem. Phys.*, 98(2):1372–1377, (1993).

[26] P. J. Stephens, F. J. Devlin, C. F. Chabalowski, and M. J. Frisch. Ab initio calculation of vibrational absorption and circular dichroism spectra using density functional force fields. *J. Phys. Chem.*, 98(45):11623–11627, (1994).

[27] C. Adamo and V. Barone. Toward reliable density functional methods without adjustable parameters: The PBE0 model. *J. Chem. Phys.*, 110(13):6158–6170, (1999).

[28] J. Heyd, G. E. Scuseria, and M. Ernzerhof. Hybrid functionals based on a screened Coulomb potential. *J. Chem. Phys.*, 118(18):8207–8215, (2003).

[29] P. E. Blöchl. Projector augmented-wave method. *Phys. Rev. B*, 50(24):17953–17979, (1994).

[30] J. Klimeš and A. Michaelides. Perspective: Advances and challenges in treating van der Waals dispersion forces in density functional theory. *J. Chem. Phys.*, 137(12):120901, 2012.

[31] S. Grimme, A. Hansen, J. G. Brandenburg, and C. Bannwarth. Dispersion-corrected mean-field electronic structure methods. *Chem. Rev.*, 116(9):5105–5154, (2016).

[32] S. Grimme. Semiempirical GGA-type density functional constructed with a long-range dispersion correction. *J. Comp. Chem.*, 27(15):1787–1799, (2006).

[33] S. Grimme, J. Antony, S. Ehrlich, and H. Krieg. A consistent and accurate ab initio parametrization of density functional dispersion correction (DFT-D) for the 94 elements H-Pu. *J. Chem. Phys.*, 132(15):154104–154123, (2010).

[34] E. Caldeweyher, C. Bannwarth, and S. Grimme. Extension of the D3 dispersion coefficient model. *J. Chem. Phys.*, 147(3):034112–034119, (2017).

[35] D. Marx and J. Hutter. *Ab Initio Molecular Dynamics*. Cambridge University Press, (2009).

[36] S. Nosé. A molecular dynamics method for simulations in the canonical ensemble. *Mol. Phys.*, 52(2):255–268, (1984).

[37] S. Nosé. A unified formulation of the constant temperature molecular dynamics methods. *J. Chem. Phys.*, 81(1):511–519, (1984).

[38] W. G. Hoover. Canonical dynamics: Equilibrium phase-space distributions. *Phys. Rev. A*, 31:1695–1697, (1985).

[39] E. Bright Wilson Jr., J. C. Decius, and P. C. Cross. *Molecular Vibrations*. Dover Publications, (1980).

[40] D. A. McQuarrie. *Statistical Mechanics*. University Science Books, (2000).

[41] A. Nitzan. *Chemical Dynamics in Condensed Phases*. Oxford University Press, (2006).

[42] M.-P. Gaigeot. Theoretical spectroscopy of floppy peptides at room temperature. A DFTMD perspective: Gas and aqueous phase. *Phys. Chem. Chem. Phys.*, 12:3336–3359, (2010).

[43] M. Thomas, M. Brehm, R. Fligg, P. Vöhringer, and B. Kirchner. Computing vibrational spectra from ab initio molecular dynamics. *Phys. Chem. Chem. Phys.*, 15:6608–6622, (2013).

[44] Y. R. Shen. *The Principles of Nonlinear Optics*. Wiley-Interscience, (2002).

[45] J. H. Hunt, P. Guyot-Sionnest, and Y. R. Shen. Observation of C-H stretch vibrations of monolayers of molecules optical sum-frequency generation. *Chem. Phys. Lett.*, 133(3):189–192, (1987).

[46] A. G. Lambert, P. B. Davies, and D. J. Neivandt. Implementing the theory of sum frequency generation vibrational spectroscopy: A tutorial review. *Appl. Spectrosc. Rev.*, 40(2):103–145, (2005).

[47] Y. R. Shen and V. Ostroverkhov. Sum-frequency vibrational spectroscopy on water interfaces: Polar orientation of water molecules at interfaces. *Chem. Rev.*, 106(4):1140–1154, (2006).

[48] C. S. Tian and Y. R. Shen. Recent progress on sum-frequency spectroscopy. *Surf. Sci. Rep.*, 69(2):105–131, (2014).

[49] P. A. Covert and D. K. Hore. Geochemical insight from nonlinear optical studies of mineral/water interfaces. *Ann. Rev. Phys. Chem.*, 67(1):233–257, (2016).

[50] A. Morita and J. T. Hynes. A theoretical analysis of the sum frequency generation spectrum of the water surface. II. Time-dependent approach. *J. Phys. Chem. B*, 106(3):673–685, (2002).

[51] R. Kubo. The fluctuation-dissipation theorem. *Rep. Prog. Phys.*, 29(1):255–284, (1966).

[52] S. D. Ivanov, A. Witt, and D. Marx. Theoretical spectroscopy using molecular dynamics: Theory and application to CH_5^+ and its isotopologues. *Phys. Chem. Chem. Phys.*, 15:10270–10299, (2013).

[53] A. Morita and J. T. Hynes. A theoretical analysis of the sum frequency generation spectrum of the water surface. *Chem. Phys.*, 258(2):371–390, (2000).

[54] T. Ishiyama and A. Morita. Molecular dynamics study of gas/liquid aqueous sodium halide interfaces. I. Flexible and polarizable molecular modeling and interfacial properties. *J. Phys. Chem. C*, 111(2):721–737, (2007).

[55] T. Ishiyama, T. Imamura, and A. Morita. Theoretical studies of structures and vibrational sum frequency generation spectra at aqueous interfaces. *Chem. Rev.*, 114(17):8447–8470, (2014).

[56] T. Ishiyama and A. Morita. Computational analysis of vibrational sum frequency generation spectroscopy. *Ann. Rev. Phys. Chem.*, 68(1):355–377, (2017).

[57] B. J. Berne and G. D. Harp. On the calculation of time correlation functions. *Adv. Chem. Phys.*, 27:64–227, (1970).

[58] J. W. Blackman and J. W. Tukey. *Particular Pairs of Windows*, pages 98–99. Dover Publications, (1959).

[59] P. H. Berens and K. R. Wilson. Molecular dynamics and spectra. I. Diatomic rotation and vibration. *J. Chem. Phys.*, 74(9):4872–4882, (1981).

[60] A. A. Mostofi, J. R. Yates, G. Pizzi, Y.-S. Lee, I. Souza, D. Vanderbilt, and N. Marzari. An update version of *wannier90*: A tool for obtaining maximally-localised Wannier functions. *Comp. Phys. Comm.*, 185:2309–2310, (2014).

[61] T. Ohto, K. Usui, T. Hasegawa, M. Bonn, and Y. Nagata. Toward ab initio molecular dynamics modeling for sum-frequency generation spectra; an efficient algorithm based on surface-specific velocity-velocity correlation function. *J. Chem. Phys.*, 143(12):124702–124712, (2015).

[62] J. Liu, W. H. Miller, F. Paesani, W. Zhang, and D. A. Case. Quantum dynamical effects in liquid water: A semiclassical study on the diffusion and the infrared absorption spectrum. *J. Chem. Phys.*, 131(16):164509, (2009).

[63] J. L. Skinner, P. A. Pieniazek, and S. M. Gruenbaum. Vibrational spectroscopy of water at interfaces. *Acc. Chem. Res.*, 45(1):93–100, (2012).

[64] S. A. Corcelli and J. L. Skinner. Infrared and Raman line shapes of dilute HOD in liquid H_2O and D_2O from 10 to 90°C. *J. Phys. Chem. A*, 109(28):6154–6165, (2005).

[65] B. M. Auer and J. L. Skinner. IR and Raman spectra of liquid water: Theory and interpretation. *J. Chem. Phys.*, 128(22):224511–224523, (2008).

[66] S. Hosseinpour, F. Tang, F. Wang, R. A. Livingstone, S. J. Schlegel, T. Ohto, M. Bonn, Y. Nagata, and E. H. G. Backus. Chemisorbed and physisorbed water at the TiO_2/water interface. *J. Phys. Chem. Lett.*, 8:2195–2199, (2017).

[67] G. Kresse and J. Hafner. *Ab initio*, molecular dynamics for liquid metals. *Phys. Rev. B*, 47(1):558–561, (1993).

[68] G. Kresse and J. Hafner. *Ab initio*, molecular dynamics for open-shell transition metals. *Phys. Rev. B*, 48(17):13115–13118, (1993).

[69] G. Kresse and J. Hafner. Ab initio molecular-dynamics simulation of the liquid-metal–amorphous-semiconductor transition in germanium. *Phys. Rev. B*, 49:14251–14269, (1994).

[70] G. Kresse and J. Hafner. Norm-conserving and ultrasoft pseudopotentials for first-row and transition elements. *J. Phys. Condens. Matter*, 6(40):8245–8257, (1994).

[71] G. Kresse and J. Furthmüller. Efficient iterative schemes for ab initio total-energy calculations using a plane-wave basis set. *Phys. Rev. B*, 54:11169–11186, (1996).

[72] G. Kresse and J. Furthmüller. Efficiency of ab-initio total energy calculations for metals and semiconductors using a plane-wave basis set. *Comput. Mater. Sci.*, 6(1):15–50, (1996).

[73] J. Hafner. Ab-initio simulations of materials using VASP: Density-functional theory and beyond. *J. Comp. Chem.*, 29(13):2044–2078, (2008).

[74] G. Kresse and D. Joubert. From ultrasoft pseudopotentials to the projector augmented-wave method. *Phys. Rev. B*, 59:1758–1775, (1999).

[75] P. Pulay. Convergence acceleration of iterative sequences. The case of SCF iteration. *Chem. Phys. Lett.*, 73(2):393–398, 1980.

[76] H. J. Monkhorst and J. D. Pack. Special points for Brillouin-zone integrations. *Phys. Rev. B*, 13:5188–5192, (1976).

[77] H. Jónsson, Greg M., and K. W. Jacobsen. *Nudged elastic band method for finding minimum energy paths of transitions*, pages 385–404. World Scientific, (1995).

[78] G. Henkelman, B. P. Uberuaga, and H. Jónsson. A climbing image nudged elastic band method for finding saddle points and minimum energy paths. *J. Chem. Phys.*, 113(22):9901–9904, (2000).

[79] P. A. Cox V. E. Henrich. *The Surface Science of Metal Oxides.* Cambridge University Press: Cambridge, (1994).

[80] H.-J. Freund, H. Kuhlenbeck, and V. Staemmler. Oxide surfaces. *Rep. Prog. Phys.*, 59(3):283–347, (1996).

[81] G. E. Brown, V. E. Henrich, W. H. Casey, D. L. Clark, C. Eggleston, A. Felmy, D.. W. Goodman, M. Grätzel, G. Maciel, M. I. McCarthy, K. H. Nealson, D. A. Sverjensky, M. F. Toney, and J. M. Zachara. Metal oxide surfaces and their interactions with aqueous solutions and microbial organisms. *Chem. Rev.*, 99(1):77–174, (1999).

[82] M. A. Henderson. The interaction of water with solid surfaces: Fundamental aspects revisited. *Surf. Sci. Rep.*, 46:1–308, (2002).

[83] P. A. Thiel and T. E. Madey. The interaction of water with solid surfaces: Fundamental aspects. *Surf. Sci. Rep.*, 7(6):211–385, (1987).

[84] M. Causà, R. Dovesi, C. Pisani, and C. Roetti. Ab initio characterization of the (0001) and (1010) crystal faces of α-alumina. *Surf. Sci.*, 215(1):259–271, (1989).

[85] I. Manassidis, A. De Vita, and M. J. Gillan. Structure of the (0001) surface of α-Al_2O_3 from first principles calculations. *Surf. Sci. Lett.*, 285(3):517–521, (1993).

[86] T. J. Godin and J. P. LaFemina. Atomic and electronic structure of the corundum (α-alumina) (0001) surface. *Phys. Rev. B*, 49:7691–7696, (1994).

[87] V. E. Puchin, J. D. Gale, A. L. Shluger, E. A. Kotomin, J. Günster, M. Brause, and V. Kempter. Atomic and electronic structure of the corundum (0001) surface: Comparison with surface spectroscopies. *Surf. Sci.*, 370(2):190–200, (1997).

[88] J. Ahn and J. W. Rabalais. Composition and structure of the Al_2O_3(0001)-(1×1) surface. *Surf. Sci.*, 388(1):121–131, (1997).

[89] I. Batyrev, A. Alavi, and M. W. Finnis. Ab initio calculations on the Al_2O_3(0001) surface. *Faraday Discuss.*, 114:33–43, (1999).

[90] A. Wander, B. Searle, and N. M. Harrison. An ab initio study of α-Al_2O_3(0001): The effects of exchange and correlation functionals. *Surf. Sci.*, 458(1):25–33, (2000).

[91] A. Marmier and S. C. Parker. Ab initio morphology and surface thermodynamics of α-Al_2O_3. *Phys. Rev. B*, 69:115401–115409, (2004).

[92] J. A. Kelber. Alumina surfaces and interfaces under non-ultrahigh vacuum conditions. *Surf. Sci. Rep.*, 62(7):271–303, (2007).

[93] D. P. Woodruff. Quantitative structural studies of corundum and rocksalt oxide surfaces. *Chem. Rev.*, 113(6):3863–3886, (2013).

[94] J. W. Elam, C. E. Nelson, M. A. Cameron, M. A. Tolbert, and S. M. George. Adsorption of H_2O on a single-crystal α-Al_2O_3(0001) surface. *J. Phys. Chem. B*, 102(36):7008–7015, (1998).

[95] C. E. Nelson, J. W. Elam, M. A. Cameron, M. A. Tolbert, and S. M. George. Desorption of H_2O from a hydroxylated single-crystal α-Al_2O_3(0001) surface. *Surf. Sci.*, 416(3):341–353, (1998).

[96] J. Toofan and P. R Watson. The termination of the α-Al_2O_3(0001) surface: a LEED crystallography determination. *Surf. Sci.*, 401(2):162–172, (1998).

[97] M. Gautier, G. Fenaud, L. Pham Van, B. Villette, M. Pollak, N. Thromat, F. Jollet, and J.-P. Duraud. α-Al_2O_3(0001) surfaces: Atomic and electronic structure. *J. Am. Ceram. Soc.*, 77(2):323–334, (1994).

[98] X.-G. Wang, A. Chaka, and M. Scheffler. Effect of the environment on α-Al_2O_3 (0001) surface structures. *Phys. Rev. Lett.*, 84(16):3650–3653, (2000).

[99] P. Thissen, G. Grundmeier, S. Wippermann, and W. G. Schmidt. Water adsorption on the α-$Al_2O_3(0001)$ surface. *Phys. Rev. B*, 80:245397–245403, (2009).

[100] S. Wippermann, W. G. Schmidt, P. Thissen, and G. Grundmeier. Dissociative and molecular adsorption of water on α-$Al_2O_3(0001)$. *Phys. Status Solidi C*, 7(2):137–140, (2010).

[101] V. Coustet and J. Jupille. High-resolution electron-energy-loss spectroscopy of hydroxyl groups at the surface of bulk insulating oxides. *Surf. Interface Anal.*, 22(1-12):280–283, (1994).

[102] V. Coustet and J. Jupille. High-resolution electron-energy-loss spectroscopy of isolated hydroxyl groups on α-al$_2$o$_3$(0001). *Surf. Sci.*, 307-309:1161–1165, (1994).

[103] V. Coustet and J. Jupille. Hydroxyl groups on oxide surfaces. *Il Nuovo Cimento D*, 19(11):1657–1664, (1997).

[104] P. Liu, T. Kendelewicz, G. E. Brown Jr., E. J. Nelson, and S. A. Chambers. Reaction of water vapor with α-$Al_2O_3(0001)$ and α-$Fe_2O_3(0001)$ surfaces: Synchrotron X-ray photoemission studies and thermodynamic calculations. *Surf. Sci.*, 417(1):53–65, (1998).

[105] P. J. Eng, T. P. Trainor, G. E. Brown Jr., G. A. Waychunas, M. Newville, S. R. Sutton, and M. L. Rivers. Structure of the hydrated α-$Al_2O_3(0001)$ surface. *Science*, 288(5468):1029–1033, (2000).

[106] J. G. Catalano. Weak interfacial water ordering on isostructural hematite and corundum (001) surfaces. *Geochim. Cosmochim. Acta*, 75(8):2062–2071, (2011).

[107] Y. Gan and George V. Franks. High resolution AFM images of the single-crystal α-$Al_2O_3(0001)$ surface in water. *J. Phys. Chem. B*, 109(25):12474–12479, (2005).

[108] D. Argyris, A. Phan, A. Striolo, and P. D. Ashby. Hydration structure at the α-$Al_2O_3(0001)$ surface: Insights from experimental atomic force spectroscopic data and atomistic molecular dynamics simulations. *J. Phys. Chem. C*, 117(20):10433–10444, (2013).

[109] B. Braunschweig, S. Eissner, and W. Daum. Molecular structure of a mineral / water interface: Effects of surface nanoroughness of α-$Al_2O_3(0001)$. *J. Phys. Chem. C*, 112(6):1751–1754, (2008).

[110] L. Zhang, C. Tian, G. A. Waychunas, and Y. R. Shen. Structures and charging of α-alumina (0001)/water interfaces studied by sum-frequency vibrational spectroscopy. *J. Am. Chem. Soc.*, 130(24):7686–7694, (2008).

[111] M. Flörsheimer, K. Kruse, R. Polly, A. Abdelmonem, B. Schimmelpfennig, R. Klenze, and T. Fanghänel. Hydration of mineral surfaces probed at the molecular level. *Langmuir*, 24(23):13434–13439, (2008).

[112] R. Polly, B. Schimmelpfennig, M. Flörsheimer, K. Kruse, A. AbdElMonem, R. Klenze, G. Rauhut, and T. Fanghänel. Theoretical investigation of the water/corundum (0001) interface. *J. Chem. Phys.*, 130(6):064702–064716, (2009).

[113] M. DelloStritto, S. M. Piontek, M. L. Klein, and E. Borguet. Relating interfacial order to sum frequency generation with ab initio simulations of the aqueous $Al_2O_3(0001)$ and $(11\bar{2}0)$ interfaces. *J. Phys. Chem. C*, 122(37):21284–21294, (2018).

[114] N. G. Petrik, P. L. Huestis, J. A. LaVerne, A. B. Aleksandrov, T. M. Orlando, and G. A. Kimmel. Molecular water adsorption and reactions on α-$Al_2O_3(0001)$ and α-alumina particles. *J. Phys. Chem. C*, 122(17):9540–9551, (2018).

[115] J. M. Wittbrodt, W. L. Hase, and H. B. Schlegel. Ab initio study of the interaction of water with cluster models of the aluminum terminated (0001) α-aluminum oxide surface. *J. Phys. Chem. B*, 102(34):6539–6548, (1998).

[116] N. H. de Leeuw and S. C. Parker. Effect of chemisorption and physisorption of water on the surface structure and stability of alpha-alumina. *J. Am. Ceram. Soc.*, 82(11):3209–2316, (1999).

[117] V. Shapovalov and T. N. Truong. Ab initio study of water adsorption on α-$Al_2O_3(0001)$ crystal surface. *J. Phys. Chem. B*, 104(42):9859–9863, (2000).

[118] Z. Łodziana, J. K. Nørskov, and P. Stoltze. The stability of the hydroxylated (0001) surface of α-Al_2O_3. *J. Chem. Phys.*, 118(24):11179–11188, (2003).

[119] V. A. Ranea, W. F. Schneider, and I. Carmichael. DFT characterization of coverage dependent molecular water adsorption modes on α-$Al_2O_3(0001)$. *Surf. Sci.*, 602(1):268–275, (2008).

[120] V. A. Ranea, I. Carmichael, and W. F. Schneider. DFT investigation of intermediate steps in the hydrolysis of α-$Al_2O_3(0001)$. *J. Phys. Chem. C*, 113(6):2149–2158, (2009).

[121] M.-P. Gaigeot, M. Sprik, and M. Sulpizi. Oxide/water interfaces: How the surface chemistry modifies interfacial water properties. *J. Phys.: Cond. Mat.*, 24(12):124106, (2012).

[122] P. Huang, T. A. Pham, G. Galli, and E. Schwegler. Alumina(0001)/water interface: Structural properties and infrared spectra from first-principles molecular dynamics simulations. *J. Phys. Chem. C*, 118(17):8944–8951, (2014).

[123] J. Janeček, R. R. Netz, M. Flörsheimer, R. Klenze, B. Schimmelpfennig, and R. Polly. Influence of hydrogen bonding on the structure of the (001) corundum–water interface. Density Functional Theory calculations and Monte Carlo simulations. *Langmuir*, 30(10):2722–2728, (2014).

[124] S.-Y. Ma, L.-M. Liu, and S.-Q. Wang. Water film adsorbed on the α-$Al_2O_3(0001)$ surface: Structural properties and dynamical behaviors from first-principles molecular dynamics simulations. *J. Phys. Chem. C*, 120(10):5398–5409, (2016).

[125] M. DelloStritto and J. Sofo. Bond polarizability model for sum frequency generation at the $Al_2O_3(0001)/H_2O$ interface. *J. Phys. Chem. A*, 121(16):3045–3055, (2017).

[126] J. Wirth, H. Kirsch, S. Wlosczyk, Y. Tong, P. Saalfrank, and R. K. Campen. Characterization of water dissociation on α-$Al_2O_3(1\bar{1}02)$: Theory and experiment. *Phys. Chem. Chem. Phys.*, 18:14822, (2016).

[127] S. Heiden, Y. Yue, H. Kirsch, J. Wirth, P. Saalfrank, and R. K. Campen. Water dissociative adsorption on α-$Al_2O_3(1\bar{1}20)$ is controlled by surface site undercoordination, density, and topology. *J. Phys. Chem. C*, 122(12):6573–6584, (2018).

[128] J. Wirth and P. Saalfrank. The chemistry of water on α-alumina: Kinetics and nuclear quantum effects from first principles. *J. Phys. Chem. C*, 116(51):26829–26840, (2012).

[129] S. Heiden, J. Wirth, R. K. Campen, and P. Saalfrank. Water molecular beam scattering at α-Al_2O_3(0001): An *ab initio* molecular dynamics study. *J. Phys. Chem. C*, 122(27):15494–15504, (2018).

[130] S. Heiden, D. Usvyat, and P. Saalfrank. Theoretical surface science beyond gradient-corrected density functional theory: Water at α-Al_2O_3(0001) as a case study. *J. Phys. Chem. C*, 123(11):6675–6684, (2019).

[131] M. K. Kesharwani, B. Brauer, and J. M. L. Martin. Frequency and zero-point vibrational energy scale factors for double-hybrid density functionals (and other selected methods): Can anharmonic force fields be avoided? *J. Phys. Chem. A*, 119(9):1701–1714, (2015).

[132] A. D. Boese and P. Saalfrank. CO molecules on a NaCl(100) surface: Structures, energetics, and vibrational Davydov splittings at various coverages. *J. Phys. Chem. C*, 120(23):12637–12653, (2016).

[133] M. Kasha, H. Rawls, and Ashraf El Bayoumi. M. The exciton model in molecular spectroscopy. *Pure Appl. Chem.*, 11:371–392, (1965).

[134] M. Heyden, J. Sun, S. Funkner, G. Mathias, H. Forbert, M. Havenith, and D. Marx. Dissecting the THz spectrum of liquid water from first principles via correlations in time and space. *Proc. Natl. Acad. Sci. U.S.A.*, 107(27):12068–12073, (2010).

[135] X. Wei and Y. R. Shen. Motional effect in surface sum-frequency vibrational spectroscopy. *Phys. Rev. Lett.*, 86:4799–4802, (2001).

[136] S. Sun, F. Tang, S. Imoto, D. R. Moberg, T. Ohto, F. Paesani, M. Bonn, E. H. G. Backus, and Y. Nagata. Orientational distribution of free O-H groups of interfacial water is exponential. *Phys. Rev. Lett.*, 121:246101–246107, (2018).

[137] T. Ohto, M. Dodia, S. Imoto, and Y. Nagata. Structure and dynamics of water at the water-air interface using first-principles molecular dynamics simulations within generalized gradient approximation. *J. Chem. Theory. Comp.*, 15(1):595–602, (2019).

[138] X. Zhuang, P. B. Miranda, D. Kim, and Y. R. Shen. Mapping molecular orientation and conformation at interfaces by surface nonlinear optics. *Phys. Rev. B*, 59:12632–12640, (1999).

[139] H. Eyring. The activated complex and the absolute rate of chemical reactions. *Chem. Rev.*, 17(1):65–77, (1935).

[140] S. Schnur and A. Groß. Properties of metal-water interfaces studied from first principles. *New J. of Phys.*, 11(12):125003–125028, (2009).

[141] D. T. Limmer, A. P. Willard, P. Madden, and D. Chandler. Hydration of metal surfaces can be dynamically heterogeneous and hydrophobic. *Proc. Natl. Acad. Sci. U.S.A.*, 110(11):4200–4205, (2013).

[142] O. Bjørneholm, M. H. Hansen, A. Hodgson, L.-M. Liu, D. T. Limmer, A. Michaelides, P. Pedevilla, J. Rossmeisl, H. Shen, G. Tocci, E. Tyrode, M.-M. Walz, J. Werner, and H. Bluhm. Water at interfaces. *Chem. Rev.*, 116(13):7698–7726, (2016).

[143] R. Mu, Z. Zhao, Z. Dohnalek, and J. Gong. Structural motifs of water on metal oxide surfaces. *Chem. Soc. Rev.*, 46(7):1785–1806, (2017).

[144] M. E. McBriarty, G. F. von Rudorff, J. E. Stubbs, P. J. Eng, J. Blumberger, and K. M. Rosso. Dynamic stabilization of metal oxide/water interfaces. *J. Am. Chem. Soc.*, 139(7):2581–2584, (2017).

[145] Z.-J. Zhao, Z. Li, Y. Cui, H. Zhu, W. F. Schneider, W. N. Delgass, F. Ribeiro, and J. Greeley. Importance of metal-oxide interfaces in heterogeneous catalysis: A combined DFT, microkinetic, and experimental study of water-gas shift on Au/MgO. *J. Catal.*, 345:157–169, (2017).

[146] Y. Tong, J. Wirth, H. Kirsch, M. Wolf, P. Saalfrank, and R. . Campen. Optically probing Al-O and O-H vibrations to characterize water adsorption and surface reconstruction on α-alumina: An experimental and theoretical study. *J. Chem. Phys.*, 114(12):054704–054716, (2015).

[147] M.-P. Gaigeot and M. Sulpizi. *Mineral/Water Interaction*, pages 271–309. John Wiley and Sons, Ltd, (2016).

[148] M. J. Gillan, D. Alfé, and A. Michaelides. Perspective: How good is DFT for water? *J. Chem. Phys.*, 144(13):130901–130934, (2016).

[149] F. Perakis, L. De Marco, A. Shalit, F. Tang, Z. R. Kann, T. D. Kühne, R. Torre, M. Bonn, and Y. Nagata. Vibrational spectroscopy and dynamics of water. *Chem. Rev.*, 116(13):7590–7607, (2016).

[150] S. Nihonyanagi, S. Yamaguchi, and T. Tahara. Ultrafast dynamics at water interfaces studied by vibrational sum frequency generation spectroscopy. *Chem. Rev.*, 117(16):10665–10693, (2017).

[151] C. Hess, S. Funk, M. Bonn, D.N. Denzler, M. Wolf, and G. Ertl. Femtosecond dynamics of chemical reactions at surfaces. *Appl. Phys. A*, 71(5):477–483, (2000).

[152] C. Hess, M. Wolf, S. Roke, and M. Bonn. Femtosecond time-resolved vibrational SFG spectroscopy of CO/Ru(001). *Surf. Sci.*, 502-503:304–312, (2002).

[153] H. Arnolds and M. Bonn. Ultrafast surface vibrational dynamics. *Surf. Sci. Rep.*, 65(2):45–66, (2010).

[154] H. Arnolds. Vibrational dynamics of adsorbates – Quo vadis? *Prog. Surf. Sci.*, 86(1):1–40, (2011).

[155] C.-S. Hsieh, R. K. Campen, M. Okuno, E. H. G. Backus, Y. Nagata, and M. Bonn. Mechanism of vibrational energy dissipation of free OH groups at the air-water interface. *Proc. Natl. Acad. Sci. U.S.A.*, 110(47):18780–18785, (2013).

[156] H.-C. Chang and G. E. Ewing. Infrared fluorescence from a monolayer of CO on NaCl(100). *Phys. Rev. Lett.*, 65:2125–2128, (1990).

[157] E. J. Heilweil, M. P. Casassa, R. R. Cavanagh, and J. C. Stephenson. Temperature dependence of the vibrational population lifetime of OH(v = 1) in fused silica. *Chem. Phys. Lett.*, 117(2):185–190, (1985).

[158] M. P. Casassa, E. J. Heilweil, J. C. Stephenson, and R. R. Cavanagh. Time-resolved measurements of OH(v=1) vibrational relaxation on SiO_2 surfaces: Isotope and temperature dependence. *J. Chem. Phys.*, 84(4):2361–2364, (1986).

[159] Y. Nagata, S. Yoshimune, C.-S. Hsieh, J. Hunger, and M. Bonn. Ultrafast vibrational dynamics of water disentangled by reverse nonequilibrium ab initio molecular dynamics simulations. *Phys. Rev. X*, 5:021002–021013, (2015).

[160] J. Jeon, J. H. Lim, S. Kim, H. Kim, and M. Cho. Simultaneous spectral and temporal analyses of kinetic energies in nonequilibrium systems: Theory and application to vibrational relaxation of O–D stretch mode of HOD in water. *J. Phys. Chem. A*, 119(21):5356–5367, (2015).

[161] J. Jeon, C.-S. Hsieh, Y. Nagata, M. Bonn, and M. Cho. Hydrogen bonding and vibrational energy relaxation of interfacial water: A full DFT molecular dynamics simulation. *J. Chem. Phys.*, 147(4):044707–044718, (2017).

[162] D. Lesnicki and M. Sulpizi. A microscopic interpretation of pump-probe vibrational spectroscopy using ab initio molecular dynamics. *J. Phys. Chem. B*, 122(25):6604–6609, (2018).

Erklärung

Hiermit versichere ich, dass die vorliegende Arbeit an keiner anderen Hochschule eingereicht sowie selbstständig und ausschließlich mit den angegebenen Quellen angefertig worden ist.

Potsdam, September 2019